



POLITECNICO DI TORINO
Repository ISTITUZIONALE

Mechanical BioMEMS Technologies for Advanced Label-free Sensing of Biomolecular Species in Microfluidic Channels

Original

Mechanical BioMEMS Technologies for Advanced Label-free Sensing of Biomolecular Species in Microfluidic Channels / Accoto, Celso. - (2016).

Availability:

This version is available at: 11583/2646290 since: 2016-08-16T15:53:49Z

Publisher:

Politecnico di Torino

Published

DOI:10.6092/polito/porto/2646290

Terms of use:

Altro tipo di accesso

This article is made available under terms and conditions as specified in the corresponding bibliographic description in the repository

Publisher copyright

(Article begins on next page)

POLITECNICO DI TORINO

SCUOLA INTERPOLITECNICA DI DOTTORATO

Doctoral Program in Electronics Devices

Final Dissertation

***Mechanical BioMEMS Technologies for Advanced
Label-free Sensing of Biomolecular Species in
Microfluidic Channels***



PhD Candidate: Celso Accoto

Tutor
Prof. Candido F. Pirri

Co-ordinator of the Research Doctorate Course
Prof. Giovanni Ghione

Co-Tutors
Dr. Francesco Rizzi
Prof. Massimo De Vittorio

April 4th 2016

To my family

CONTENTS

Abstract.....	I
Introduction.....	III
1. Chapter 1: Introduction to Biosensing for lab-on-chip devices.....	8
1.1. Introduction to BioMEMS.....	8
1.1.1. Suspended Microchannel Resonator.....	14
1.1.2. Electrophoresis devices.....	18
1.1.2.1. An introduction to parametric resonance.....	20
1.1.2.2. A MEMS-based Parametric Sensing Microfluidic Channels.....	24
References.....	26
2. Chapter 2: Laser material processing-fabrication techniques.....	31
2.1. Introduction to Laser Material Processing.....	31
2.1.1. Laser Energy-Material Interaction	32
2.2. Two Photon Lithography	33
2.2.1. Two photon lithography: photosensitive material	38
2.3. Laser machining: Laser Cutter	40
2.3.1. Laser machining materials: polydimethylsiloxane (PDMS).....	43
References.....	45
3. Chapter 3: SU-8-based Suspended Microchannel Resonator for bio-mechanical sensing applications.....	47
3.1. Device design.....	47
3.1.1. Finite element method based modelling of the suspended microchannel resonator.....	48
3.1.2. First design.....	49

3.1.3. Second design.....	52
3.2. Fabrication process	56
3.3. Characterization.....	62
References.....	68
4. Chapter 4: MEMS–based Parametric Sensing of Biomolecular Species Microfluidic Channels.....	69
4.1. Device design	69
4.1.1. First design.....	70
4.1.1.1. Modelling of the suspended microchannel resonator.....	71
4.2. Fabrication process	72
4.2.1. Process optimization.....	72
4.2.2. Device fabrication.....	74
4.3. Characterization.....	78
4.3.1. Bonding examination.....	78
4.3.2. Dynamic characterization.....	79
4.3.2.1. Scaling of beam.....	82
4.4. Second design.....	89
4.4.1. Modelling of the suspended microchannel resonator.....	90
4.4.2. Fabrication and Characterization.....	92
References.....	98
5. Chapter 5: Conclusions and Outlook.....	100
 Acknowledgements.....	 104

Abstract

The aim of this PhD project is to investigate alternative sensing methodologies that can possibly improve the sensing performances of lab-on-chip (LOC) designed for biochemical applications. Suspended microchannel resonator (SMR) for bio-mechanical sensing applications have become very popular as detection of weights of chemicals integrated in LOC. They exploit laser doppler vibrometry (LDV) for dynamic mode detection.

In this thesis two different SMRs designs have been investigated, involving either technological challenges – the use of polymers as material and processing techniques based on laser micromachining – and different sensing phenomena – the use of the parametric resonance rather than the standard harmonic resonance response.

The flexibility of two-photon direct laser writing is exploited to optimize a highly-versatile fabrication strategy based on a shell-writing procedure with the aim to reduce fabrication time of big inlet/outlet sections compatible with most microfluidic systems for LOCs. With respect to standard microfabrication techniques, requiring several technological steps to obtain suspended hollow structures, this method allows to fabricate complex SMR sensors in only one fabrication step, by virtue of its intrinsically three-dimensional nature. A SMR fixed-fixed beam has been fabricated and characterized by LDV.

A different sensing mechanism based on the parametric resonance instead of the harmonic resonance has been investigated to develop a novel platform for the characterization of biomolecules in free-flow with unique specificity, sensitivity, and speed: to this purpose a PDMS based device was realized by laser machining, a rapid prototype fabrication technique; beside to it, a commercial fused silica capillary tubing was also employed in the realization of a prototype for this sensing mechanism, and both solutions were tested through LDV.

Introduction

Microfluidics is the science that studies the manipulation of small amounts of fluids. Being the channels with dimensions of tenths to hundreds micrometres, microfluidics is the perfect tool to integrate complex systems devices, such as the so-called *lab-on-chip* (LOC), or compact microsystems for biology and chemistry applications.

Microfluidic devices can work with smaller reagent volumes, shorter reaction time, and parallel operations, which means higher effectiveness in the control of molecules and faster response time. These devices are nowadays commercially employed in chemistry, biology, pharmaceuticals and medicine, bio-defense, and other areas where they demonstrate superior performance compared to standard and bench-top methodologies.

Small size makes microfluidic systems portable, which is particularly appealing for clinical or on-field use in point-of-care diagnostics.

LOC can be also designed to perform a wide range of tasks for environmental monitoring such as detecting airborne toxins or pollutant molecules that can be present in liquids.

Depending on the nature of the transduction signal, the sensing techniques can belong to different domains:

- Optical
- Electrical
- Mechanical

Among them, resonant Micro and Nano electromechanical systems (MEMS and NEMS) have drawn attention as their mechanical properties are highly sensitive to changes in their mass by adsorption of chemicals. Basic mechanical building blocks, like bridges (fixed-fixed) and cantilevers (fixed-free), have been showed to be very effective as high sensitivity MEMS technological platform for detection of proteins, nucleic acids and chemical pollutants [1,2].

In particular, Burg et al. [3] fabricated a vacuum-packaged suspended microchannel resonant (SMR) mass sensor, showing an improved efficiency for biomolecular detection

in liquid upon accumulation of molecules on the internal walls of the microchannel. The selective mass detection is allowed by a functionalization of the internal surface of the channel by bio-receptors which, through a bio-recognition event, can bind to the target species, thus modifying the total mass of the beam and its resonant frequency thereof. Although the system in [3] achieved improved sensitivity by eliminating high damping and viscous drag in liquid environments, a further step on this way is represented by the development of fabrication techniques to allow versatile downscaling, clearly determining a technological challenge due to the highly complex fabrication process nowadays employed [4].

The aim of this PhD research, hence, is to investigate alternative sensing methodologies that can possibly improve the sensing performances of lab-on-chip, allowing the reduction of bulky experimental apparatus toward on-chip and real-time monitoring systems designed for biochemical applications.

The investigated solutions involve either technological challenges – e.g. the use of polymers as material and processing techniques based on laser micromachining – and different sensing approaches – e.g. the exploitation of the parametric resonance rather than the standard harmonic resonance response, and the results of experimental studies for both the aspects are reported.

As far as the materials are concerned, it is important to highlight the use of alternative and cheaper materials (along with simplified manufacturing procedures) rather than crystalline silicon: polymers like SU-8 photoresist (PR) or polydimethylsiloxane (PDMS), are increasingly more and more used to realize microfluidic circuits.

The processing techniques presented in this dissertation exploit laser micromachining techniques because of their relatively fast prototyping speed: Two-photon lithography (TPL) is used for the SU-8, that provides a simple and straightforward way to produce three-dimensional (3D) geometries with high-resolution, allowing the fabrication of complex 3D microstructures. On the other hand a CO₂ laser source is used to machine PDMS by laser cutting (laser ablation) technique.

This thesis work is composed of five sections that are organized in the following way.

The first chapter introduces an overview on microfluidics systems with special attention towards biosensors, and describes the two devices assessed in the dissertation: the

suspended microchannel resonator for mass detection exploiting the harmonic resonance approach and the one using parametric resonance response as sensing mechanism for label-free detection.

Technological aspects as microfabrication techniques and material characteristics are covered in Chapter 2. It starts with a small overview on the fabrication methods in microfluidics, with a focus on two-photon lithography (TPL) and CO₂ laser technology. In the second part of the chapter the material characteristics are presented and discussed. Chapter 3 and Chapter 4 are devoted to the design of the suspended microchannel resonator in SU-8, with finite element method (FEM) analysis used to evaluate the dynamic behavior of the proposed structures. Fabrication and characterization results are presented and discussed: scanning electrons microscope (SEM) and focused ion beam (FIB) have been used to verify the integrity of the samples before the testing phase, based on Laser Doppler Vibrometry technique. Finally, the conclusions and perspectives of this very promising research field are presented in Chapter 5.

This PhD program was financed by the Ministry of Education and Research for the project "PONa3_00077, Infrastructure Project for bio-MEMS Technologies for Advanced Sensing of Environmental and Food Monitoring and Diagnostics", and has involved academic and research centers such as Politecnico di Torino, the Center for Biomolecular Nanotechnologies (CBN) of the Istituto Italiano di Tecnologia (IIT) in Lecce and the Prof. Kimberly Turner's Mechanics of Microscale Systems Lab at University of California Santa Barbara.

References

- [1] J.L. Arlett, E.B. Myers, M.L. Roukes, “Comparative advantages of mechanical biosensors”, Nat. Nanotechnol., vol. 6, pp. 203–215, Apr. 2011.
- [2] R. Datar, S. Kim, S. Jeon, P. Hesketh, S. Manalis, A. Boisen, T. Thundat, “Cantilever Sensors: Nanomechanical Tools for Diagnostics”, MRS Bulletin, vol. 34, pp. 449–454, Jun. 2009.
- [3] T. P. Burg, A. R. Mirza, N. Milovic, C. H. Tsau, G. A. Popescu, J. S. Foster, S. R. Manalis, “Vacuum-Packaged Suspended Microchannel Resonant Mass Sensor for Biomolecular Detection”, J. Microelectromech. S., vol. 15, no.6, pp. 1466–1476, Dec. 2006.
- [4] K. Brueckner, F. Niebelschuetz, K. Tonisch, Ch. Foerster, V. Cimalla, R. Stephan, J. Pezoldt, T. Stauden, O. Ambacher, M. A. Hein, “Micro- and nano-electromechanical resonators based on SiC and group III-nitrides for sensor applications”, Physica Status Solidi A, vol. 208, no. 2, pp. 357–376, Feb. 2011.

Chapter 1

Introduction to Biosensing for lab-on-chip devices

This chapter introduces an overview on microfluidic systems with special attention towards biosensors, and describes the two devices assessed in the dissertation: the suspended microchannel resonator for mass detection exploiting the harmonic resonance approach and the one using parametric resonance response as sensing mechanism for label-free detection.

1.1 Introduction to BioMEMS

Biological (or biomedical) microelectromechanical systems (BioMEMS or biosensors) are poised to have a significant impact on clinical and biomedical applications.

The aim of these systems is the production of an electrical signal that is proportional to the concentration of a specific chemical or set of chemicals: this feature is achieved by exploiting the so-called “*selectivity*” of biomolecules, meaning that different types of biomolecules have the highly remarkable capability of molecular recognition and show a strong affinity to the constituent in the analyte or sample. Some pairs are particularly important like enzyme–substrate, antibody–antigen, nucleic acids–complementary sequences in the construction of the sensing layer or in establishing intelligence in the sensor.

In fig.1 is represented the general concept of a biosensor [1]: it is composed of a *bioreceptor* (performing the molecular recognition) and a *transducer* for the detection method.

In particular the bioreceptor is a biological system that is in direct contact with the

sample and forms the sensitive component of the sensor, thus it has the primary importance for the selectivity.

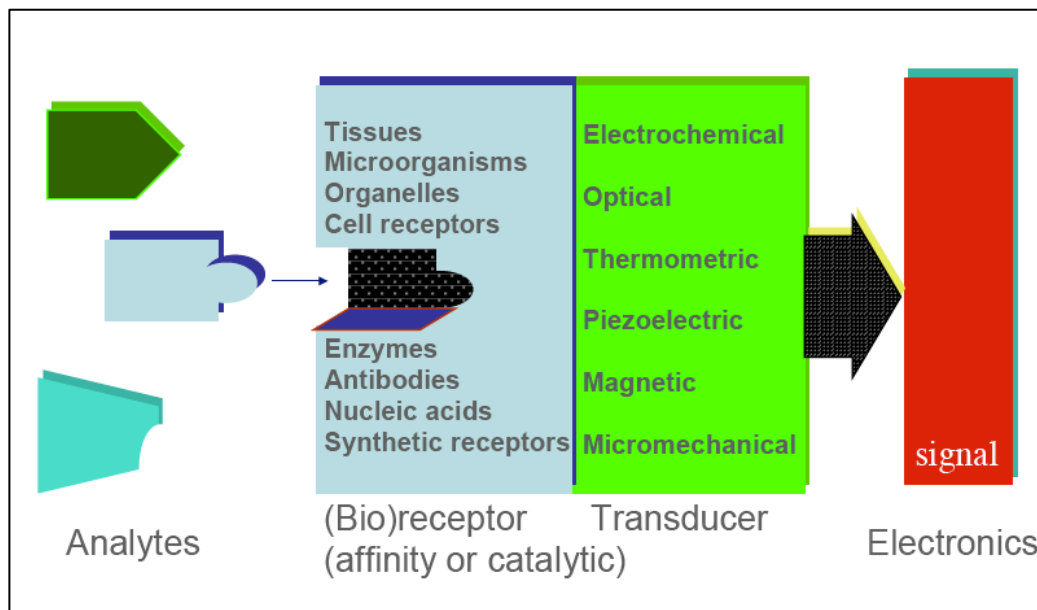


Figure 1. The function of a biosensor is to transform a biological event into an electrical signal: the molecular recognition is accomplished by the bioreceptor, while the detection method is implemented in the transducer part [1].

Various sensing modalities are used in these devices including optical, electrical or mechanical and will be discussed further below in the text.

BioMEMS – also termed “*lab-on-chip*” (LOC) – represents a significant opportunity in various settings: at home (point-of-care), at the doctor’s office, at the hospital bedside, and in clinical or commercial diagnostic laboratories. The potential impact of these technologies on the early diagnosis and management of disease can be very high for sensing and reporting on parameters ranging from physiological to biomolecular.

BioMEMS and biochips are built from silicon, plastics, or polymer by using micro and nanofabrication technologies.

These devices include microfluidic elements such as channels and wells for fluid and sample transport and could employ a range of processing, separation, and sensing modalities [2]: a schematic illustration of an integrated microsystem used for biochemical analysis and detection of DNA is shown in fig.2 [3].

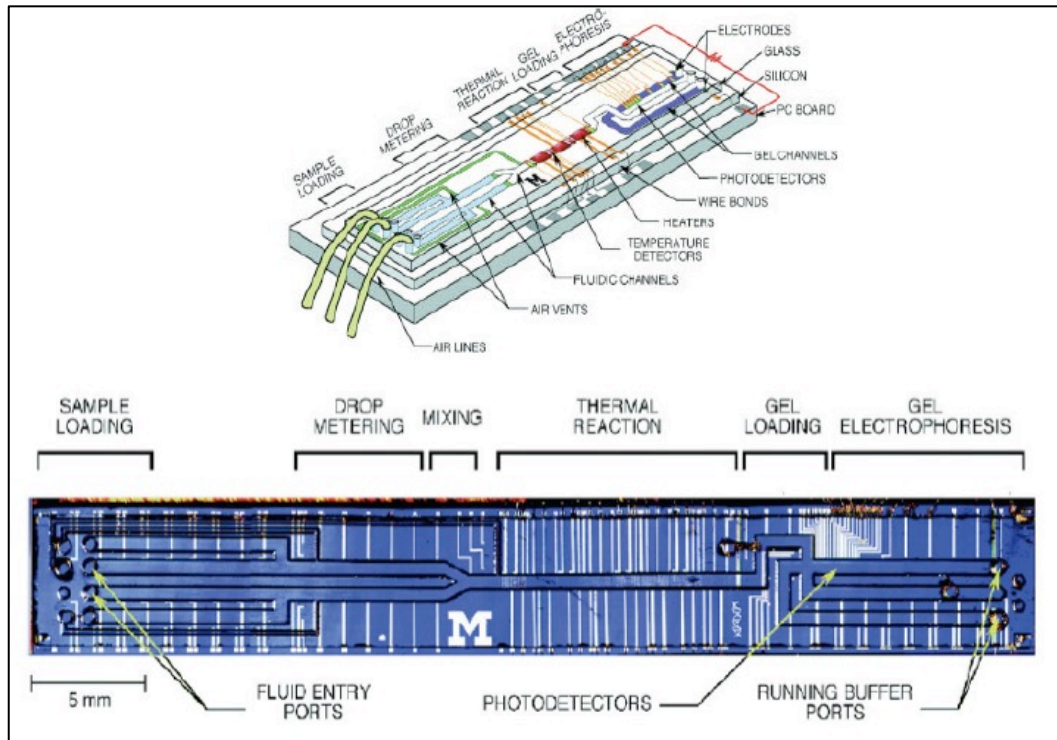


Figure 2. An Integrated Nanoliter DNA Analysis Device which has fluidic channels, heaters, temperature sensors, and fluorescence detectors to analyze nanoliter-size DNA samples [3].

These devices can also have integrated sample preparation modules and biological recognition elements such as antibodies or DNA molecules for selective capture on the same chip sensor. Clinical fluids of interest can provide a rich source of diagnostic and prognostic markers for various diseases. The possible targets from clinical fluids of interest include cells, bacteria, viruses, protein or nucleic acid-based biomarkers, or small molecules, where many or all of these targets have applications in the analysis of body fluids such as blood, urine, saliva, and cerebrospinal fluid.

In fig.3 [9] is reported a descriptive plot (from the 2011) showing the “fluidic detection limits for protein sensing” of the most sensitive technologies, both mechanical and non-mechanical: as highlighted in the picture the ideal biosensor would offer low limits of detection and quick analysis time. It was already clear in those days that microfluidic sensors are designated to approach the level of sensitivity that will permit real-time measurements.

On the other hand, for biosensor applications, it is necessary to focus on both the

intrinsic device performance and on the performance of the overall sensor system.

Fig. 3 makes it evident that micro– and nanoscale sensors can enable simultaneous, real–time, quantitative assays on large populations of individual cells, especially with the implementation of “*multiplexed microfluidics*”, where the outstanding task is the integration of complex microfluidics and dense arrays of nanoscale biosensors.

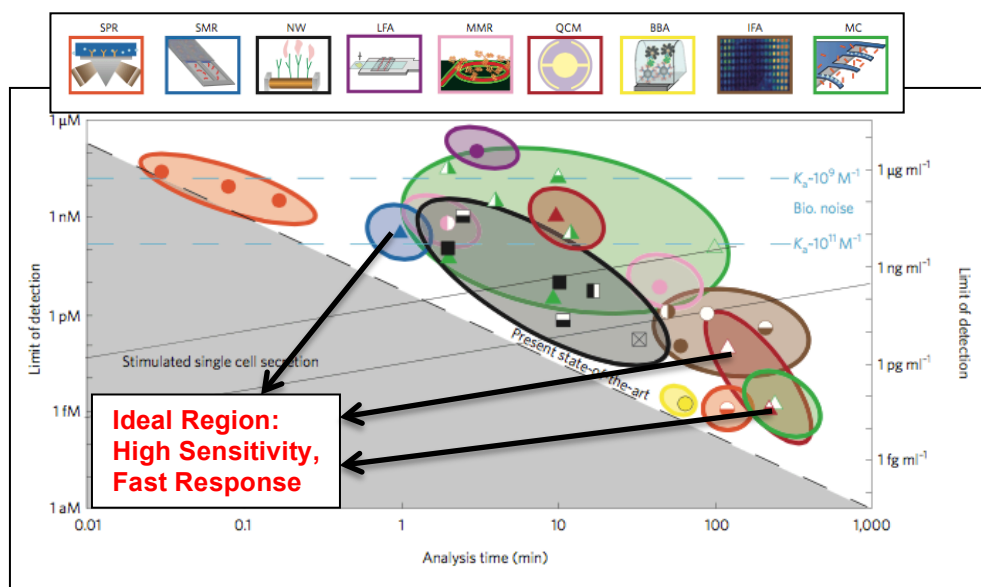


Figure 3. Limit of detection in moles (left axis) and grams per millilitre (right axis) versus the analysis time for the different types of biosensor (both mechanical and non-mechanical) shown in the panels at the top of the figure. The black dashed line shows the state-of-the-art: the challenge for new biosensors is to achieve sensitivity in the pico- to nano-molar range while also achieving shorter analysis times (figure adapted from [9]).

In general, the use of micro– and nanoscale technologies is well justified because of the following reasons: 1) reduced time–to–result due to small volumes resulting in higher effective concentrations, 2) reducing the sensor element to the scale of the target species and hence providing a higher sensitivity, 3) reduced reagent volumes and associated costs, 4) providing one–time–use disposable sensors and cartridges, and 5) the possibility of portability and miniaturization of the entire system.

Optical biosensors can be split into fluorescence–based detection and label–free detection. In fluorescence–based detection, either target molecules or biorecognition molecules are labeled with fluorescent tags, such as dyes; the intensity of the fluorescence signal indicates the amount of targeted molecules. While fluorescence

based detection is extremely sensitive, it suffers from laborious labeling processes that may also interfere with the function of the biomolecule. In contrast, in label-free detection, targeted molecules are not labeled or altered, and are detected in their natural forms. A significant part of label-free optical sensors measures the refractive index change near the sensor surface by exciting an evanescent field that exponentially decays into the bulk solution with a characteristic length between tens to hundreds of nanometers. The surface plasmon resonance method is the most popular among label free optical biosensors. Among electrical biosensors, electrochemical devices have traditionally received the major share of the attention. These devices usually couple enzymes that produce or consume electrons upon substrate recognition to an electrode transducer. Many of these enzymes specifically catalyze the reactions of clinically important analytes such as glucose, lactate, cholesterol, amino acids, urate, pyruvate, glutamate, alcohol, hydroxybutyrate, to name a few. Nanotechnology advances are providing nanoscale electrical biosensors based on semiconductor nanowires and nanotubes, in which the electrochemical gating arises from a change in the local surface potential due to the target binding.

Mechanical detection for biochemical entities and reactions has more recently been used through the exploitation of micro- and nanoscale cantilever sensors on a chip: the adsorption of molecules on a cantilever sensor has two main effects: increasing the mass and changing the surface stress. There are typically two approaches used for the measuring:

1. *Static mode* (stress sensing): sensing biomolecular interactions relies on binding induced changes in the cantilever deflection caused by differential surface stress; bending of the cantilever read-out is obtained by using optical or electrical detection;
2. *Dynamic mode* (mass sensing): alternatively called resonant-mode, relies on binding-induced changes in cantilever resonant frequency caused by mass-change or stiffness change;

In the stress sensing mode (fig.4(a)), the biochemical reaction is performed selectively on the surface of the cantilever: a generic beam which experiences a different surface

stress on two opposite sides bends itself and the deflection δ is proportional to the differential stress $\Delta\sigma$ according to the relationship [2]:

$$\delta \propto \frac{1 - \nu}{E} \left(\frac{L}{t}\right)^2 \Delta\sigma \quad (1)$$

with:

- ν is the Poisson's ratio
- E is the Young's modulus
- L is the beam length
- t is the cantilever thickness

By means of selective functionalization of one side of the cantilever it is possible to transduce molecular adsorption into mechanical bending: in general probe molecules are functionalized with thiol groups on a cantilever surface previously coated with gold. Subsequently the target molecules bind to the probe molecules, so that each step in this sequence induces a certain amount of bending, measurable by electrical or optical means (optical lever).

In case of mass sensing mode, the most established transduction mechanism is to drive the resonator at its harmonic (resonant) frequency f_r and monitor any changes in f_r ; the surface biochemical binding is sensed directly since the resonant frequency is a function of the cantilever mass: this mechanism is illustrated in fig.4(b) for a cantilever but is also valid for doubly-clamped beams which are the main devices of this research.

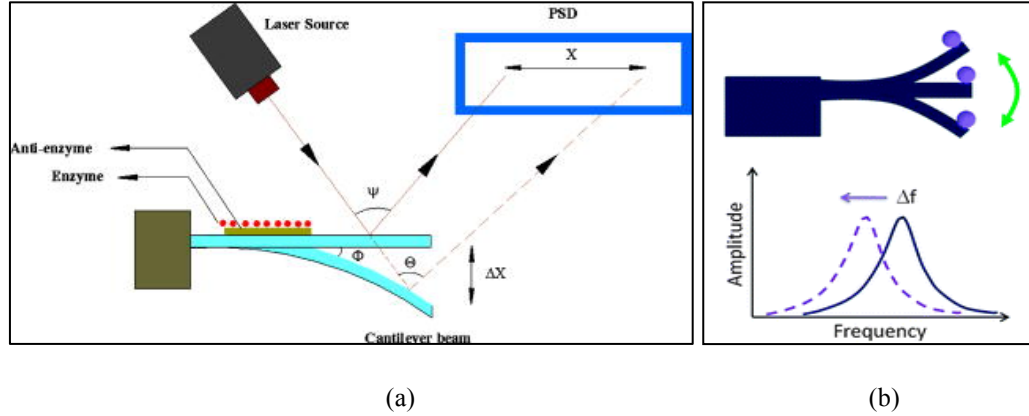


Figure 4. Illustration of the static (a) [4] and dynamic (b) [5] operation mode of nanomechanical biosensors. In (a) biomolecular interactions between target and probe molecules alter intermolecular interactions within a self-assembled monolayer on one side of the cantilever, producing a sufficient bending moment to deflect the beam. In (b) the cantilever is usually driven at its resonance frequency. Driving methods include piezoelectric actuators, magnetic forces, etc. When a biomolecule binds on the cantilever surface, the resonance frequency shifts downwards due to the added mass.

The general equation that rules the frequency–mass relationship is:

$$f_0 \propto \sqrt{\frac{k}{m_0 + \Delta m}} \quad (2)$$

where k is the stiffness of the vibrating element, m_0 is the mass of the bare beam and Δm is the loading mass.

From (2) it can be seen that the resonant frequency shifts to lower values when a quantity Δm is absorbed on the surface of the beam.

Assuming that the elastic constant does not change, if the added mass is much smaller than the mass of the resonator it is possible to obtain a linear relation between the shift in frequency and the variation of mass:

$$\Delta m \propto -\frac{\Delta f}{f_0} m_0 \quad (3)$$

1.1.1 Suspended Microchannel Resonator

Equation (3) shows that when molecules are uniformly adsorbed onto the surface of a resonating beam, the resulting relative frequency shift due to mass change is independent of the exact shape of the resonator.

Although mass detection using the resonance frequency of a beam is well suited for measuring mass in vacuum and air, its mass resolution is very poor when operated under liquid solution: in this case in fact the frequency–response of the resonator is dramatically affected by the viscosity of the fluid.

Resonance frequency variations, therefore, have represented a major challenge in the detection of adsorbed mass in liquid environments.

However, Burg et al. demonstrated a hollow cantilever concept called the suspended microchannel resonator (SMR) – schematically reported in fig.5 – that is capable of detecting biological interactions in liquids, showing high performances in terms of sensitivity thanks to the fact that a high–Q operation is restored [6]. In fact, the liquid analyte is allowed to flow inside the suspended microchannel, changing the mass of the resonating beam after adsorption with the inner surfaces inside. The whole system is then able to vibrate in a vacuum environment without viscous damping.

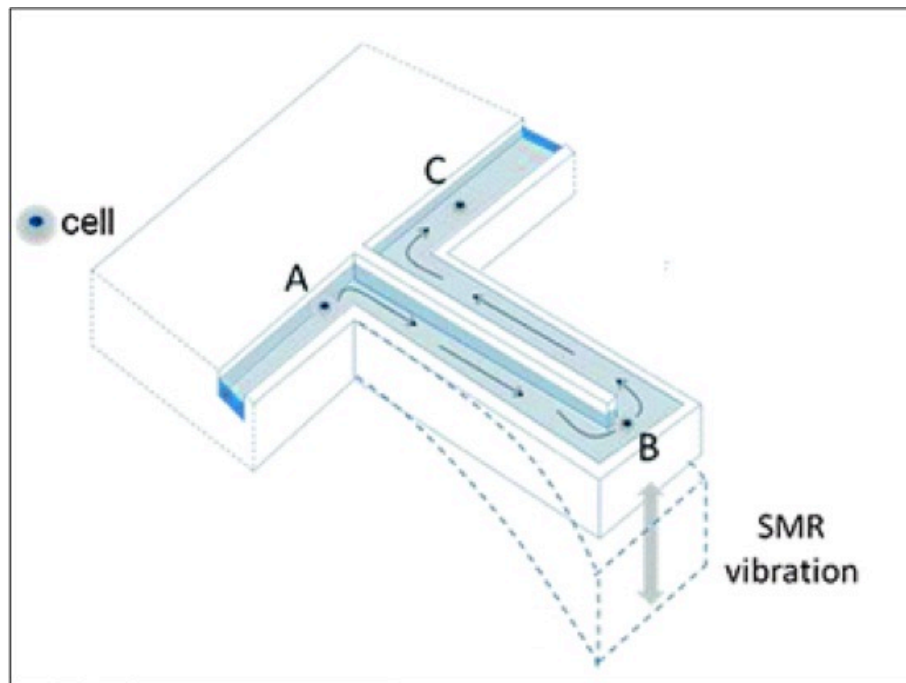


Figure 5. A cantilever as Suspended Microchannel Resonator for the measurement of the mass and density of cells in a liquid solution [5].

In particular, for a fixed–fixed beam having an internal channel with constant cross section, the mass sensitivity is – neglecting second order effects – a function of the ratio

between the adsorbed mass and the total mass and does not depend on the exact geometry.

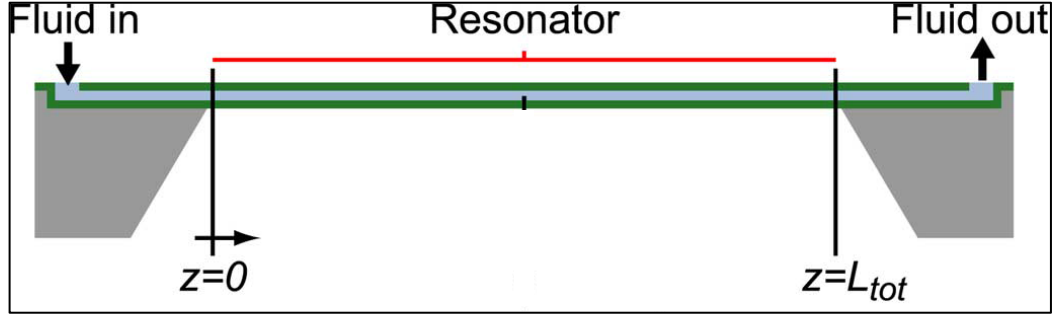


Figure 6. Parameters describing the geometry of an arbitrarily shaped suspended microchannel. The z axis measures the distance from the inlet along the channel. The channel is assumed to have a constant rectangular cross section [6].

Assuming pure bending, the displacement field of a vibrational mode is represented by a one-dimensional (1-D) function $u(z)$ (see fig. 6). Equating the maximum kinetic and the maximum potential energy (W) yields the resonance frequency as follow:

$$f_0^2 = \frac{W}{4\pi^2 \int_0^L \frac{1}{2} m_A(z) \cdot u(z)^2 dz} \quad (4)$$

with $m_A(z) = \int \rho(x, y, z) dx dy$ being the mass per unit length.

m_A increases when molecules are adsorbed: we call this increase in the mass as Δm_A and the related frequency change Δf and equation (4) becomes:

$$(f_0 + \Delta f)^2 = \frac{W}{4\pi \int_0^L \frac{1}{2} [m_A(z) + \Delta m_A(z)] \cdot u(z)^2 dz} \quad (5)$$

At first order, $\frac{\Delta f}{f_0}$ as a function of Δm_A is given by:

$$\frac{\Delta f}{f_0} = -\frac{1}{2} \frac{\int_0^L \Delta m_A(z) \cdot u(z)^2 dz}{\int_0^L m_A(z) \cdot u(z)^2 dz} \quad (6)$$

which becomes equation (7) if $\Delta m_A(z)/m_A(z)$ is constant:

$$\frac{\Delta f}{f_0} \approx -\frac{1}{2} \frac{\Delta m_A}{m_A} \quad (7)$$

In recent years, exciting and significant advances in biochemical detection have been made using cantilever and fixed–fixed beam with internal channels as sensing elements, and direct, label–free quantitative measurements of biomolecular detection of a whole host of entities and mechanisms has been reported from DNA, protein, viruses, cells, and cell growth [7, 8, 9, 10].

In [7] Burg et al. demonstrate that SMRs can also serve to track passing particles of diverse sizes, such as bacteria or cells (fig. 7). When the particle travels in the microchannel, the resonant frequency drops by an amount that depends on the position of the particle along the resonating structure and on the particle density and volume. Bacteria such as *Escherichia coli* and *Bacillus subtilis*, which have different masses, were distinguished with the use of SMRs.

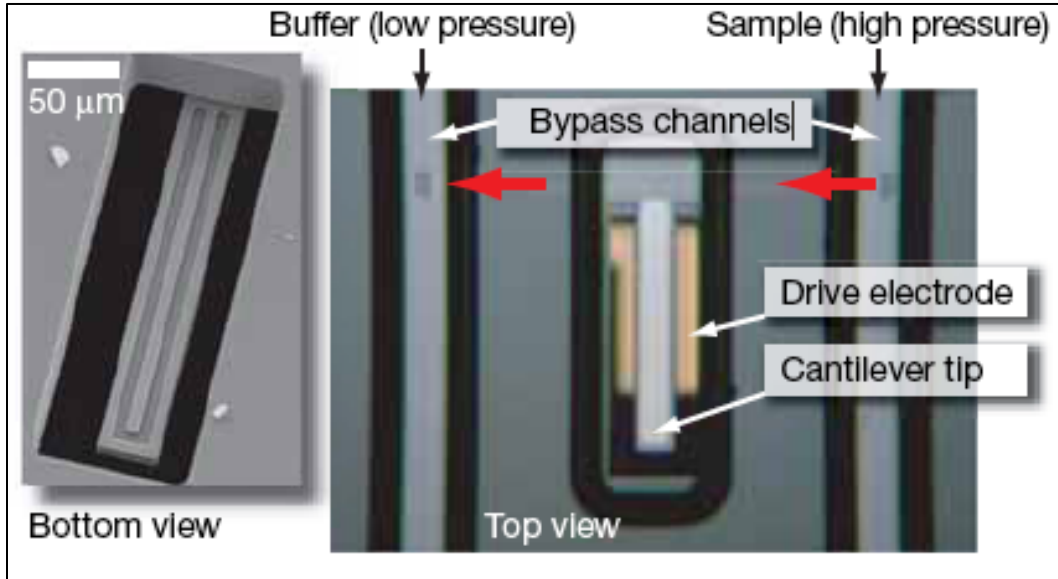


Figure 7. Microcantilever containing a microfluidic channel developed for measuring the weight of single cells and single nanoparticles [7].

Furthermore, cantilever sensors have been used to measure the mass of cells and biomolecules in [11], concentrations of dilute cell suspensions in [12, 13], also nucleic acids in [14, 15], as well as bacterial and fungal growth in [16, 17].

Pursuing this research field, we propose the suspended microchannel resonator device made of the photosensitive polymeric material SU-8, exploiting the “two-photon” direct laser writing technique, with an optimized procedure for the fabrication of big inlet/outlet sections compatible with most microfluidic systems for Lab-On-Chip. With respect to standard microfabrication techniques, requiring several technological steps to obtain suspended hollow structures, this method allows to fabricate complex SMR sensors in only one fabrication step, by virtue of its intrinsically three-dimensional nature.

1.1.2 Electrophoresis devices

Most of LOC devices have an analytical section in which the single species present in the analyte solution are isolated and its contents separated and detected. Several microfluidic devices have been developed for single-cell analysis because miniaturized systems facilitate low-volume sample handling and increase throughput by automation [18, 19].

Sample transport on biochip devices generally is a combination of electroosmosis, electrophoresis, and pressure-driven flow. Analyte movement into the electrophoresis channel occurs via application of an electric field, and all applied forces are along the axis of the electrophoresis channel.

Figure fig. 8 shows a typical junction structure of the kind used to perform electrophoretic chemical separations [20].

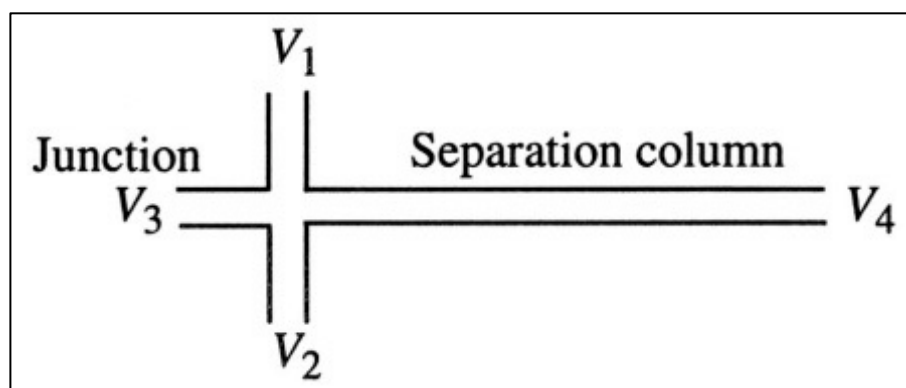


Figure 8. A junction and separation column used for electrophoretic separation in combination with electroosmotic flow [20].

Four flow channels meet at an intersection. The system is filled with an electrolyte buffer solution, and voltages are applied via electrodes immersed in the reservoirs at the ends of each channel (not shown in the picture). On the right is a long separation column. A positive voltage is applied to V_1 while V_2 is grounded so that electroosmotic flow carries the sample electrolyte through the junction region; voltages must also be applied at V_3 and V_4 to prevent the sample from entering the horizontal channels.

Once the sample-filling voltages have been applied long enough for the slowest moving fluid component to reach the intersection, the voltages are switched: a large voltage is applied at V_3 and V_4 is grounded. This creates a rapid electroosmotic flow down the separation channel, fed with buffer from the V_3 reservoir. If the ionic sample species are positively charged, they move faster than the fluid buffer; if negatively charged, they move slower and, depending on their respective mobility, the different chemical species get separated by the electric field while the flow is taking place. By the time the sample fluid reaches the end of the separation channel, distinct bands of different species are observed, either by fluorescence or some other optical technique.

Although a variety of detection schemes have been developed for microfluidic analytical devices [21, 22, 23, 24, 25, 26], fluorescence detection remains the preferred method for the investigation of biomolecule properties [27, 28, 29, 30]. Its widespread use allows researchers to leverage the long experience matured within the scientific community, and the collective efforts to enhance sensitivity (i.e. two-photon excitation, TIRF, [31]) and mitigate some of its inherent problems (i.e. fluorescent background

signal, photobleaching). However, in spite of these efforts, fluorescence detection still suffers from fundamental disadvantages. For instance, tagging samples with fluorescent labels is a time consuming and labor intensive procedure. In addition, the attachment of fluorophores to biomolecules can alter their surface or charge characteristics and, therefore, some aspects of their natural behavior. Another major disadvantage is that fluorescence detection needs bulky instrumentation, difficult to integrate on-chip and therefore not suitable for portable diagnostic devices. Moreover, as the size of the fluidic channels decreases, the detection of fluorescence signals requires to engineer more sensitive and therefore more sophisticated and expensive solutions. In recent years, a number of alternative solutions to optical sensing have been proposed, from nanowire-based field effect transistors (FET) [23], to nanopores coupled with electrical sensing [24, 32], to functionalized electronic “barcodes” coupled to RF frequency readout [26]. Although offering promising results, these methods require cumbersome fabrication procedures.

A possible alternative to an optical detection system would exploit parametric resonance phenomena applied to a suspended separation column resonator, as described in the next section.

1.1.2.1 An introduction to parametric resonance

In many engineering and physical systems, oscillatory behavior of the dynamic system due to periodic excitation is of great interest.

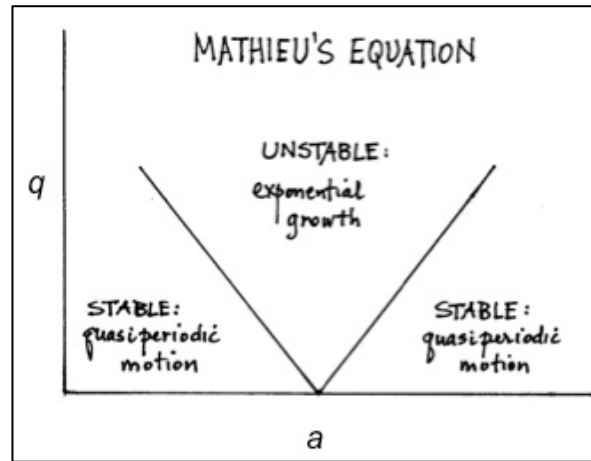
Two kinds of oscillatory responses can be distinguished: forced oscillations and parametric oscillations. Forced oscillations appear when the dynamical system is excited by a periodic input. If the frequency of an external excitation is close to the harmonic frequency of the system, then the system will experience *harmonic resonance*, i.e. oscillations with a large amplitude. Parametric oscillations are the result of having time-varying (periodic) parameters in the system. In this case, the system could experience *parametric resonance*, and again the amplitude of the oscillations in the output of the system will be large.

Systems with time-varying parameters are called parametrically excited systems [33].

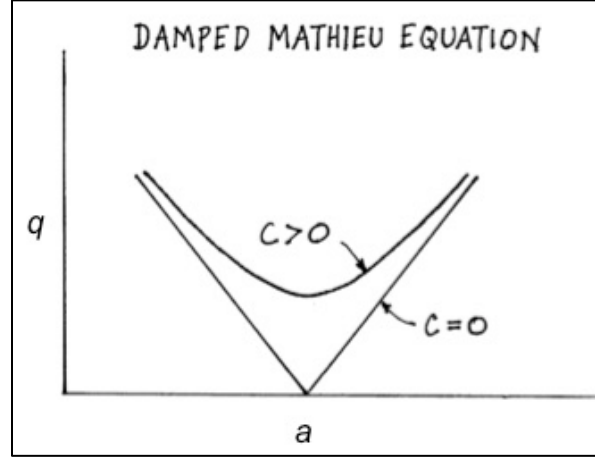
The dynamical behavior of a system in parametric resonance is described by the well-known *Mathieu's equation*, which is a special case of second order differential equation with a periodic coefficient:

$$\frac{d^2u}{dt^2} + c \frac{du}{dt} + [a - 2q\cos(2t)]u = 0 \quad (8)$$

Equation (8) has solutions that can be periodic and bounded (referred to as *stable solution*), or *unstable* solution: depending on a and q (the parameters of the system), the solution of Mathieu's equation is stable for certain values of a and q , whereas it is unstable for other values; this allows to define *stability regions* in the plane (a,q) as illustrated in fig.11 [34].



(a)



(b)

Figure 11. Schematic of the parameter space showing the “V”-shaped boundary between stable and unstable region. In (a) the ideal situation of zero damping ($c = 0$) is represented, while in (b) a realistic condition where damping is present is shown: in this case the bottom tip of the wedge moves upwards but the shape remains essentially unchanged [34].

It can be proven that instabilities occur at $a = n^2$, with n integer, and that the boundaries of the first instability region ($n=1$), for small values of q , are given by $a = 1 \pm 2q$. In terms of the physical parameters of the device, the driving frequencies that cause unstable responses in the system are given by:

$$\omega_1 = \frac{2\omega_r}{n} \quad (9)$$

where ω_r is the *harmonic resonant* frequency of the system. Furthermore, in a realistic case the presence of a damping term (c in the equation (8)) has to be considered, resulting in the shifting of the tongues upwards (fig.11(b)) in the a - q parameter space requiring a minimum driving threshold for the onset of the parametric resonance: this is the reason why parametric resonance is difficult to observe at the macroscale.

Figure 12 illustrates an important characteristic of this mode of operation: namely, the sharp transition of the oscillation (vertical segment) that marks the entrance into the parametric region.

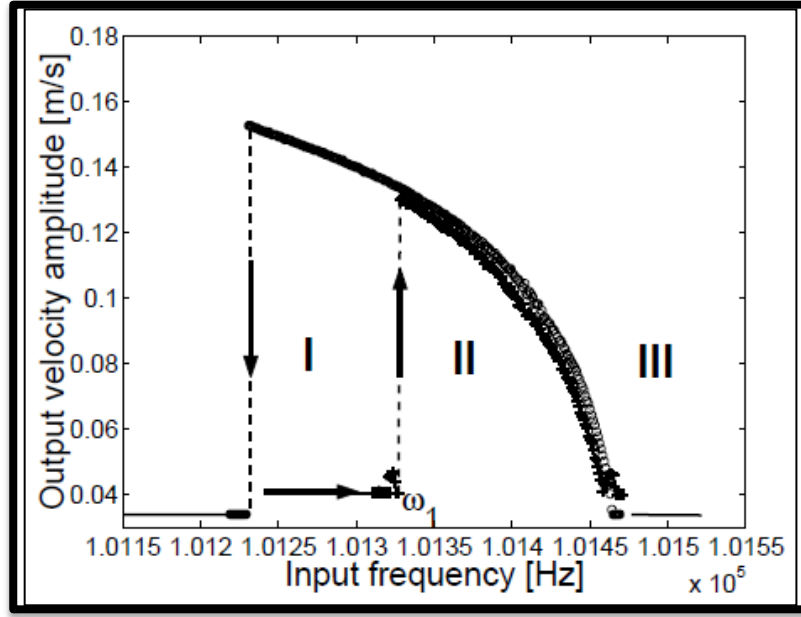


Figure 9. The 'jump' event is characteristic of parametric resonators: it always occurs when the excitation frequency is twice the resonant frequency of the system. Experimental data of a parametrically excited micro resonator revealing a sharp transition between parametric region (II) and zero amplitude response (I). Sensing can be performed by tracking this spectral feature [35].

The plot in fig. 12 represents experimental data of an electrostatically actuated micro-cantilever from [35]: the device is made of highly doped polysilicon with measures $200\mu\text{m} \times 50\mu\text{m} \times 2\mu\text{m}$, and tested in vacuum ($p = 8\text{mT}$), sweeping the frequency of the driving signal from low to high and from high to low. The curves illustrate an important characteristic of this mode of operation: the sharp transition (vertical segment) of the oscillation that marks the entrance into the parametric region (upper branch in the fig. 12). This transition always occurs for the value ω_1 (twice the resonance frequency, in the case depicted in fig. 12, according to equation (9)). A further increase of the input frequency to region II decreases the output velocity amplitude. Finally, going from region II to region III, the system reaches negligible output velocity amplitude. Driving the system in the opposite direction increases the output velocity signal until collapsing again to negligible amplitude. Thus, driving the beam with a sinusoidal signal of frequency ω_1 keeps the system at the upper branch at the boundary between the unstable and stable regions (fig. 12): any changes in the system's harmonic resonance frequency (for example due to a change in the oscillating mass) will cause the parametric

resonance condition not to be satisfied. A decrease in the harmonic frequency ω_r leads to a collapse of the oscillation back to the negligible amplitude solution (region I in the figure) [35, 36]. For example, in case of an added mass, the harmonic frequency decreases thus forcing the system back into region I.

1.1.2.2 A MEMS-based Parametric Sensing in Microfluidic Channels

We propose [37] to develop a novel, resonant-based detector that senses biomolecular markers by monitoring the parametric oscillations of a fixed-fixed beam embedded at the end of the microfluidic separation channel, as illustrated in fig.13.

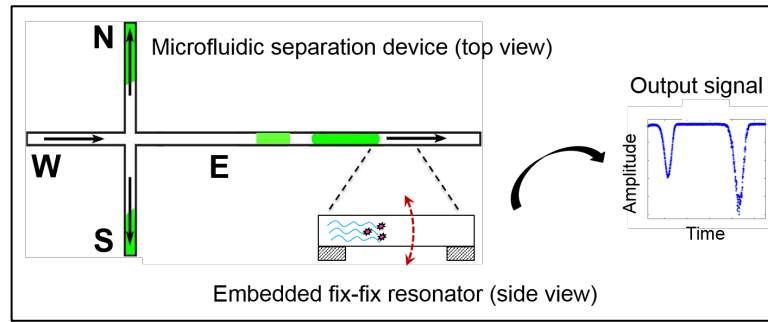


Figure 13. Schematic description of the proposed approach: microfluidic separation and parametric detection device. Complex samples are first separated into their elementary components by microcapillary electrophoresis. By monitoring the parametric oscillation of the embedded fixed-fixed resonator, the detection of different species can be made without any sample labeling [37].

If successful this solution will couple the advantages of microfluidic bioanalytical platforms with label-free detection of biomolecules. Although sensing in microfluidic channels using shifts in harmonic resonance frequency has been demonstrated (with the microfluidic channel typically embedded in the resonant structure), this would be the first device exploiting *parametric* resonance: an instability phenomenon, characterized by a sharp transition between oscillatory and non-oscillatory behavior. The transition is governed by a resonance condition dependent on system's parameters: thus, changes in these parameters translate into changes in oscillator behavior. Advantages include sensitivity: due to the sharp transition, even very small frequency shifts (few mHz) can be accurately detected [38, 39, 40, 41]; possibility of compact implementations of the platform within portable devices with all electronic detection; analysis of biomolecules

closer to native conditions, because of the absence of labels; simpler sample preparation procedure (no need for fluorescence); cost is concentrated in the reusable platform (no additional costs for sample labeling).

References

- [1] A. Turner lecture at DTU, 2012.
- [2] R. Bashir, “BioMEMS: State of the art in detection and future prospects,” *Adv. Drug Deliv. Rev.*, vol. 56, no. 11, pp. 1565–1586, 2004.
- [3] Burns, M. A.; Johnson, B. N.; Brahmasandra, S. N.; Handique, K.; Webster, J. R.; Krishnan, M.; Sammarco, T. S.; Man, P. M.; Jones, D.; Heldsinger, D.; Mastrangelo, C. H.; Burke, D. T., “An Integrated Nanoliter DNA Analysis Device”. *Science* 1998, 282, 484–487.
- [4] Amritsar Jeetender; Ion G. Stiharu; Packirisamy Muthukumaran, “Bioenzymatic detection of troponin C using micro-opto-electro-mechanical systems”, *J. Biomed. Opt.* 11(2), 021010 (April 03, 2006)
- [5] Javier Tamayo, Priscila M. Kosaka, José J. Ruz, Álvaro San Paulo and Montserrat Calleja, “Biosensors based on nanomechanical systems”, *Chem. Soc. Rev.*, 2013, 42, 1287-1311
- [6] T. P. Burg, A. R. Mirza, N. Milovic, C. H. Tsau, G. A. Popescu, J. S. Foster, S. R. Manalis, “Vacuum-Packaged Suspended Microchannel Resonant Mass Sensor for Biomolecular Detection”, *J. Microelectromech. S.*, vol. 15, no.6, pp. 1466–1476, Dec. 2006.
- [7] T. P. Burg, M. Godin, S. M. Knudsen, W. Shen, G. Carlson, J. S. Foster, K. Babcock, and S. R. Manalis, “Weighing of biomolecules, single cells and single nanoparticles in fluid,” *Nature*, vol. 446, pp. 1066–1069, 2007.
- [8] P. S. Waggoner, C. P. Tan, and H. G. Craighead, “Microfluidic integration of nanomechanical resonators for protein analysis in serum,” *Sens. Actuators B, Chem.*, vol. 150, no. 2, pp. 550–555, 2010.
- [9] J. L. Arlett, E. B. Myers, and M. L. Roukes, “Comparative advantages of mechanical biosensors,” *Nat. Nanotechnol.*, vol. 6, pp. 203–215, 2011.

- [10] R. Datar, S. Kim, S. Jeon, P. Hesketh, S. Manalis, A. Boisen, T. Thundat, “Cantilever Sensors: Nanomechanical Tools for Diagnostics”, *MRS Bulletin* 34 (2009) 449-454.
- [11] Ilic, B., Czaplewski, D., Zalalutdinov, M., Craighead, H.G., Neuzil, P., Campagnolo, C., Batt, C., “Single cell detection with micromechanical oscillators”, 2001. *J. Vac. Sci. Technol. B* 19 (6), 2825–2828
- [12] Campbell, G.A., Mutharasan, R., 2007b. *Environ. Sci. Technol.* 41 (5), 1668–1674.
- [13] Li, S.Q., Fu, L.L., Barbaree, J.M., Cheng, Z.Y., “Resonance behavior of magnetostrictive micro/milli-cantilever and its application as a biosensor”, 2009. *Sens. Actuators, B* 137 (2), 692–699.
- [14] Su, M., Li, S.U., Dravid, V.P., “Microcantilever resonance-based DNA detection with nanoparticle probes”, 2003. *Appl. Phys. Lett.* 82 (20), 3562–3564.
- [15] Ilic, B., Yang, Y., Aubin, K., Reichenbach, R., Krylov, S., Craighead, H.G., “Enumeration of DNA Molecules Bound to a Nanomechanical Oscillator”, 2005. *Nano Lett.* 5 (5), 925–929
- [16] Gfeller, K.Y., Nugaeva, N., Hegner, M., “Rapid biosensor for detection of antibiotic-selective growth of *Escherichia coli*.”, 2005b. *Appl. Environ. Microbiol.* 71 (5), 2626–2631
- [17] Nugaeva, N., Gfeller, K.Y., Backmann, N., Lang, H.P., Duggelin, M., Hegner, M., “Micromechanical cantilever array sensors for selective fungal immobilization and fast growth detection”, 2005. *Biosens. Bioelectron.* 21 (6), 849–856
- [18] Sims CE, Allbritton NL. *Lab Chip.* 2007; 7:423–440. [PubMed: 17389958].
- [19] Zare RN, Kim S. *Annu. Rev. Biomed. Eng.* 2010; 12:187–201. [PubMed: 20433347].
- [20] Stephen D. Senturia, “MICROSYSTEM DESIGN”, 2001 KLUWER ACADEMIC PUBLISHERS
- [21] J. D. Adams and H. T. Soh, “Tunable acoustophoretic band-pass particle sorter,” *Appl*

Phys Lett, vol. 97, no. 6, p. 064103, 2010.

[22] C. Minseon, X. Yi, J. Nie, R. Stewart, T. A. Csordas, O. Seung Soo, J. A. Thomson, and H. T. Soh, “Quantitative selection of DNA aptamers through microfluidic selection and high-throughput sequencing,” *Proc Natl Acad Sci USA*, vol. 107, pp. 15373–8, 2010.

[23] Y. Chen, X. Wang, M. K. Hong, S. Erramilli, P. Mohanty, and C. Rosenberg, “Nanoscale field effect transistor for biomolecular signal amplification,” *Appl. Phys. Lett.*, vol. 91, no. 24, p. 243511, 2007.

[24] D. Stoddart, A. J. Heron, E. Mikhailova, G. Maglia, and H. Bayley, “Single nucleotide discrimination in immobilized DNA oligonucleotides with a biological nanopore,” *Proc. Natl. Acad. Sci. U. S. A.*, vol. 106, no. 19, pp. 7702–7, May 2009.

[25] G. V. Soni and A. Meller, “Progress toward ultrafast DNA Sequencing using solid-state nanopores,” *Clin. Chem.*, vol. 53, no. 1996–2001, 2007.

[26] D. K. Wood, G. B. Braun, J.-L. Fraikin, L. J. Swenson, N. O. Reich, and A. N. Cleland, “A feasible approach to all-electronic digital labeling and readout for cell identification,” *Lab Chip*, vol. 7, pp. 469–474, 2007.

[27] J. Han and H. G. Craighead, “Entropic trapping and sieving of long DNA molecules in a nanofluidic channel,” *J. Vac. Sci. Technol. A Vacuum, Surfaces, Film.*, vol. 17, no. 4, p. 2142, 1999.

[28] C. Reccius, J. Mannion, J. Cross, and H. Craighead, “Compression and Free Expansion of Single DNA Molecules in Nanochannels,” *Phys. Rev. Lett.*, vol. 95, no. 26, pp. 1–4, 2005.

[29] J. O. Tegenfeldt, C. Prinz, H. Cao, S. Chou, W. W. Reisner, R. Riehn, Y. M. Wang, E. C. Cox, J. C. Sturm, P. Silberzan, and R. H. Austin, “The dynamics of genomic-length DNA molecules in 100-nm channels,” *Proc Natl Acad Sci USA*, vol. 101, no. 30, pp. 10979–10983, 2004.

- [30] Y.-C. Wang and J. Han, "Pre-binding dynamic range and sensitivity enhancement for immuno-sensors using nanofluidic preconcentrator.," *Lab Chip*, vol. 8, no. 3, pp. 392–4, 2008.
- [31] T. Wynne and S. Pennathur, "Three-Dimensional Time Resolved Measurements of Charged Quantum Dots in Nanoconfined Channels using Total Internal Reflection Fluorescence Microscopy (TIRFM)," in *Proc. Of the 15th Hilton Head Conf.*, Hilton Head Island, SC, USA, 2010.
- [32] A. Meller, L. Nivon, E. Brandin, J. Golovchenko, and D. Branton, "Rapid nanopore discrimination between single polynucleotide molecules," *Proc. Natl Acad. Sci. USA*, vol. 97, no. 3, pp. 1079–1084, 2000.
- [33] Nayfeh, A. H., Mook, D. T.: *Nonlinear Oscillations*. John Wiley & Sons. New York, (1979).
- [34] Richard H. Rand, *Lecture Notes on Nonlinear Vibrations*, version 53, Cornell University.
- [35] M. Napoli, R. Baskaran, K. Turner and B. Bamieh, "UNDERSTANDING MECHANICAL DOMAIN PARAMETRIC RESONANCE IN MICROCANTILEVERS" *IEEE* 2003.
- [36] M. T. Napoli, W. Zhang, K. Turner, and B. Bamieh, "Characterization of Electrostatically Coupled Micro Cantilevers," *J. Microelectromechanical Syst.*, vol. 14, no. 2, pp. 295–304, 2005
- [37] M. T. Napoli, "Label-free Sensing of Biomolecular Species in Microfluidic Channels", proposal
- [38] W. Zhang and K.L. Turner, "Frequency tuning and control of parametrically resonant mass-sensors", *Journal of Vacuum Technology A*, vol. 23, pp. 841–845, 2005.
- [39] C. B. Burgner, N. J. Miller, K. L. Turner and S. W. Shaw, "Noise squeezing control for bifurcation sensing in MEMS", *Proc. ASME IDETCCIEC*, Washington, DC '11, pp. 456–789, August 2011.

[40] W. H. Zhang and K. Turner, "Application of parametric resonance amplification in a single-crystal silicon micro-oscillator based mass sensor," *Sensors Actuators A Phys.*, vol. 2005, no. 122, pp. 23–30.

[41] W. Zhang and K. Turner, "A Mass Sensor Based On Parametric Resonance," in *Solid-State Sensor, Actuator and Microsystems Workshop*, Hilton Head Island, South Carolina, 2004.

Chapter 2

Laser material processing– fabrication techniques

This chapter contains the description of the fabrication processes implemented for the realization of the suspended microresonators: first, we describe the Two photon lithography technique used to fabricate the SU8–based device, then the CO₂ laser technology to process the PDMS will be presented.

In each section the corresponding material characteristics are highlighted and discussed.

2.1 Introduction to Laser Material Processing

Laser material processing utilizes laser energy to modify the shape or appearance of a material. This method of material modification provides numerous advantages to customers such as the ability to quickly change designs, produce products without the need for tooling, and improve quality of finished parts.

Another advantage of laser material processing is compatibility with a multitude of materials. Compatible materials range from non–metals such as ceramics, composites, plastics/polymers and adhesives to metals including aluminum, iron, stainless steel and titanium. This section contains a general description on the effects produced by laser energy interacting with a material and the laser processes that are applied to the majority of materials.

2.1.1 Laser Energy–Material Interaction

The effects produced by laser energy interacting with a material strongly depend upon the wavelength and power level of the laser, and the absorption characteristics and chemical composition of the material.

Common wavelengths for laser material processing are 10,6 μm and 9,3 μm produced by CO₂ lasers, 1,06 μm produced by Nd:YAG solid state laser, a wide NIR/IR range by diode and fiber lasers [1, 2]. A range of power levels are available for each laser type to optimize the laser energy–material interaction. However, the absorption characteristics and chemical composition of the material to be processed and the desired results will greatly influence the selection of the laser type and power level.

The effects of the laser energy–material interaction are *material ablation* and/or *material modification*:

- Material ablation is a physical process that removes material. Material is removed completely from the top to the bottom surface or partially from the top of the material down to a specified depth;
- Material modification is a physical process that alters the properties and/or appearance of a material; direct laser writing process belong to this class of interaction.

Material ablation is used for cutting, engraving and marking with depth. Material modification is used for marking on the surface of a material by changing the appearance or properties of the material. The terms cutting, engraving and marking are commonly referred to as laser processes.

The effects of the laser energy–material interaction are schematically illustrated in fig.1.

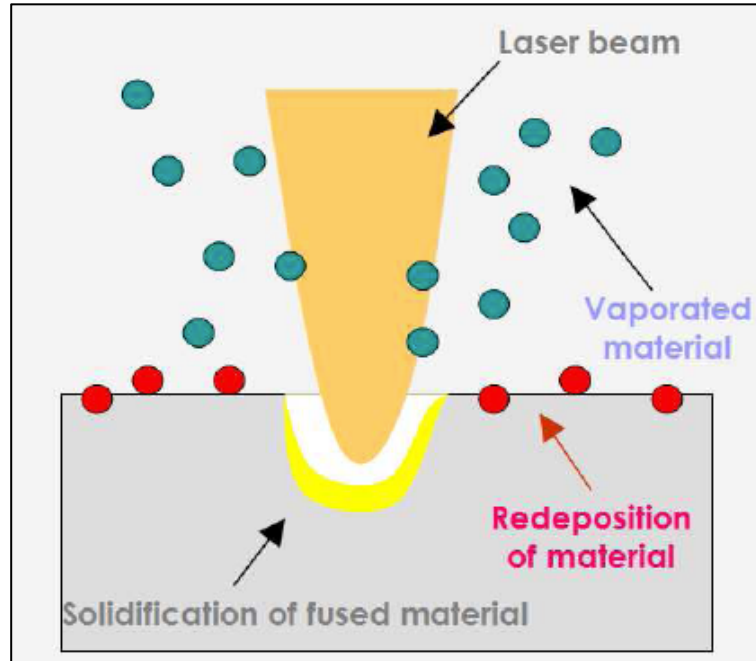


Figure 1. Process of modification of sample surface through phase changes induced by the laser energy absorbed by the material: 1) the laser beam impinges a material can be reflected, absorbed or transmitted; 2) the absorbed energy is transformed in thermal energy inside the material; 3) this absorption can determines some effects on the substrates which depend on process parameters [1].

If the material interacting with laser light is a photocurable polymer, i.e. able to change its physical or chemical state after interaction with radiation, it is possible to define a *Photopolymerization* interaction. This kind of laser–material interaction is at the base of Two–photon Lithography for Direct Laser Writing processing of Polymers.

2.2 Two Photon Lithography

Two–photon lithography (TPL) – also known as two–photon polymerization (TPP) – is a recent “*direct laser writing*” (DLW) technique allowing to create complex 3D structures with sub-micron resolution from photosensitive materials (i.e. photoresist).

Polymerization is defined as a process of linking monomer molecules together in a chemical reaction to form three–dimensional networks or polymer chains. It can be initiated via energy introduced from light or heat. The photo–polymerization is defined as

the light-induced chemical reaction of monomers or oligomers that results in a solid polymeric network. Material systems for photo-polymerization contain two main components: a *photoinitiator* and a *monomer* (or a mixture of monomers and oligomers). Photoinitiators are molecules having low photo dissociation energy and are added to increase the material photosensitivity. Photo-polymerization reactions that form a cross-linked network follow the characteristic steps of any chain polymerization mechanism: photoinitiation, propagation and termination. Then the sample is immersed in the developer bath to selectively remove the non-polymerized material: the complete procedure is illustrated in fig. 2 below.

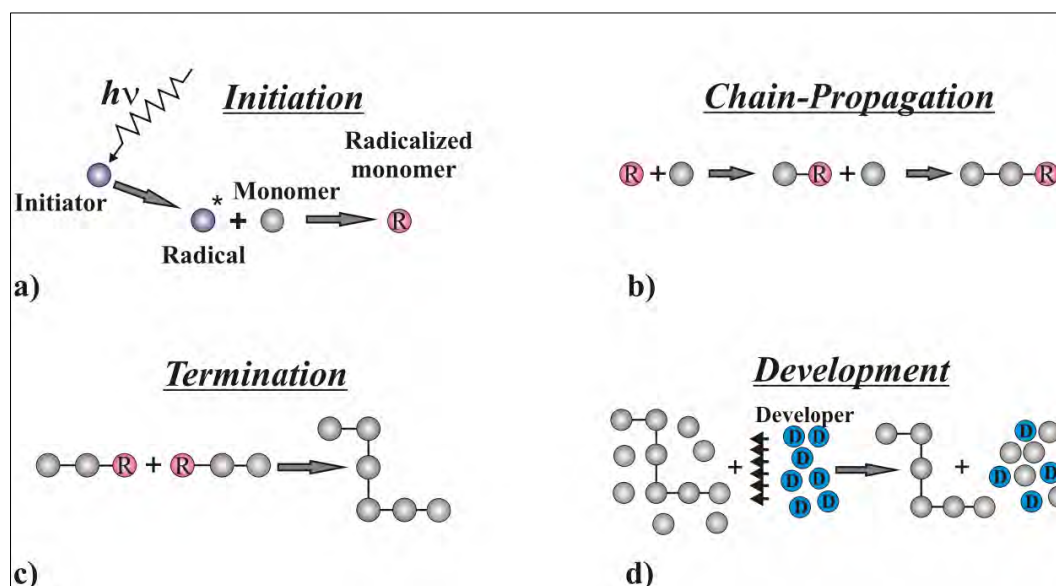
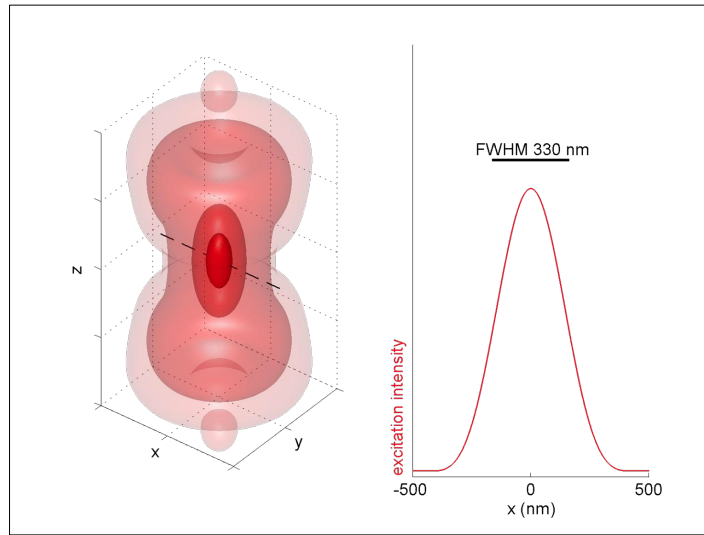


Figure 2. *Photochemistry process.* Photoinitiator molecule absorbs a photon and turns to a radical (a); then it radicalizes monomer and triggers chain-propagation reaction (b); when two radical-monomers meet the chain propagation is terminated (c); during development process the non-polymerized part of the material is washed out leaving only insoluble polymer chains (d) [3].

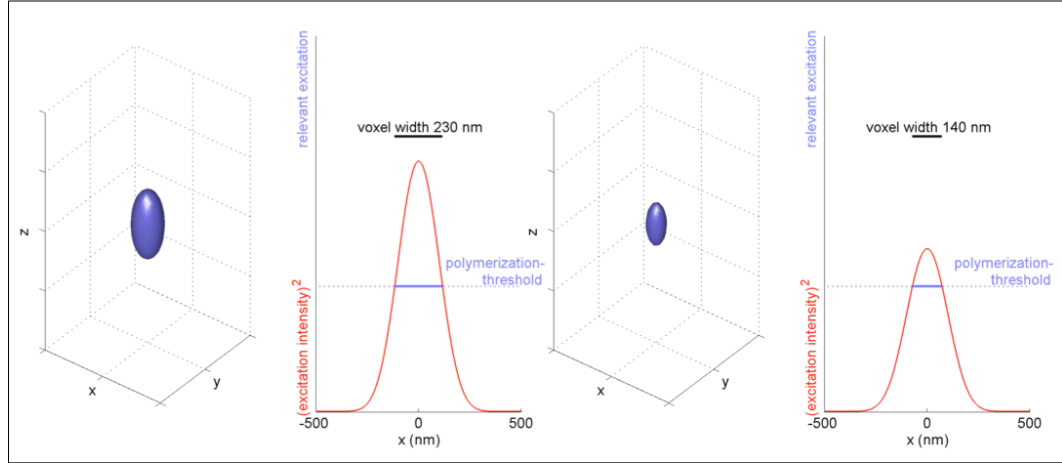
Many resins that polymerize when exposed to UV-light can undergo similar chemical reactions when two photons of near-infrared light are absorbed simultaneously: *two-photon absorption* (TPA) is a nonlinear process in which a molecule simultaneously absorbs two photons of energy $h\nu$ (or $h\nu_1$ and $h\nu_2$, respectively) to attain an excited state of energy of $2h\nu$ (or $h\nu_1 + h\nu_2$) [4]. The quadratic dependence of TPA on incident

intensity implies that for a focused laser beam, the polymerization will only occur at the focal volume, also known as a *voxel* (from volume pixel). Since very high peak intensity is necessary for the TPA process to occur, a femto-second laser is normally exploited for this application. Several models have been developed to describe the shape of the voxel. One of these models makes use of the point spread function (PSF) to describe the spatial distribution of TPA generated with a focused laser beam while other model tries to identify which region of the irradiation spot experiences fluence/intensity higher than the threshold of photomodification (i.e., polymerization, crystalline phase change, melting, structural modification, defect formation, etc) [5, 6]. The representative voxel spatial distribution for both 1-photon and 2-photon can be seen in fig. 3 [7].

Because the absorption probability of TPA depends quadratically on the incident intensity I , this results in a narrower excitation in 3D space, and thus, real 3D objects can be fabricated by scanning the focal spot of the laser inside the photopolymer media. However, one should note that because of this nonlinearity, the voxel has not a symmetric shape but is elongated along the optical axis (in the vertical direction).



(a)



(b)

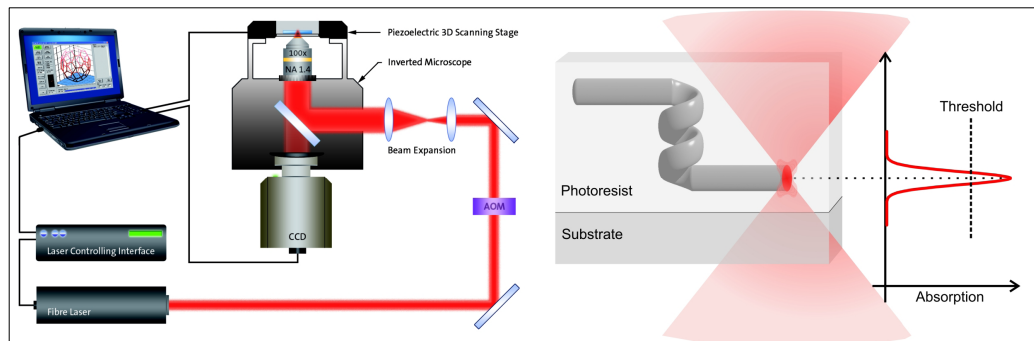
Figure 3. Spatial distribution of: (a) single and (b) two-photon absorption voxel. In (b) on the right it can be seen that two-photon absorption allows to achieve smaller voxel dimensions depending on the magnitude of the intensity with respect to the polymerization threshold [7].

The fabrication tool used is the “Photonic Professional” system, provided by Nanoscribe GmbH (see fig. 4), equipped with a pulsed erbium doped femtosecond fiber laser source at a center wavelength of 780 nm, a motorized coarse positioning stage (x–y–stage) along with a piezoelectric stage moving in a volume of $300\ \mu\text{m} \times 300\ \mu\text{m} \times 300\ \mu\text{m}$ for a fine positioning of the sample.

The laser beam is focused into the PR (Photo Resist) layer using a high numerical aperture oil–immersion objective (N.A. 1.4). The maximum laser power allowed by the machine in a fabrication process is 20 mW [8].



(a)



(b)

Figure 4. Nanoscribe Photonic Professional system: (a) overview of the system; (b) Principle of two photon absorption laser lithography [8].

The writing process is schematically illustrated in fig. 5, consisting in 4 main steps: the PR is first placed on a glass substrate either by drop-casting or spin-coating (step 1) and then the 3D desired pattern is transferred through the two photon polymerization process (step 2); when the writing process is complete (step 3) the release of the structure is obtained after development (step 4).

This fabrication process offers a unique combination of advantages. First, no topological

constraints are present in the fabrication of three-dimensional structures. Second, subdiffraction-limited resolution can be attained by employing laser intensities just above the intensity threshold at which polymerization will occur. Third, movable components can easily be created without the use of sacrificial layers.

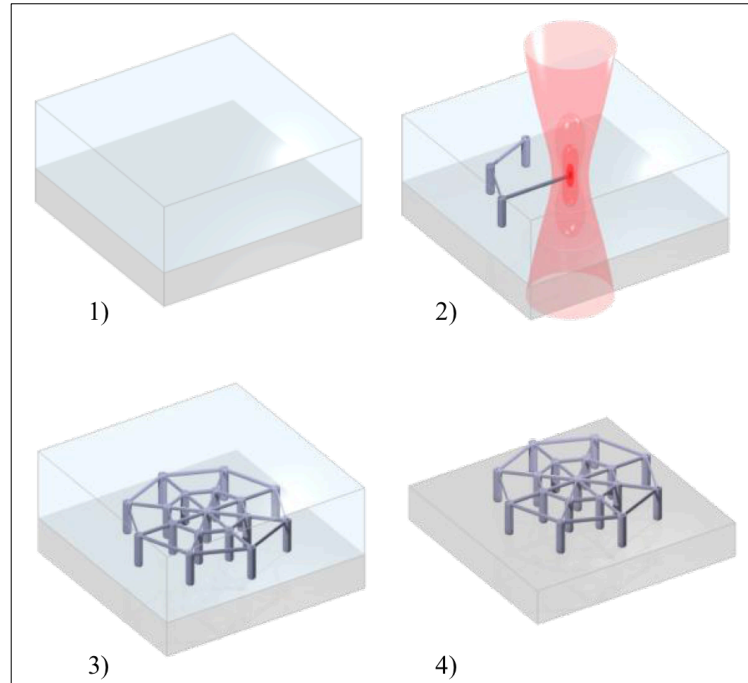


Figure 5. Direct Laser Writing (DLW): Free-standing three-dimensional microstructures can be fabricated by TPP. First the desired pattern is “written” by precise positioning of the laser focal point in the photoresist. Then, the unsolidified remainder of the photoresist is washed away by means of an organic solvent, leaving only the newly fabricated microstructures on the substrate [7].

2.2.1 Two photon lithography: photosensitive material

Photosensitive materials are divided into negative and positive tone. In this work only negative photoresins were used: the exposed volume of a negative resist undergoes photomodification and becomes insoluble in developer. Unexposed material is removed during the sample development, thus revealing the DLW inscribed object.

The photoresist employed in this work is the epoxy-based SU-8 2000 series (from MicroChem): it is supplied as a viscous liquid consisting of an epoxy resin, a solvent and a photoacid generator [9] and is widely used in the conventional photolithography. In fig.6 it is reported the structural diagram of the SU-8 molecule: it is composed of 8 epoxy groups, that are those that will cross-link to give the final polymerized structure.

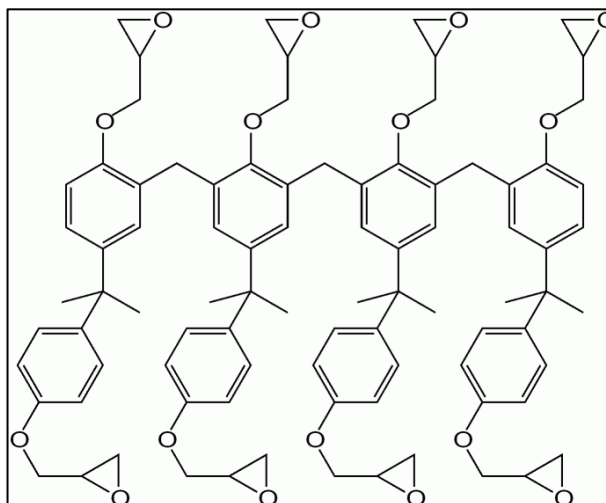


Figure 6. Chemical composition of the main constituent in SU8 photoresist. Eight oligomers are available for a high degree of crosslinking upon photoexposure.

In general the SU-8 is suitable to be used to pattern high aspect ratio structures, its maximum absorption is for ultraviolet (UV) light with a wavelength of the i-line (365 nm), and cyclopentanone are used as the primary solvent for the 2000 series used in this work. When exposed, SU-8's long molecular chains cross-link causing the polymerisation of the material.

SU-8 was originally developed as a photoresist for the microelectronics industry, to provide a high-resolution mask for fabrication of semiconductor devices.

It is now mainly used in the fabrication of microfluidics (mainly via soft lithography, but also with other imprinting techniques such as nanoimprint lithography) and microelectromechanical systems parts. It is also one of the most biocompatible materials known [10] and is often used in BioMEMS as it the case of this work.

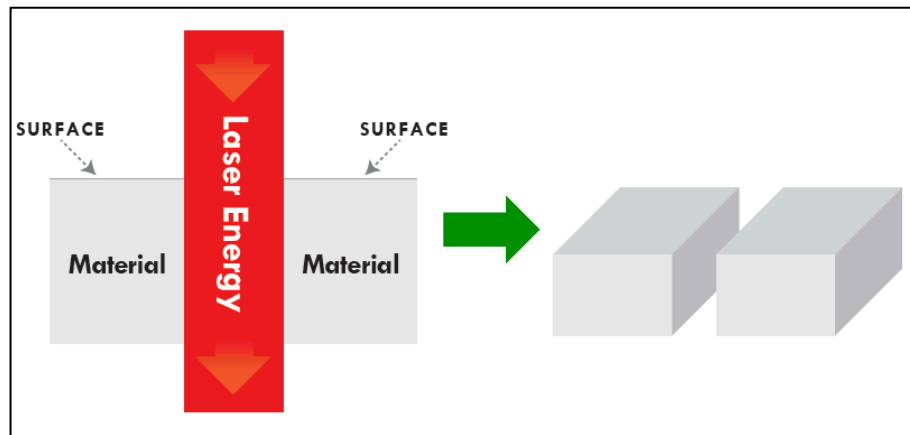
During pre-exposure bake the solvent is evaporated and the material becomes solid: it is crucial to achieve a uniformly dry layer, since inhomogeneities will lead to undesirable variations of photopolymerization threshold. After the pre-exposure bake the SU-8 film becomes solid so that it can be processed in a rigid form, and the produced pattern is *immobilized* throughout the fabrication step: highly complex interconnected structures can be easily produced, and this is particularly advantageous for the fabrication of moving micromechanical components.

Finally, it is worth to note that, in a standard lithography exposure of a chemically amplified PR, a post exposure bake (PEB) is needed to complete the cross-linking phase: it redistributes the photo-generated chemicals and suppresses the standing wave effect; however some works have reported that the patterns survived without PEB treatment in femtosecond laser lithography using a chemically amplified resist SU-8 [11]: on this basis the PEB step was skipped and the structures resulted perfectly defined after development.

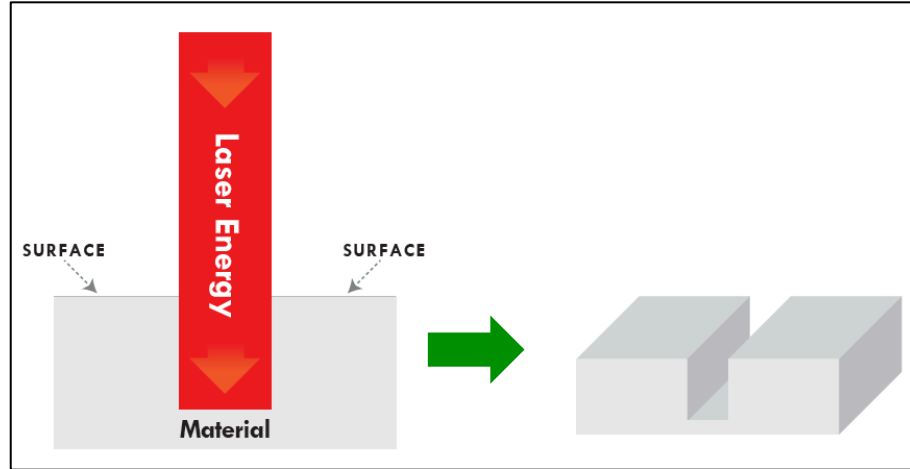
2.3 Laser machining: Laser Cutter

As mentioned in the introductory section, the PDMS based device is built by using the so-called “*laser cutting*” technique, in which a laser beam is directed towards the material to be cut: it is the complete removal and separation of material from the top surface to the bottom surface along a designated path (see fig. 7(a)).

On the other hand, “*laser engraving*” is the removal of material from the top surface down to a specified depth (see fig. 7(b)).



(a)



(b)

Figure 7. Laser cutting (a); Laser engraving (b).

Laser machining is a rapid prototype technique allowing for fast material processing, involves less manufacturing steps and less or no additional chemical reagents and/or solvents. Furthermore, the laser structuring of prototypes for new products or processes is less expensive since the masks can be omitted.

All these features, in combination with the large use of polymeric materials for microfluidic devices fabrication, make laser machining the principal alternative to the standard fabrication techniques such as hot embossing, injection molding, soft lithography, when the resolution requirements are not critical, remaining above the wavelength value (10 μm in our work) [12].

Among the different kind of laser sources, CO_2 lasers have a predominant role in the laser micromachining of polymers due to its excellent absorption in polymers. In facts, one type of laser–matter interaction is absorption where energy is transferred to the material [13]. Depending on the material and laser type, absorption is followed by the conversion of the energy into heat, which is a photothermal mechanism [1].

The first laser ablation of polymers was performed in the 1982, when Y. Kawamura et al. and R. Srinivasan et al. first reported the material removal of polymers with lasers [14, 15].

A photothermal mechanism is usually found for metals, but also for polymers. In the case of metals, excessive heating leads to desorption of the material through vaporization or

sublimation. For high intensities, even ionization and plasma formation can be found. A large number of applications are based on this mechanism of heating via laser light, for example welding and cutting of metals. The high reliability and precision of lasers are key features in this regard.

In the case of polymers, the processes are often more complex, depending on the material, wavelength and time scale. Polymers do not simply vaporize but rather show thermal decomposition upon heating [16]. In general the following mechanisms may appear:

- 1) random chain scission
- 2) end-chain scission, sometimes also called *"unzipping"*

leading to lower molecular weights and formation of volatile species – oligomers or monomer – which undergo vaporization.

The eliminated parts of the polymer are typically lost through the gas phase.

The tool used in this work to laser cut the PDMS is the 8011 Trotec Speedy 100/R (fig. 8) from Trotec Laser GmbH. The machine is equipped with a 12W CO₂ laser source (10,6 µm wavelength) and a working area of 610 mm x 305 mm [17].



Figure 8. Trotec 8011 Speedy 100/R laser cutter [17].

2.3.1 Laser machining materials: polydimethylsiloxane (PDMS)

Polydimethylsiloxane called PDMS or dimethicone is a polymer widely used for the fabrication and prototyping of microfluidic chips.

It is a mineral–organic polymer (a structure containing carbon and silicon) of the siloxane family (word derived from silicon, oxygen and alkane). Apart from microfluidics, it is used as a food additive (E900), in shampoos, and as an anti–foaming agent in beverages or in lubricating oils.

For the fabrication of microfluidic devices, PDMS (liquid) mixed with a cross–linking agent is poured into a microstructured mold and heated to obtain an elastomeric replica of the mold (PDMS cross–linked).

Referring to fig. 9, the empirical formula of PDMS is $(C_2H_6OSi)_n$ and its fragmented formula is $CH_3[Si(CH_3)_2O]_nSi(CH_3)_3$, n being the number of monomers repetitions.

Depending on the size of monomers chain, the non–cross–linked PDMS may be almost liquid (low n) or semi–solid (high n). The siloxane bonds enable to obtain a flexible polymer chain with a high level of viscoelasticity.

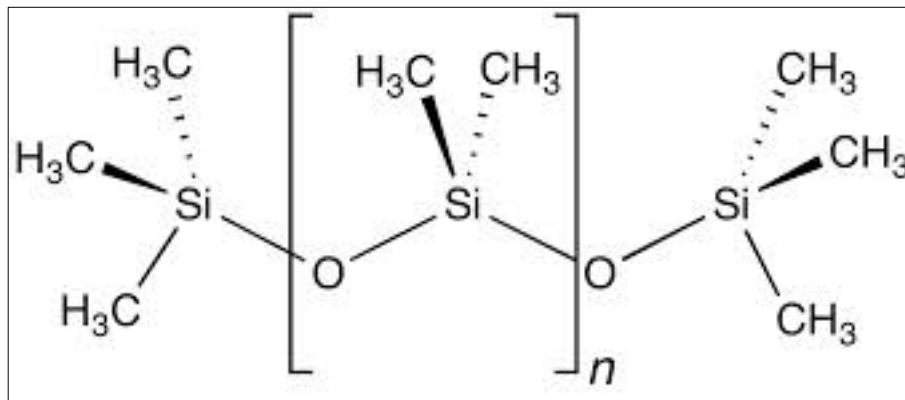


Figure 9. PDMS chemical formula.

PDMS is very popular as material in the fabrication of microfluidic chips primarily for the following reasons:

1. It is transparent at optical frequencies facilitating the observation of contents in micro–channels by naked eyes or through a microscope.
2. It has a low autofluorescence [18].

3. It is considered as bio-compatible (with some restrictions).
4. It bonds tightly to glass or another PDMS layer with a simple plasma treatment. This allows the production of multilayers PDMS devices and enables to take advantage of technological possibilities offered by glass substrates, such as surface functionalisation.

The PDMS used for the fabrication of the suspended microchannel is the BISCO[®] HT-6240 transparent solid silicone, a trade mark of Rogers Corporation: it is available in various thicknesses and manufactured in roll form so that the purchased material is to be processed [19].

References

- [1] Gabriele Maccioni, “Processing Technologies” Lectures Handnotes 2014
- [2] TOPTICA Photonics AG Website
- [3] Mangirdas Malinauskas, Doctoral dissertation, Vilnius 2010
- [4] Chun, W., W. Xiaomei, S. Zongshu, Z. Xian, Z. Guangyong, W. Dong, F. Qi, and J. Minhua, "Optical properties of a new two-photon absorbing chromophore," *Applied Optics* 40, 2475-8 (2001).
- [5] Maruo, S. and S. Kawata. Two-photon-absorbed photopolymerization for three-dimensional microfabrication. 1997. Nagoya, Japan: IEEE.
- [6] Juodkazis, S., V. Mizeikis, K.K. Seet, M. Miwa, and H. Misawa, "Twophoton lithography of nanorods in SU-8 photoresist," *Nanotechnology* 16, 846-849 (2005).
- [7] Gerhard Balthasar, “Three-Dimensional Direct Laser Writing”, Nanoscribe technical presentation, October 25th 2012.
- [8] Nanoscribe User Manual.
- [9] SU-8 2000 series Data Sheet.
- [10] Nemani, Krishnamurthy V.; Moodie, Karen L.; Brennick, Jeoffry B.; Su, Alison; Gimi, Barjor (October 2013). "In vitro and in vivo evaluation of SU-8 biocompatibility". *Materials Science and Engineering: C* 33 (7): 4453–4459.
- [11] M. Mizoshiri, Y. Hirata, J. Nishii, H. Nishiyama, *OPTICS EXPRESS* 8, 19 (2011) 7673 – 7679

- [12] Mohammadreza Riahi Shahid Beheshti University/Laser and Plasma Research Institute Iran CO₂ Laser and Micro–Fluidics.
- [13] J.C. Miller and R.F. Haglund. Laser Ablation and Desorption. Academic Press, San Diego, 1998]. Depending on the material and laser type, absorption is followed by the conversion of the energy into heat, which is a photothermal mechanism.
- [14] Kawamura, Y., K. Toyoda, and S. Namba, Effective Deep Ultraviolet Photoetching Of Poly(Methyl Methacrylate) By An Excimer Laser. Applied Physics Letters, 1982. 40(5): p. 374-375.
- [15] Srinivasan, R. and V. Mayne–Banton, Self–Developing Photoetching Of Poly(Ethylene–Terephthalate) Films By Far Ultraviolet Excimer Laser–Radiation. Applied Physics Letters, 1982. 41(6): p. 576-578.
- [16] C.L. Beyler and M.M. Hirschler. Thermal decomposition of polymers. In P. J. DiNenno and pp., editors, SFPE Handbook of Fire Protection Engineering, page 1110. NFPA, Quincy, 3rd edition edition, 2001.
- [17] Trotec Speedy 100 User Manual.
- [18] Piruska, A. et al. The autofluorescence of plastic materials and chips measured under laser irradiation. Lab. Chip 5, 1348–1354 (2005).
- [19] BISCO® HT–6240 Data Sheet.

Chapter 3

SU-8-based Suspended Microchannel Resonator for bio-mechanical sensing applications

In this chapter the whole workflow for the suspended microchannel resonator device, from the design to the optical realization and characterization, is presented. Aiming to reduce the fabrication time, a highly-versatile fabrication strategy is proposed, based on a shell-writing procedure. With respect to standard microfabrication techniques, requiring several technological steps to obtain suspended hollow structures, this method allows to fabricate complex SMR sensors in only one fabrication step, by virtue of its intrinsically three-dimensional nature. The realized resonant structure was characterized by laser-doppler vibrometry, showing good agreement with finite-element methods simulations.

3.1 Device design

As mentioned earlier in the first chapter, the suspended microchannel resonator (SMR) proposed here is made of epoxy-based SU-8 photoresist (PR), a material widely used in MEMS and microfluidic applications by virtue of its mechanical and optical properties. Two different designs have been investigated in reference to different inlet/outlet position.

3.1.1 Finite element method based modelling of the suspended microchannel resonator

The SMR described in fig. 1 has been designed by using a finite element method (FEM) analysis package such as COMSOL Multiphysics.

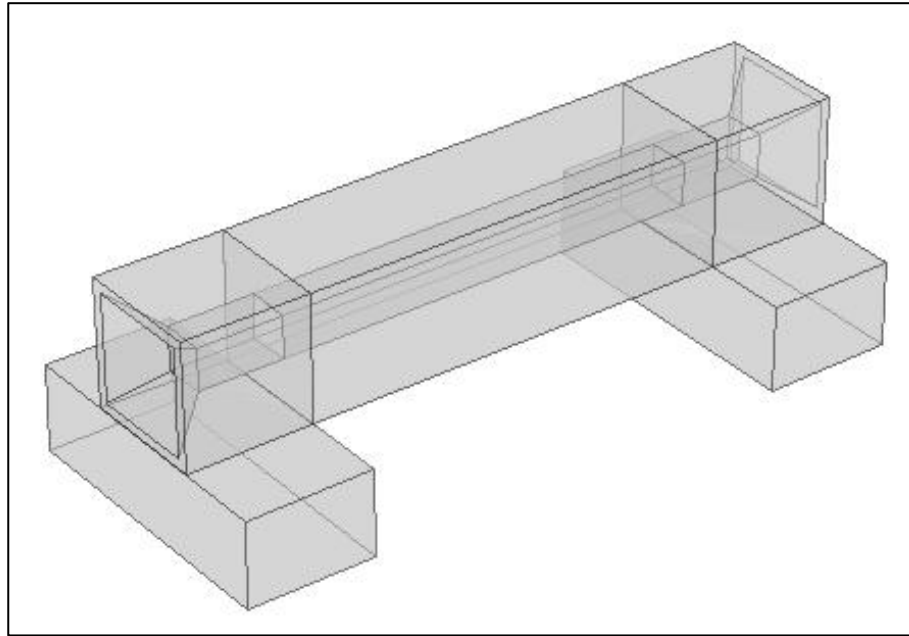
The FEM analysis is a good choice for solving multiphysics partial differential equations over complex physical domains. The finite element method breaks a 3D complex geometry into many smaller, often tetrahedral, discrete regions and approximates the complex partial differential equations (PDEs) with a simpler system of equations having a numerically stable solution in each discrete region. However it is important to remember that modelling a real system means always approximate it at best of possibilities. A good model of a microsystems is composed always by more than one set of PDEs, but as the number of equations increases the computing power required may become unsustainable. In the major of case it is possible to reach a compromise between the model accuracy and computing degree.

The discretization of the structure was created through a mesh of the type "*free tetrahedral*", that divides the property in tetrahedra. The variables of interest are calculated in the vertices of each tetrahedra. In particular, the geometry has been discretized with an "*extremely fine*" mesh option in the "Element size" section, with the following parameters, compatible with the device dimensions: maximum element size is $3,2\ \mu\text{m}$, minimum element size is $0,032\ \mu\text{m}$, maximum element growth rate of 1,3 a curvature factor of 0,2 and 1 for the resolution of narrow regions. To compute the resonant frequency of the structure, a "*Solid Mechanics*" physics is used together with a "*Linear Elastic Material Model*". For the viscosity damping in air an "*Acoustic-Solid Interaction*" physics is used. In order to obtain the natural frequency and the mode shape of the device, an "*eigenfrequency study*" is performed on the geometry having fixed supporting blocks and the suspended section is free to oscillate, as illustrated in figure 3.

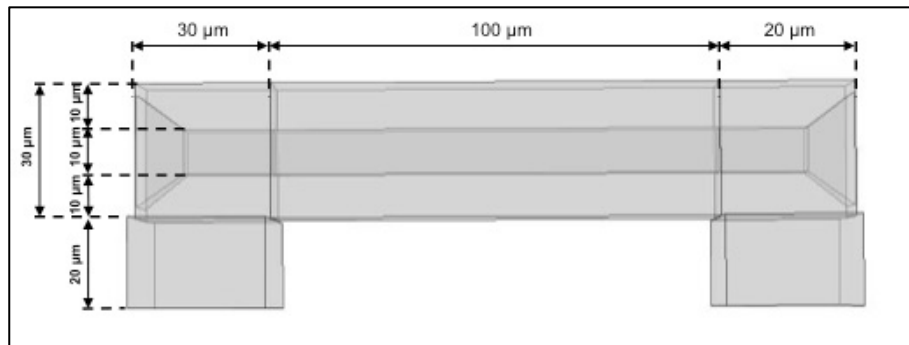
The material SU-8 properties have been selected from the built-in library where the in-plane and out-of-plane Young's modulus of $3.2 \pm 0.2\ \text{GPa}$ and $5.9 \pm 0.9\ \text{GPa}$ respectively, and a Poisson's ratio of 0.33 are used as input mechanical parameters [2].

3.1.2 First design

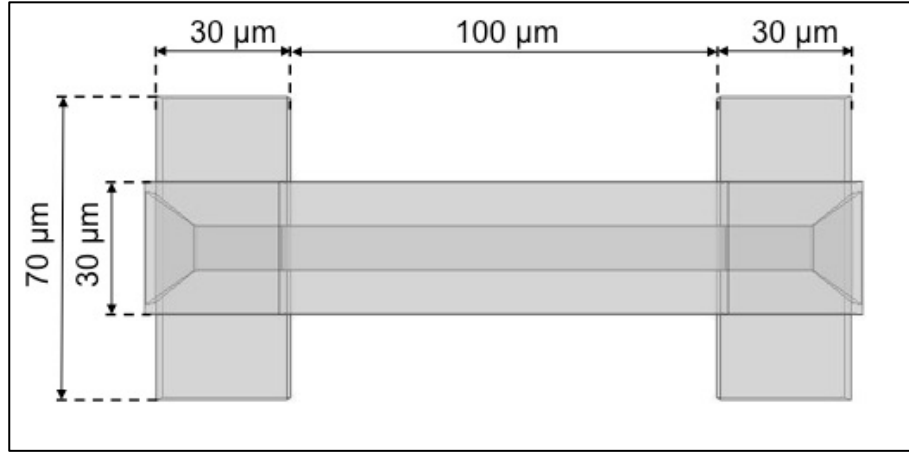
The first explored SMR geometry is illustrated in fig.1, and consists of a hollow and doubly-clamped beam, having a 100 μm –long suspended channel with 10 $\mu\text{m} \times 10 \mu\text{m}$ internal cross–section and 30 $\mu\text{m} \times 30 \mu\text{m}$ external cross–section. The beam is clamped to the supporting blocks (30 $\mu\text{m} \times 70 \mu\text{m} \times 20 \mu\text{m}$) with funnel shaped inlet/outlet (I/O) [1].



(a)



(b)



(c)

Figure 1. Geometry of the suspended microchannel resonator: three dimensional view (a); lateral (b) and top (c) representation respectively.

Figure 2 shows the mesh discretization produced as described above.

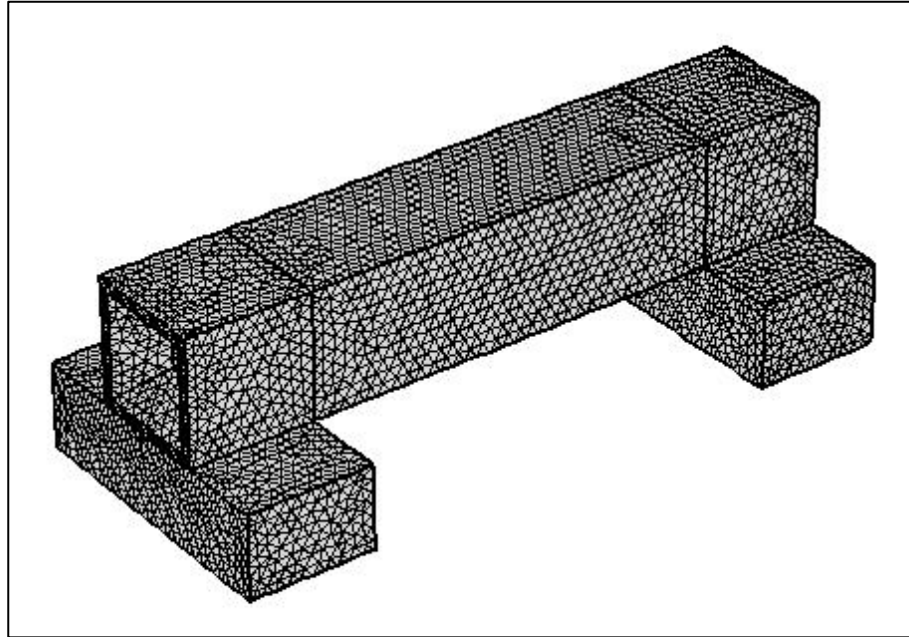


Figure 2. Resulting mesh of the device in fig. 1. It consists of 102840 domain elements, 12078 boundary elements, and 1052 edge elements.

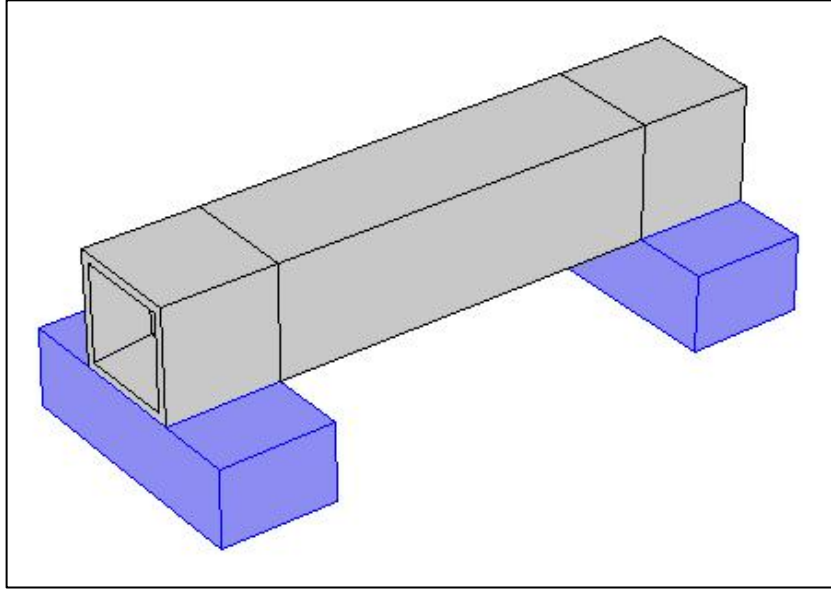


Figure 3. Suspended microchannel resonator showing the fixed constrains adopted in the simulations.

FEM simulation output returned $f_0 = 2,4876$ MHz for the trasversal mode in vacuum (representative images of the simulated vertical displacements for the first out-of-plane mode are displayed in fig. 4).

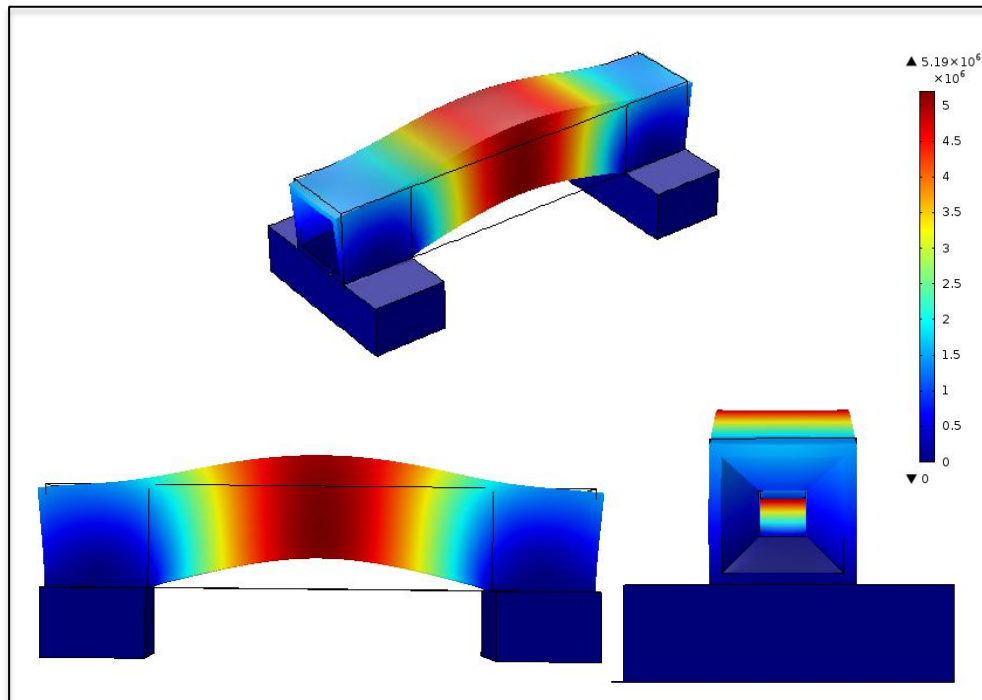


Figure 4. The designed SMR is represented in a FEM simulation showing the first resonant mode.

3.1.3 Second design

The resonant frequency of the previous device was too high as demanding a high-performing electronics for the read-out section. The value of 1MHz was then set as upper limit for the resonant frequency. Since the resonant frequency scales with $1/L^2$ (with L being the length of the suspended part), a longer channel is required to have a lower resonance: a parametric study has been performed to define the minimum length – as a function of the channel thickness – to obtain a resonant frequency lower than 1MHz for the first resonant mode. As reported in the plot of fig. 5 the channel has to be longer than 150 μm for a channel as thick as 10 μm .

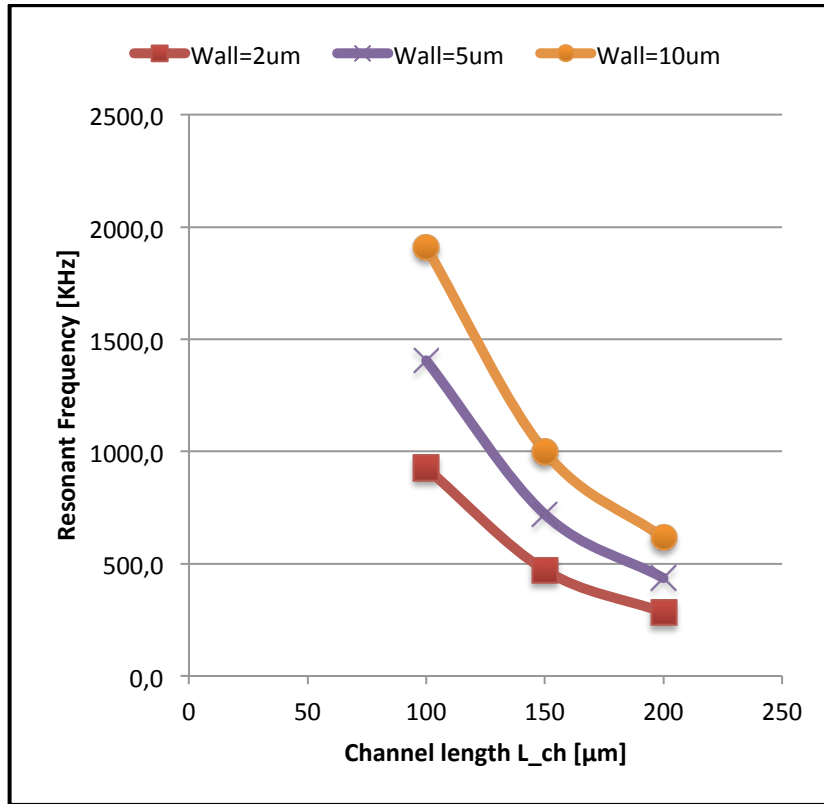
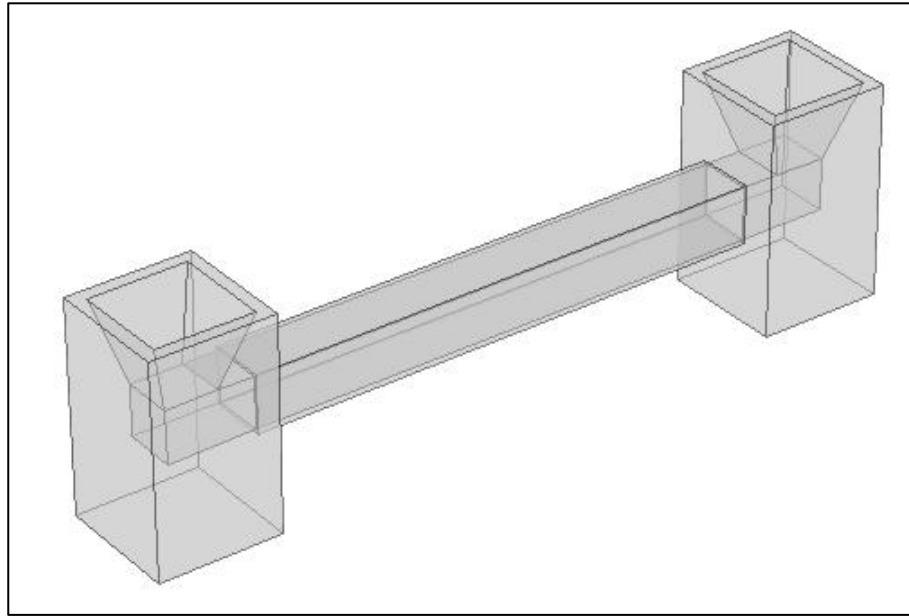


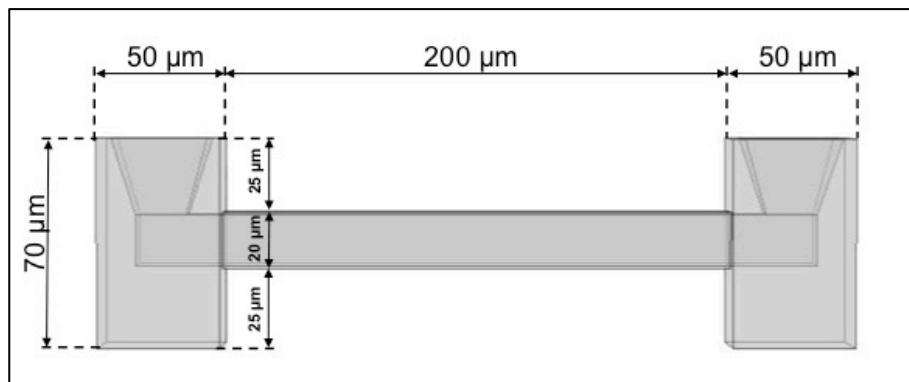
Figure 5. Resonant frequency vs channel length for different wall thickness: for a 10 μm -thick channel the length has to be longer than 150 μm .

The new SMR geometry is illustrated in fig. 6 and fig. 7, and consists of a hollow and doubly clamped beam, having a 200 μm -long suspended channel with $20 \mu\text{m} \times 20 \mu\text{m}$ internal cross-section. The beam is clamped to the supporting blocks ($50 \mu\text{m} \times 50 \mu\text{m} \times$

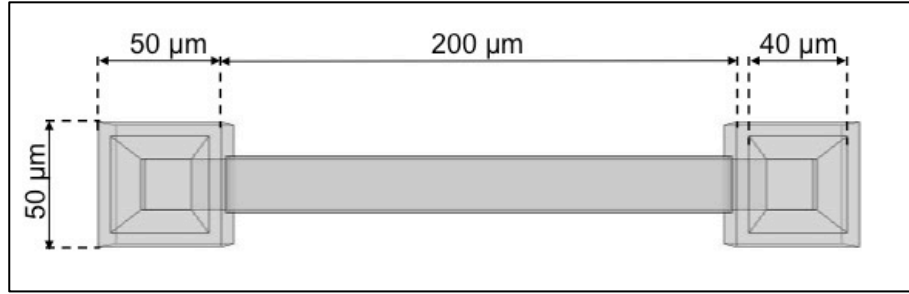
70 μm) with inlet/outlet sections ($40\text{ }\mu\text{m} \times 40\text{ }\mu\text{m}$) and to a glass substrate, allowing the deflection of the suspended region [3]. For instance, the design of the device itself was further developed, with the insertion of vertical inlet/outlet instead of longitudinal ones. The whole device reaches a total length of 300 μm as the total length of the writing volume.



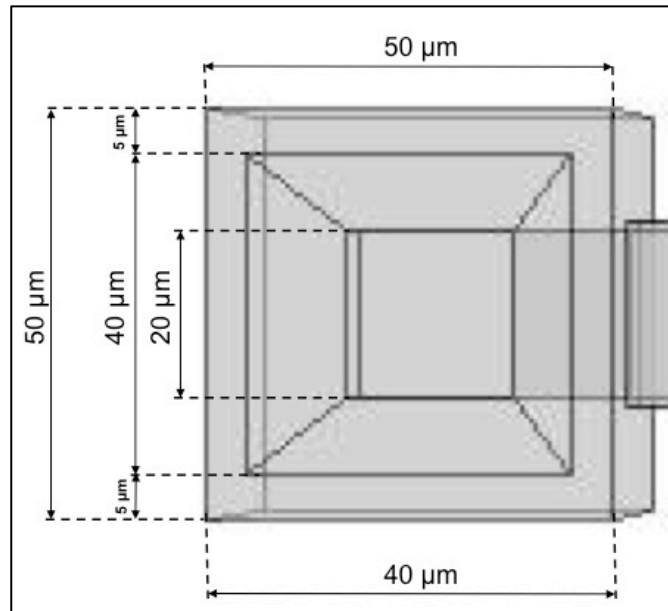
(a)



(b)



(c)



(d)

Figure 6. Geometry of the suspended microchannel resonator: three dimensional view (a); lateral (b), top (c) and inlet port detail (d) respectively.

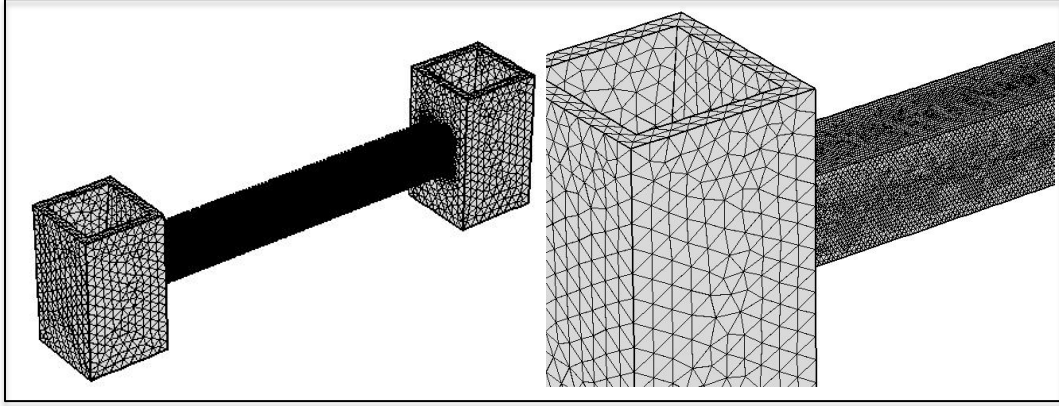


Figure 7. Mesh of the new geometry: the suspended part has a finer discretization as shown in the zoomed image, giving much more precise results. The complete mesh consists of 179494 domain elements, 84286 boundary elements, and 2286 edge elements.

For this device the calculation outputs returned $f_{0,vacuum} = 898$ kHz and $f_{0,air} = 881$ kHz, for vacuum and air background respectively (representative image of the simulated vertical displacements for the first out-of-plane mode is displayed in fig. 8). The difference between $f_{0,vacuum}$ and $f_{0,air}$ can be assigned to the influence of the air viscosity on the mechanical behavior of the resonator (damping effect).

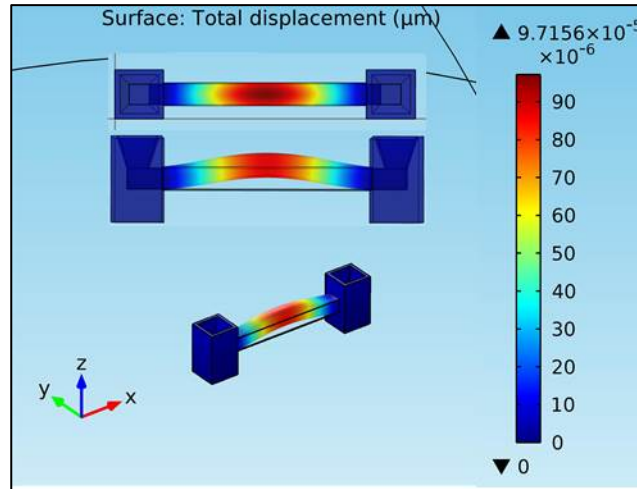


Figure 8. The designed SMR is represented in a FEM simulation showing the first resonant mode in air environment. The inset shows the top and side views [3].

3.2 Fabrication process

As already mentioned in the previous sections of the thesis, the SMR was fabricated by means of a two-photon lithography system provided by Nanoscribe GmbH and equipped with a 780 nm femtosecond-pulsed laser and a piezoelectric sample stage moving in a volume of $300\text{ }\mu\text{m} \times 300\text{ }\mu\text{m} \times 300\text{ }\mu\text{m}$. The laser beam is focused into the PR layer using a high numerical aperture oil-immersion objective (N.A. 1.4). The machine features a maximum laser power (LP) of 20 mW during the fabrication process, allowing the PR to undergo both photoactivation and polymerization during the same exposure period. Indeed, at the used powers the peak intensity confined in the focal region is high enough to activate the photoacid generator contained in the PR and to locally increase the SU-8 temperature, thus inducing also thermal cross-linking [4].

One of the main advantages of TPL is the possibility to write into a relatively wide volume ($27 \times 10^6\text{ }\mu\text{m}^3$ in our case) with an in-plane resolution below 100 nm. However, when realizing big structures as the one described here, the writing time can exceed 24h. In order to reduce fabrication time we have employed a shell-writing technique, consisting in exposing to the two-photon beam only the outer contours of the object instead of polymerizing the entire volume. To minimize the exposed shell thickness, some main considerations should be taken into account. (i) A fully sealed shell is needed to confine the unexposed material inside the shell and prevent mechanical properties modifications induced by the interaction with the environment. (ii) External surface should ensure that the developer solution does not percolate into the structure through the exposed walls, swelling the device volume. (iii) Edges should be thick enough to warrant structural stability. Indeed, due to material densification while curing and post-processing, volume shrinkage of the microstructure can take place [5]: since the amount of material is the same before and after polymerization, the volume reduction can induce mechanical cracks and accumulate stress.

The definition of the suitable writing parameters like laser power and scanning speed (or update rates in points per second), was achieved by performing a systematic variation of these parameters on an array of test structures in SU-8: this is reported in fig. 9, where a matrix of squared blocks having a $10\text{ }\mu\text{m}$ side have been polymerized at

different LPs and update rates. The values of the powers are in percentage of the maximum power available (20mW): 4mW, 6mW and 8mW were used during this test.

The relationship between the update rate parameter and the scanning speed in $\mu\text{m}/\text{sec}$ is:

$$\text{scanning speed } [\mu\text{m}/\text{sec}] = \text{update rate} \times \text{point distance}$$

where point distance is a parameter indicating the distance in nm between the written points, and its default value is set to 100nm. For the values shown in the picture the scanning speeds are: 10, 15, 20, 25, 30, 35 and 40 $\mu\text{m}/\text{sec}$. At this stage the combination of 6mW (LP = 30) and 20 $\mu\text{m}/\text{sec}$ (update rate of 200) was chosen, giving optimal results as will be further shown in the text. Also, from fig. 9 it is possible to see that some blocks are not in the original position: probably the action of the developer solution was strong enough to remove them, most likely due to poor adhesion.

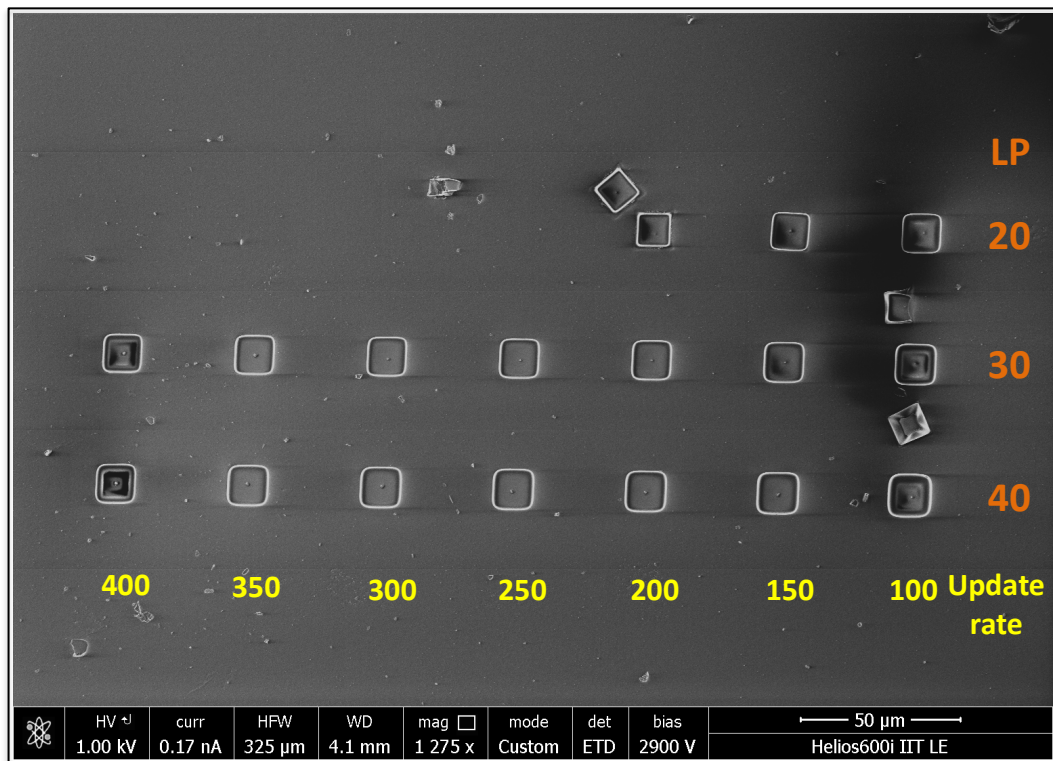
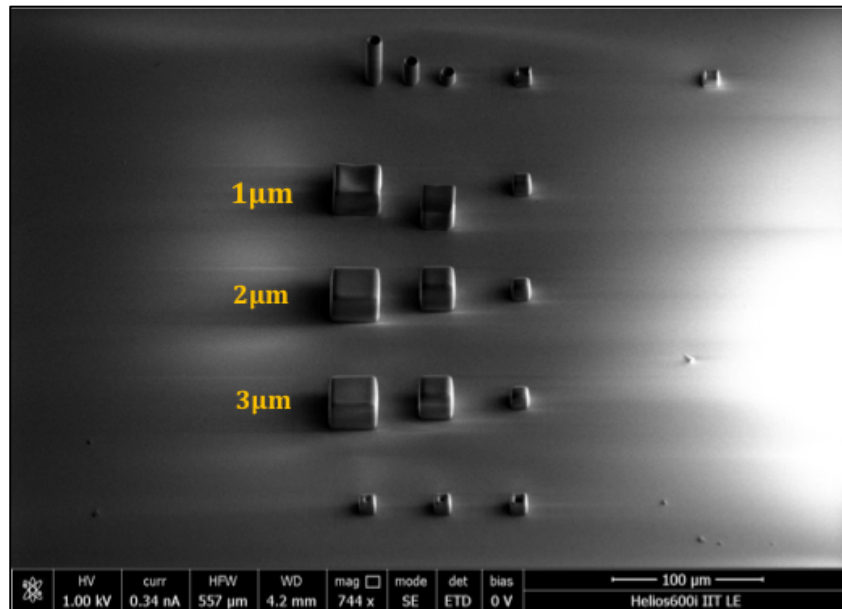


Figure 9. Matrix of SU-8 squared blocks polymerized with different laser power–scanning speed combinations. The blocks have the same side length (10 μm). Some blocks have moved from the original position, indicating some possible adhesion issues.

In order to define the correct polymerization thickness, arrays of 10 μm -high parallelepipeds with different shell thicknesses (1 μm , 2 μm , 3 μm) and different side dimensions (10 $\mu\text{m} \times 10 \mu\text{m}$, 20 $\mu\text{m} \times 20 \mu\text{m}$, 30 $\mu\text{m} \times 30 \mu\text{m}$) have been used as test structures. The fabrication tests have been performed on a spin-coated SU-8 2025 film (film thickness $\sim 20 \mu\text{m}$) deposited on a circular microscope coverslip and, following SU-8 operation procedures [6,7], soft-baked on a hot plate (3 min @ 65°C and 8 min @ 95°C) and then exposed by TPL. The SU-8 cross-linking was obtained with a laser power tuned at 6 mW and writing speed of 20 $\mu\text{m}/\text{s}$. At the end of the writing process, the sample was developed in PGMEA for ~ 10 min and rinsed with IPA. Fig. 10 shows representative outcomes of these tests. A 1 μm -thick shell (fig. 10(b)) leads to a pronounced distortion of the outer surface, while for 2 μm thickness this effect was less pronounced (fig. 10(c)). This is not the case for the structures having a contour of 3 μm (fig. 10(d)), which preserved their original shape and have not been swelled nor deformed during the development step, thus promising a good structural stability. It is worth mentioning that the internal untreated region can, however, melt at $\sim 50^\circ\text{C}$, setting the higher temperature operation limit for devices realized by exploiting this fabrication procedure.



(a)

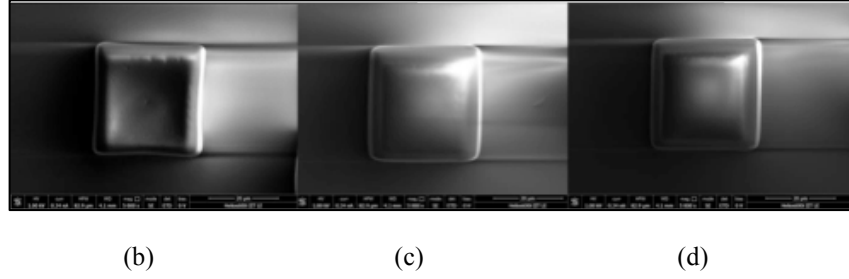


Figure 10. Test geometries to determine the minimum shell thickness to avoid percolation of the development solution: (a) global view of the array consisting of a set of three cubes of different size, written with different contour thicknesses (from the top to the bottom: 1 μm , 2 μm , 3 μm respectively); (b), (c) and (d): detail of a 30 μm -side cube with 1 μm , 2 μm and 3 μm thick shell respectively (microphotographs have the same 20 μm scale bar) [3].

The optimum thickness identified above was therefore used for the fabrication of the SMR device into a 80 μm -thick SU-8 2025 film.

Representative SEM images of the both realized SMRs are illustrated in fig. 11(a) and fig. 12(a), while a detail of one I/O region is displayed in fig. 11(b) and fig. 12(b), respectively. Good stability of I/O section was observed, despite only 3 μm -thick shell was polymerized. The internal channel can be clearly identified through the transmission optical microscopy (figs. 11(c) and 12(c)).

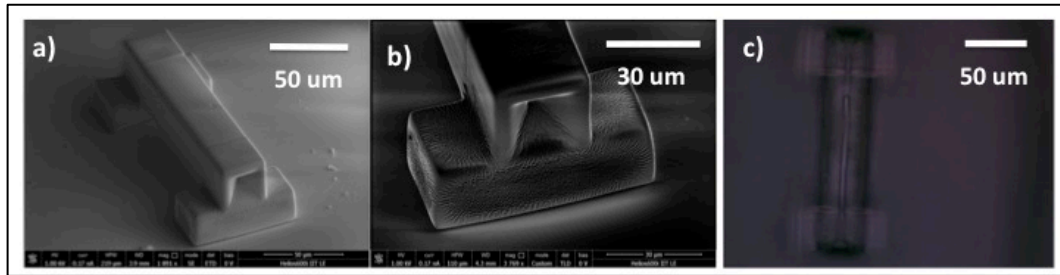
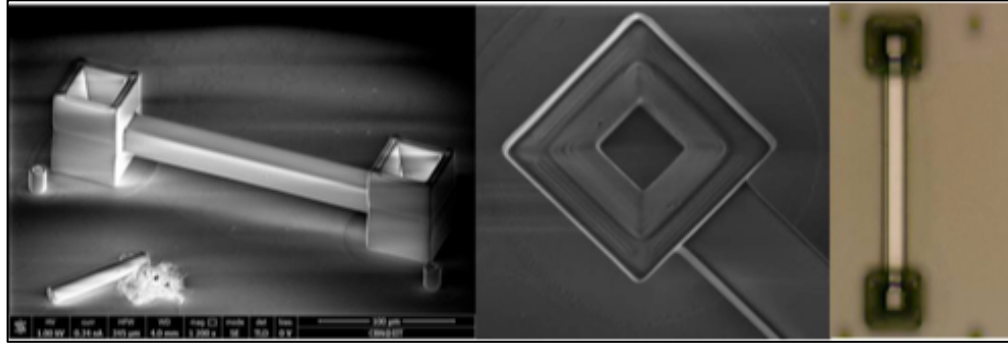


Figure 11. Scanning electron microscopy micrograph of the fabricated device: 3D view (a); detail of the inlet/outlet (b); Optical microscope image showing the complete development of the microchannel (c) [8].



(a)

(b)

(c)

Figure 12. Pictures of the realized device: SEM images (a), (b); (c) Optical inspection revealing the internal channel [3].

A second SEM picture collected from the first microfabricated SMR (figure 13) shows that one end of the device is detached from the glass substrate, slightly bending upwards. This is due to a residual mechanical stress that arises from the photon polymerization, leading to deformations: in this case there is one end that is not attached to the substrate, indicating that the stress induced in the structure is compressive. The characterization results in the next section will show the mechanical consequences of this anomaly.

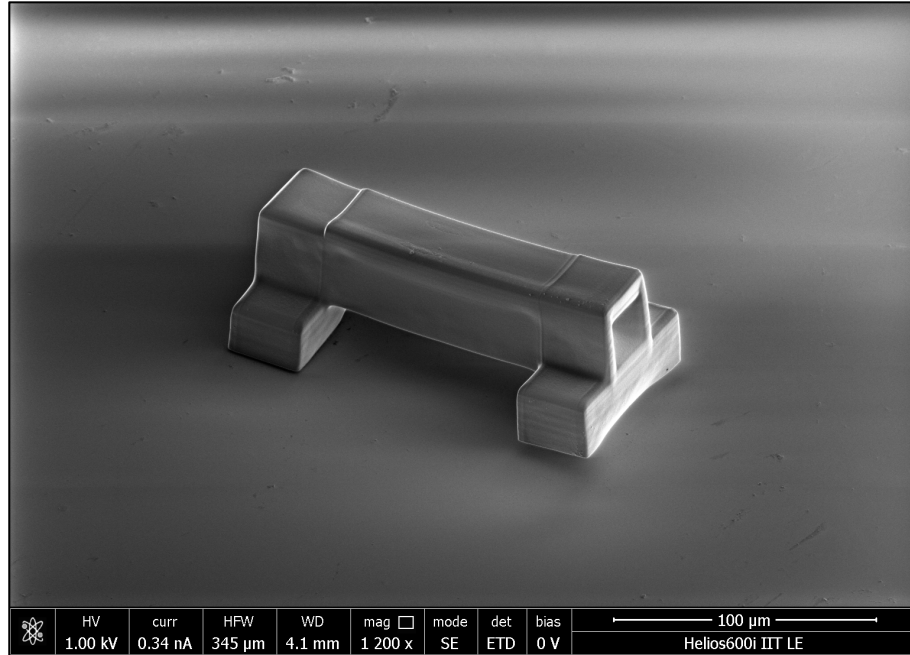


Figure 13. SEM micrograph of the realized device (first design). One end is not attached to the substrate, indicating that the beam is slightly bending upwards, due to the induced stress in the structure compressive.

In order to avoid this drawback and have a stress-free structure (also improving the adhesion to the substrate), a quick thermal treatment (10 min @ 65°C and 20 min @ 95°C) to reduce the stress in the second SMR processing was performed just after exposure and the development time was set to ~ 15 min to allow complete development of the channel: this step was introduced in the fabrication process of the second design.

Finally, to confirm the uniform complete development of the internal channel for the second device, the beam was cut by focused ion beam milling (30 kV, 9.3 nA) to analyze the suspended bridge cross-section (fig. 14): the shell thickness all around the channel resulted to be fully polymerized, since it is written for the entire thickness. The mechanical properties of the unpolymers and polymerized regions can, in principle, be slightly different. In spite of this, the channel wall, completely polymerized, allows this procedure not to perturb the mechanical properties of the designed SMR.

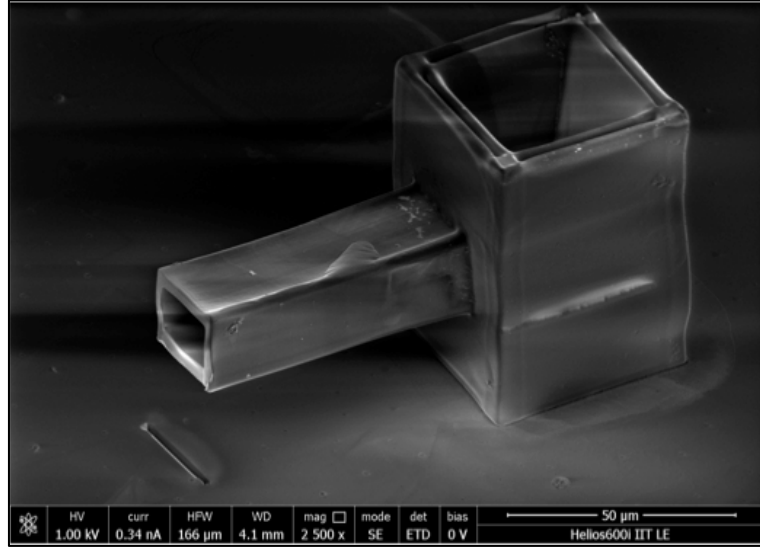
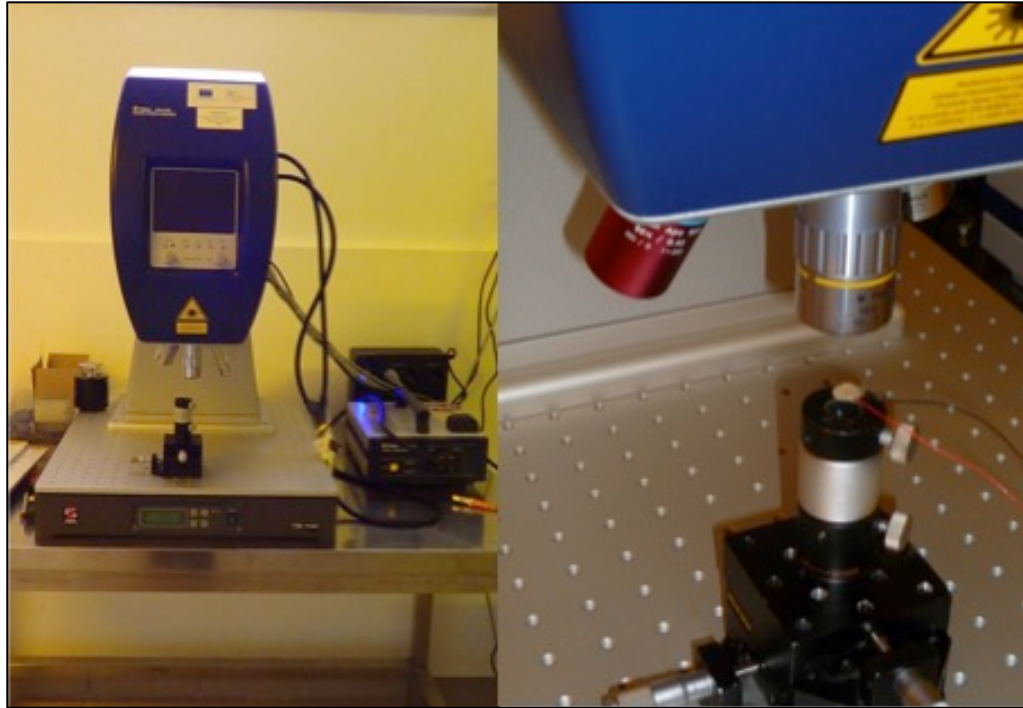


Figure 14. SEM image showing that the internal channel has come to a complete development and the bridge wall is completely polymerized [3].

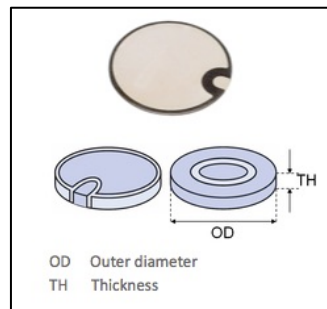
3.3 Characterization

The fabricated devices have been characterized to identify the first transverse resonant mode (shape and frequency). Laser-Doppler vibrometer in fig. 15 (LDV, Polytec Vibrometer MSA500) in conjunction with a piezo-actuated disc PIC 255 in fig. 15(c) – 10mm diameter and 2mm thick, Physik Instrumente GmbH – [9] was employed to measure the mechanical properties of the sensor. The SMR was secured on an electrically driven piezo-disc which forces the microstructure to vibrate. The employed scanning LDV system enables non-contact measurements in real time for the characterization of out-of-plane vibrational behavior for determining the amplitude of the displacement at any sample point (vertical resolution of a few tens of picometers) [10]. The characterization tool is based on the Doppler-effect that allows to sense the frequency shift of back scattered light from a moving object with respect to the reference laser frequency (fig. 16). Exploiting a heterodyne detection technique, the Laser-Doppler vibrometry measurements relate the change in the optical path length due to mechanical vibrations with both the velocity and displacement of the object.



(a)

(b)



(c)

Figure 15. Polytech Vibrometer MSA 500: (a) overview; (b) Detail on the piezoelectric disc carrying the DUT; (c) the piezoelectric component PIC 255 used as actuator for the structure.

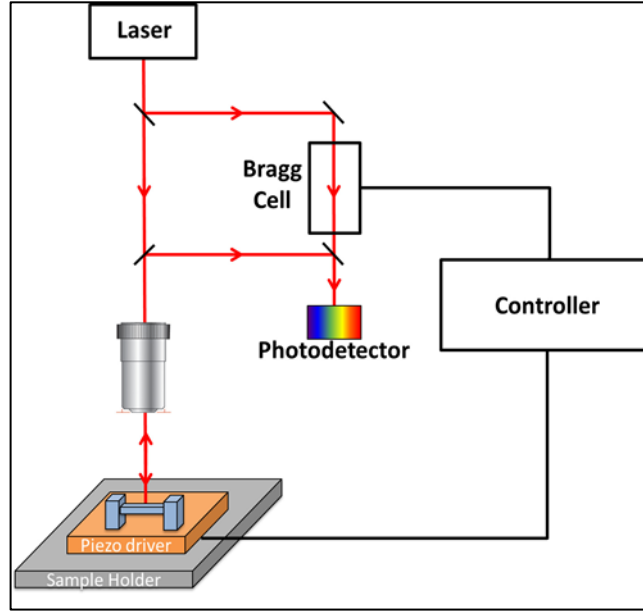


Figure 16. Experimental setup implementing vibrometry measurements by Doppler effect [3].

To minimize the noise level, the “frequency domain averaging” mode was used, where the averaged spectrum is obtained from all the values of the FFT spectra of the collected sequence of points on the sample.

Fig. 17 shows a frame of the oscillating microchannel (second design) in its first mode from a software reconstruction: the highest displacement (about 70 pm) was recorded by LDV in the central area of the suspended beam.

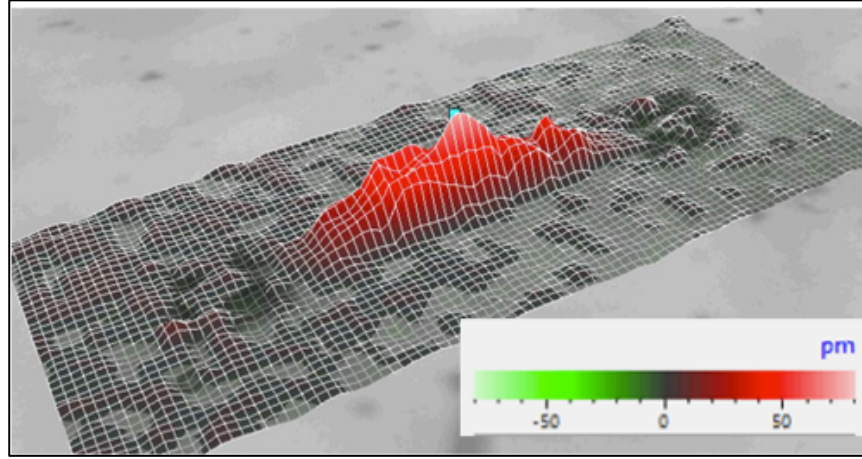


Figure 17. Three-dimensional reconstruction via LDV software of the first resonant mode for the second design [3].

The experimental data of the beam displacement are reported in fig. 18 where the red curve acts as a guide for the reader's eyes, allowing to identify the peak corresponding to the first flexural mode of resonance at 880 kHz, in good agreement with the simulation done in air.

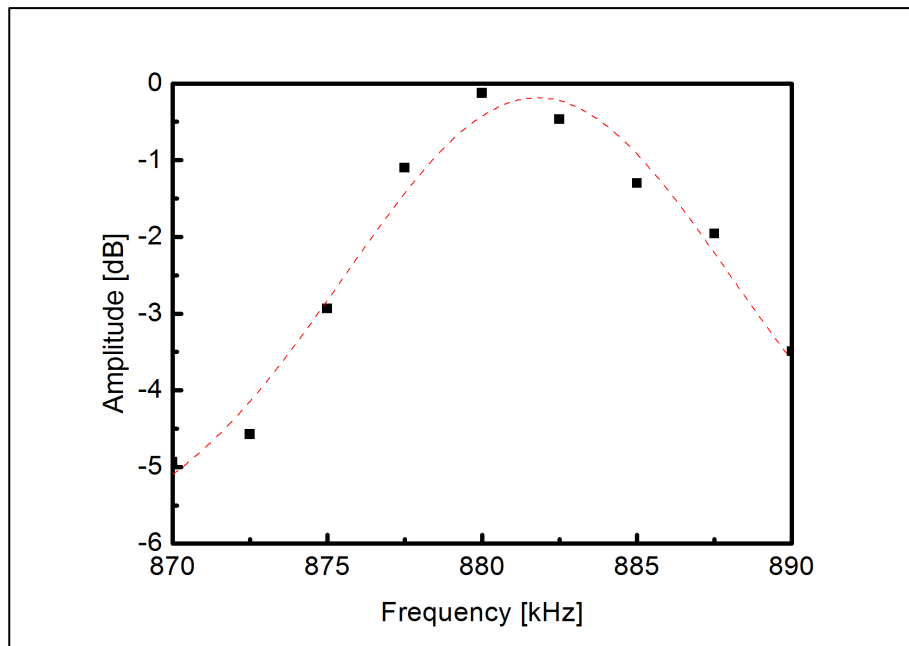


Figure 18. LDV measurement: frequency spectrum of the out-of-plane displacement for the first resonant mode (peak at 880 kHz); the dashed line is intended as a guide for the eyes [3].

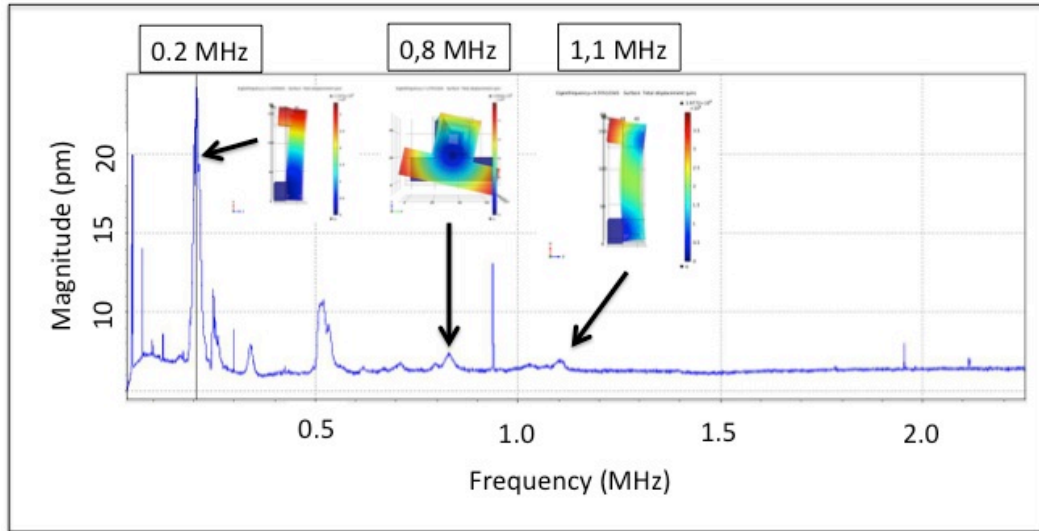
From the measured data we can derive the quality factor Q of the system from the relationship:

$$Q = \frac{f_0}{BW} \quad (10)$$

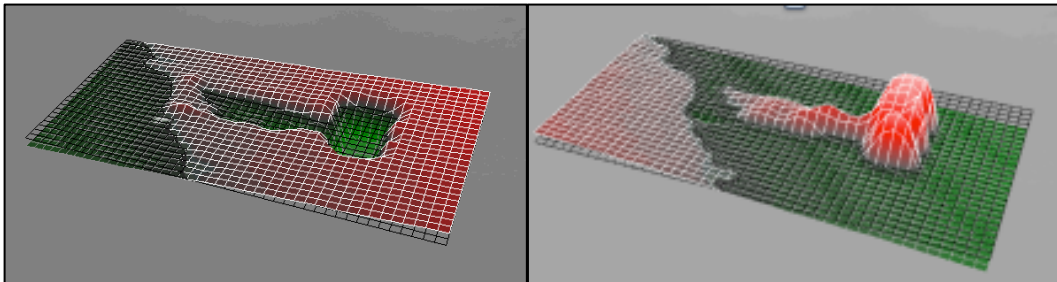
where f_0 is the resonance frequency and BW represents the bandwidth of the system, corresponding to the frequency range where Q reduces up to 3 dB of the maximum. From the measured dataset, we obtained $Q \sim 60$ for the fundamental mode, which – taking into account the non negligible losses from the piezo to the glass die and to the SMR – is considered a reasonable value for structures operating in air environment.

As reference, the SMR belonging to the first design has been characterized, and the characterization response is reported in fig. 19: in particular, the frequency spectrum reported in fig. 19(a), shows different harmonic behaviour for this device. As previously discussed in fact one end of the channel is detached from the substrate surface, resulting in both lower resonant frequencies and different mode shapes. In particular a first flexural mode at 0,2 MHz can be recognized, where the beam responds like a cantilever: this is clearly visible from the software video reconstruction in fig. 19(b), showing two frames of the time response with the detached end that is moving up and down.

Other two modes are identified in fig. 19(a): at 0,8 MHz there is a torsional mode thanks to the detached end, while at 1,1 MHz a second flexural mode is visible.



(a)



(b)

Figure 19. The measured frequency response in air is shown in (a) for the first design device. The peaks are located at different frequencies than expected, and also the mode shapes are different: due to the fact that the device has one end detached from the substrate, it behaves like a cantilever. The software reconstruction in the time domain of the beam clearly shows this, with the “free” end moving up and down (b).

References

- [1] C. Accoto, A. Quattieri, F. Pisanello, C. Ricciardi, F. Pirri, M. De Vittorio, F. Rizzi, “Two-photon direct laser writing in SU8 epoxy resin of a suspended microchannel resonant bio-mechanical sensor for liquid chemical analyses”, presentation at the 39th International Conference on Micro and Nano Engineering, London 2013
- [2] R. Feng, R. J. Farris, “The characterization of thermal and elastic constants for an epoxy photoresist SU8 coating”, J. Mater. Sci., vol. 37, no.22 pp. 4793–4799, Nov. 2002
- [3] C. Accoto, A. Quattieri, F. Pisanello, C. Ricciardi, F. Pirri, M. De Vittorio, F. Rizzi, “Two-Photon Polymerization Lithography and Laser Doppler Vibrometry of a SU-8-based Suspended Microchannel Resonator”, IEEE Journal of Microelectromechanical System, vol. 24 , no. 4
- [4] G. Witzgall, R. Vrijen, E. Yablonovitch, V. Doan, B. J. Schwartz, “Single-shot two-photon exposure of commercial photoresist for the production of three-dimensional structures”, Opt. Lett., vol. 23, no. 22, pp. 1745–1747, Nov. 1998
- [5] M. Malinauskas, “Fabrication of functional 3D micro/nanostructures by laser multiphoton polymerization technique”, Ph.D. dissertation, Dept. Quant. Elec., Vilnius Univ., Vilnius, LT, 2010
- [6] SU–8 2000 Processing Guidelines, Microchem
- [7] SU–8 2000 series Data Sheet
- [8] F. Rizzi, C. Accoto, S. Stassi, S. Marasso, A. Quattieri, F. Pisanello, C. Ricciardi, F. Pirri, M. De Vittorio, “Litografia Laser a due fotoni per la fabbricazione di sensori bio-meccanici microfluidici per la diagnostica chimica di inquinanti in liquido”, XIV Giornata Mondiale dell’Acqua: Convegno “Gestione Sostenibile del Mediterraneo” at Accademia Nazionale dei Lincei, Rome 2014
- [9] Piezoelectric Ceramic Products Catalog, Physik Instrumente
- [10] MSA500 User Manual, Polytec GmbH

Chapter 4

MEMS–based Parametric Sensing of Biomolecular Species in Microfluidic Channels

This chapter presents a novel resonant–based detector that senses biomolecular markers by monitoring the parametric oscillations of a fixed–fixed beam embedded at the end of the microfluidic separation channel. Finite element method analysis are used to evaluate the dynamic behavior of the structures. Fabrication and characterization results are presented and discussed: scanning electrons microscope (SEM) is used as inspection technique, and the testing phase is based on laser–Doppler vibrometry technique.

4.1 Device design

As discussed in the first chapter, the development of a novel resonant–based detector, that senses biomolecular markers by monitoring the parametric oscillations of a fixed–fixed beam embedded at the end of the microfluidic separation channel (as illustrated below in figure 1), is investigated.

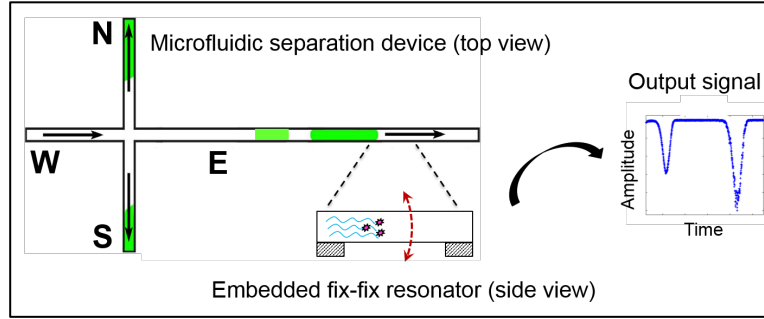


Figure 1. Schematic description of the proposed approach: microfluidic separation and parametric detection device. Complex samples are first separated into their elementary components by microcapillary electrophoresis. By monitoring the parametric oscillation of the embedded fixed–fixed resonator, the detection of different species can be made without any sample labeling.

4.1.1 First design

The suitability of PDMS to be employed for parametric resonance, is investigated through the realization of a resonant microchannel entirely made in PDMS (fig. 2) by Laser Material Processing.

The device is composed by two layers of PDMS with dimensions of $25\text{mm} \times 15\text{mm}$ and a thickness in the order of $250\mu\text{m}$. In the central region, the suspended part has measures of $2,5\text{mm}$ in length, $0,9\text{mm}$ in width, whereas the microfluidic channel presents a cross–section of $450\mu\text{m} \times 150\mu\text{m}$, since these are the values for the fabricated device (as reported in the next section).

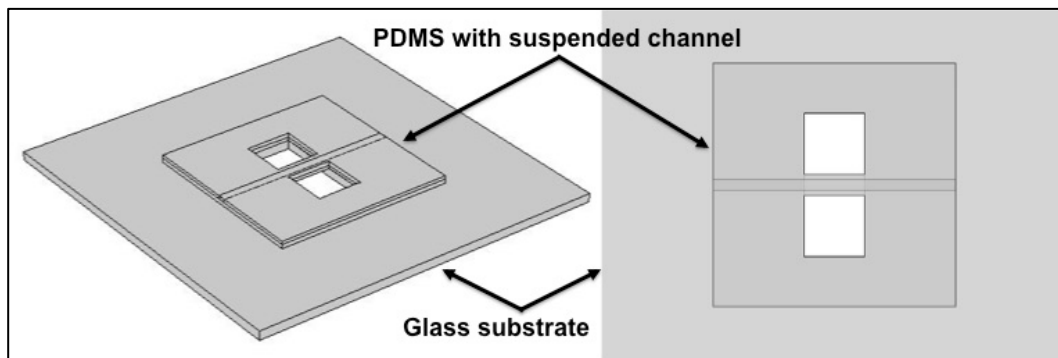


Figure 2. Schematic representation of the microfluidic channel in PDMS: 3D representation on the left and top – view on the right. The inlet/outlet port are not shown here.

4.1.1.1 Modelling of the suspended microchannel resonator

Also in this case, the SMR described in fig. 1 was designed by using COMSOL Multiphysics.

The discretization of the structure was created through a mesh of the type *"free tetrahedral"* : it is chosen to discretize the geometry with the *"custom"* option in the *"Element size"* section, with the following parameters: maximum element size is 500 μm , minimum element size is 10 μm , maximum element growth rate of 2 a curvature factor of 0,6 and 0,5 for the resolution of narrow regions.

As far as the material properties are concerning, a Young's modulus 870kPa and 0,499 for the Poisson's ratio [1] have been chosen: note that for the latter parameter, there are a number of documents which suggest that an accurate value for PDMS's Poisson's ratio is ≈ 0.5 [2,3,4] with values of 0.499 being employed in order to avoid incorrect calculation of infinite moduli. Here we employ the commonly accepted approximation of 0.499 in all simulations [5].

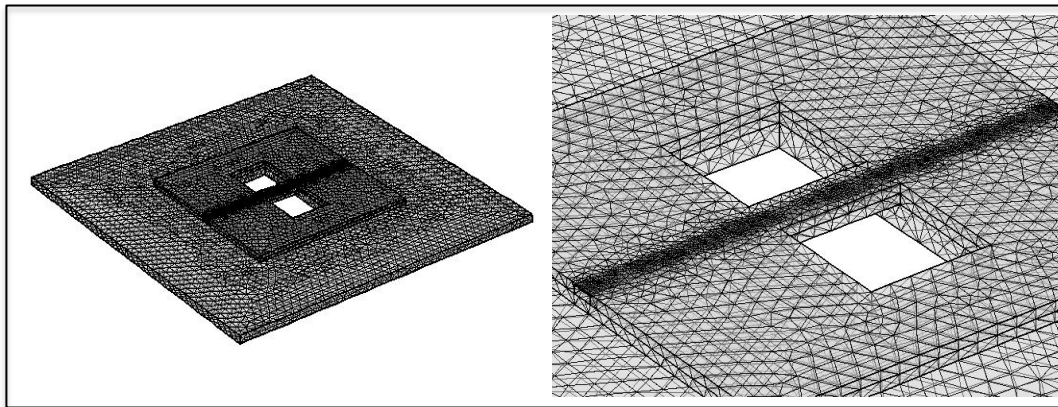


Figure 3. Mesh of the new geometry: the top part of the channel has a finer discretization as shown in the zoomed image, due to the fact that it is the smallest dimension of the entire geometry. In this configuration the complete mesh consists of 38916 domain elements, 18000 boundary elements, and 1278 edge elements: figure 3 shows the discretization produced as described above.

To compute the resonant frequency of the structure, a *"Solid Mechanics"* physics analysis is used together with a *"Linear Elastic Material Model"*.

In order to obtain the natural frequency and the mode shape of the device, an

“*eigenfrequency study*” is performed on the geometry having in the suspended section the only movable part.

With the previously reported dimensions and material characteristics, the FEM simulations give a resonant frequency of 1,545kHz for the first transversal mode, illustrated in fig. 4.

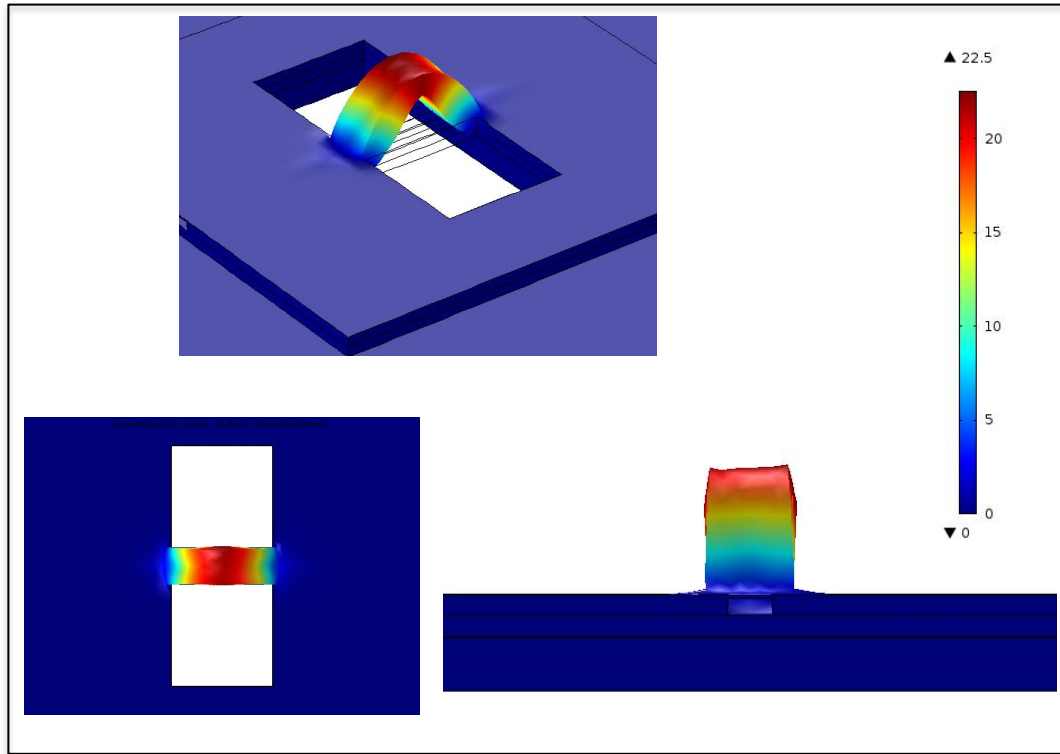


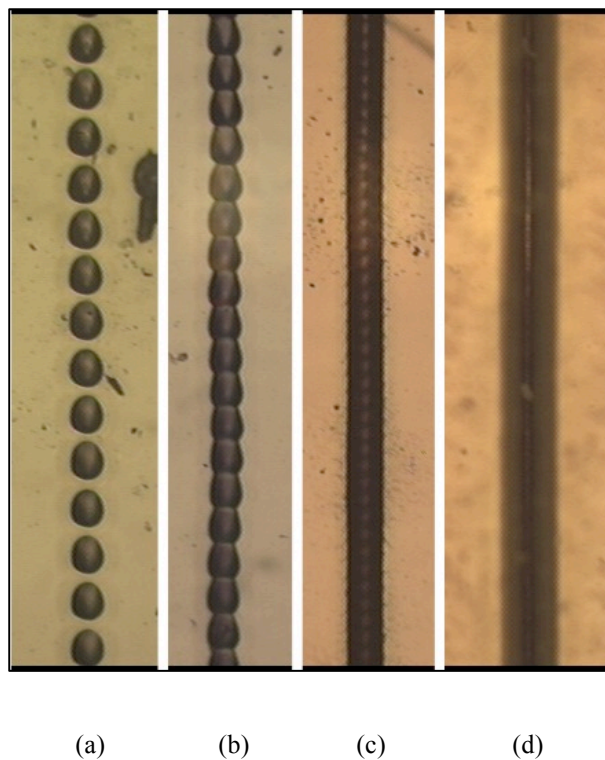
Figure 4. The designed microfluidic channel is represented in a FEM simulation showing the first resonant mode in air environment.

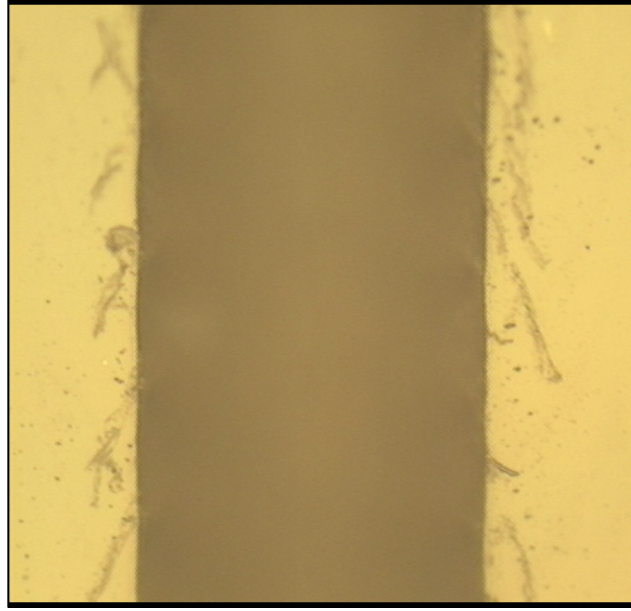
4.2 Fabrication process

4.2.1 Process optimization

There are three main parameters controlling the settings of the laser-cutting machine: laser power, scanning speed and pulses per inch (PPI), which work together to determine the depth and smoothness of cut patterns. Different combinations of these

three parameters can result in different spatial printing resolutions. The relation between the laser parameters and cutting profile of in patterning PDMS was widely studied in [6]. These three parameters of pulsed CO₂ laser were optimized for cutting PDMS layers of different thickness, realising the required patterns with ideal profile. In order to optimize parameters of laser cutting, various tests with different settings of parameters were conducted. Four engraving profiles of lines on a PDMS film with a thickness of 250 μ m are shown in fig. 5. It is found that the fourth setting (laser power: 0,6W; scanning speed: 4,5cm/s; PPI: 500) is more suitable, by which a line with smoother edge and fewer dust residue was obtained. Although the resolution of CO₂ laser cutting is not as high as that of photolithography using expensive and hard chromium masks, it is comparable to prototyping processes using printed transparent masks and adequate for the fabrication of microfluidic devices in many applications [7]. In addition, compared with conventional soft lithography process required to construct patterns on PDMS, the laser cutting method is simple, fast and low cost, which show great advantages in microfluidic chips fabrication.





(e)

Figure 5. Microscopic pictures showing the influence of laser parameters on engraving profiles. Lines were cut on a 250 μ m thick PDMS film by setting laser power, scanning speed and PPI at (a) 0.6W, 10cm/s, 100; (b) 0.6W, 10cm/s, 500; (c) 0.6W, 5cm/s, 500; and (d) 0.6W, 4,5cm/s, 500; (e) 50X zoom of line written with parameters in (d) showing a fairly clean and sharp profile.

4.2.2 Device fabrication

The device is composed by two layers of PDMS (25mm \times 15mm) simultaneously laser-cut from sheets of 250 μ m ca. thickness along with two squared holes (2,5mm \times 2,5mm) in the central region, defining the suspended part, where the channel is engraved through one further step of laser ablation.

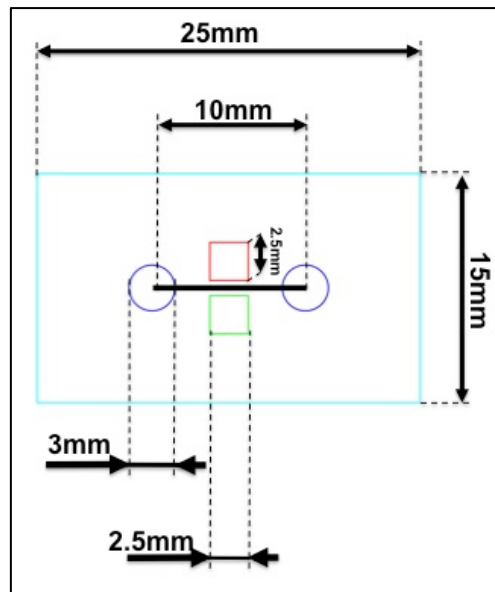
The PDMS has been processed using a laser power (LP) of 12% of the maximum power (namely 1,44W) and a velocity of 1,8cm/s for the parts to be cut, whereas LP = 5% (namely 0,6W) and a velocity of 4,5cm/s to engrave the channel were used as the materials settings. In fig. 6(a) it is reported the layout of the device drawn in CorelDRAW and loaded in the laser cutter software: the black line represents the engraved region while the remaining colors (red, blue, green and turquoise) are edges to be cut; after the cut, the PDMS parts were cleaned with IPA and rinsed with nitrogen

flow.

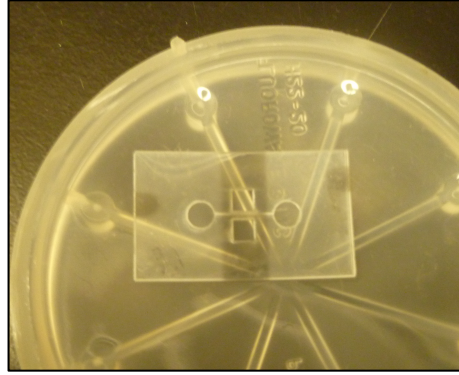
The final device is obtained by bonding together the two PDMS layer according to the following developed protocol for the PDMS to PDMS bonding:

- 10min UV–Ozone surface treatment
- Geometry alignment under the microscope
- 25min at 0,4MPa for intimate contact
- 45min on hot plate at 90°C

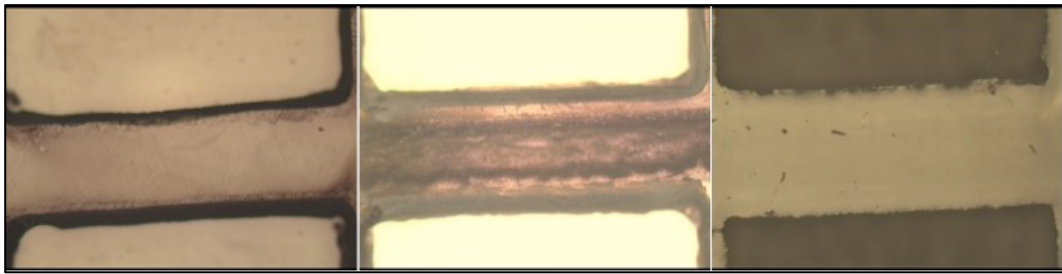
Figure 7 shows the results during a SEM inspection. The cross section of the sample was sputter–coated with a gold–palladium alloy prior to the SEM imaging.



(a)



(b)

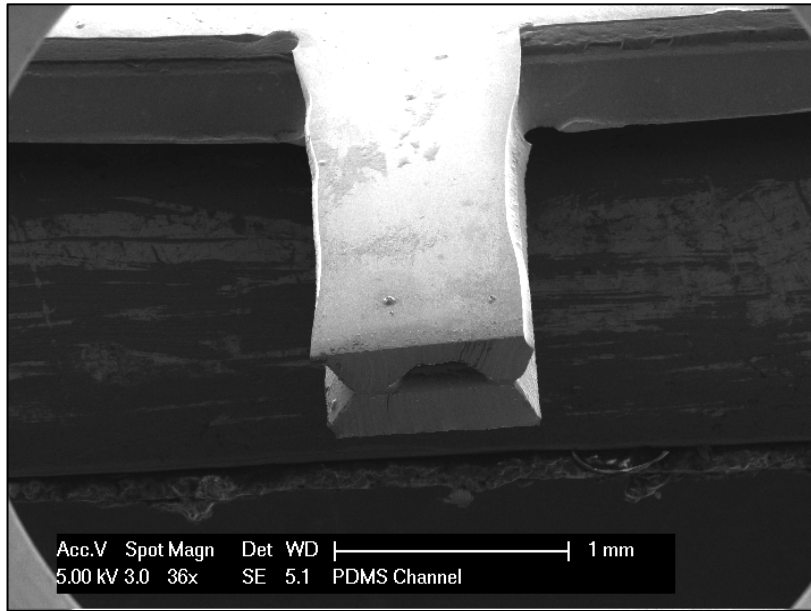


(c)

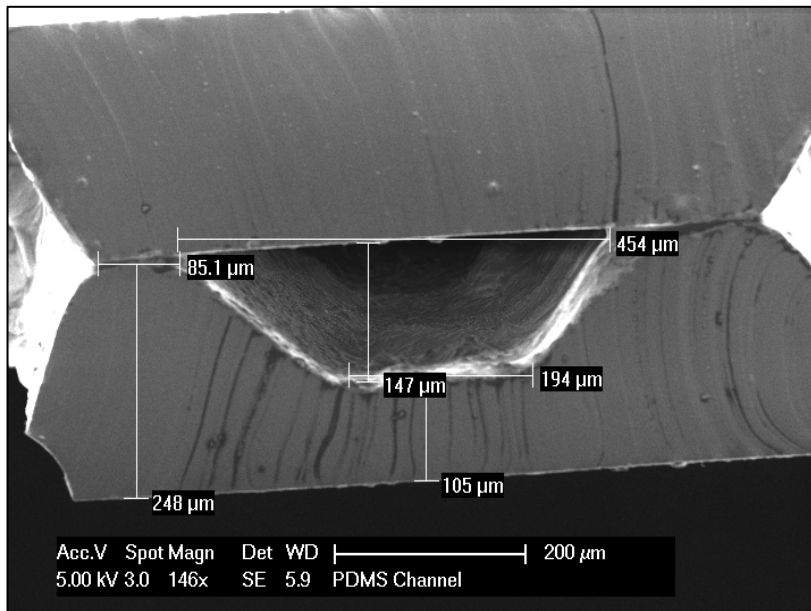
(d)

(e)

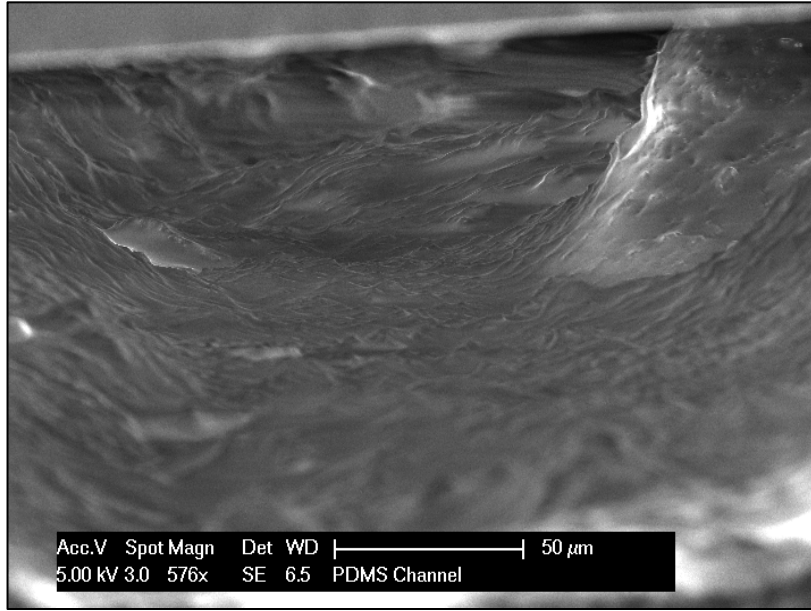
Figure 6. Fabrication results: layout with dimensions of the geometry used for laser-cut (a). The realized PDMS device in (b): by comparison with the upper image (a) we can see that the design has been transferred with high fidelity. (c), (d) and (e) are images of the suspended part only from the optical microscope: the open channel (before bonding) in the center allows us to identify the engraved area and the sidewalls.



(a)



(b)



(c)

Figure 7. Pictures from a SEM inspection of the realized device: the channel was cut in order to verify the geometry and dimension of the channel (a), (b); (c) shows the roughness of the engraved part of the channel.

4.3 Characterization

4.3.1 Bonding examination

The bonding strength of the manufactured channel was examined by a simple leakage test, which was performed by introducing a mixed solution of deionized (DI) water and a red food dye (employed for visualization). Two small flexible tubes – serving as interface for the fluid transport – were connected to the inlet and outlet of the tested device using an epoxy glue. A syringe pump was used to manually introduce the liquid solution to channel and no leakage was observed in our experiment (fig. 8).



Figure 8. Leakage test: a liquid solution composed of deionized water and a red food dye is manually injected through a syringe to verify that the bond between the two PDMS layers is hermetic. Starting from the left to the right, we can see (yellow arrow) that the fluid has reached the outlet of the channel and increases in volume (by further increase the pressure on the syringe) without any leak.

4.3.2 Dynamic characterization

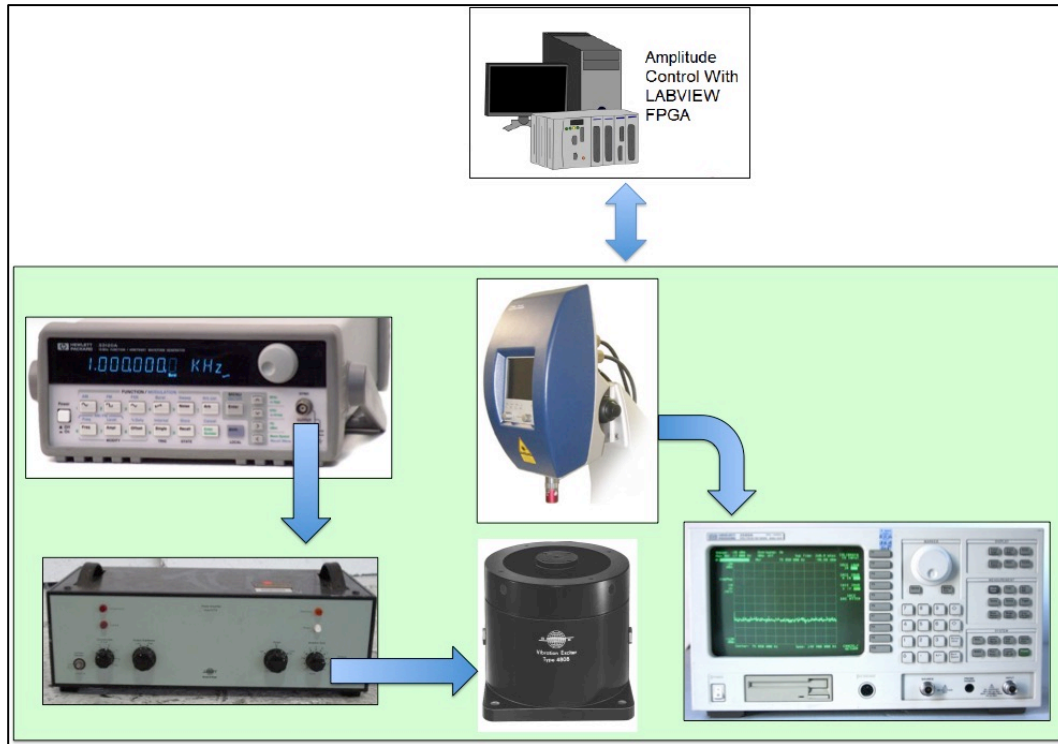
Laser–Doppler vibrometry is used in a similar way as in the previous chapter to evaluate the performance of such a device.

The complete measurement set–up (schematically reported in fig. 9(b)) is composed of a Polytec Vibrometer MSA400 in conjunction with a PM Vibration Exciter Type 4808 from Bruel & Kiaer (fig. 9(a)) [8] driven by a signal generator Hewlett Packard (HP) 33120A through a Power Amplifier Type 2712 (Bruel & Kiaer); the device under test (DUT) is measured by the vibrometer and the output signal (velocity analog signal) is fed into the Spectrum Network Analyzer 3589A from HP, allowing the extraction of the frequency spectrum.

The whole data acquisition process as well as all the instruments are controlled through a PC running a Matlab code.



(a)



(b)

Figure 9. Experimental set-up implementing vibrometry measurements by Doppler effect. The shaker from Bruel & Kiaer in (a). In (b) is illustrated the instrument chain, composed of a LDV MSA 400, an external function generator HP 33120A connected to a Bruel & Kiaer power amplifier 2712 that drives the shaker. The output signal from the MSA 400 (velocity output) is fed into the spectrum analyzer HP 3589A, returning the amplitude value for each driving frequency. The measuring process is controlled by a PC that runs a Matlab code and records the amplitude and frequency values, enabling the reconstruction of the frequency spectrum.

The PDMS device was secured (through double-side Kapton tape) on a ceramic dual-in-line package (DIP), which is then soldered to a general purpose breadboard and finally mounted to the shaker moving plate by means of four screws, as illustrated in fig. 10.

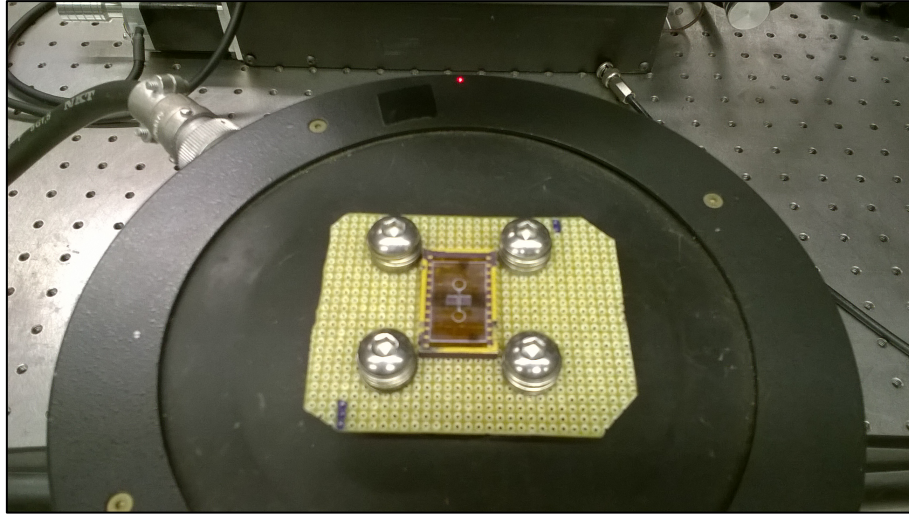


Figure 10. The PDMS device is “packaged” in a ceramic dual-in-line package (DIP) through double-side Kapton tape. The DIP is then soldered to a general purpose bread board and the whole parts are mounted to the vibrating membrane of the shaker by four screws.

The measurements outcomes for the resonant frequency are reported in fig. 11 where the plot for the empty channel and the channel filled with corn oil are compared: the resonance value goes from 1,3756 kHz for the empty channel to the lower value of 1,1671 kHz for the filled channel; this decreasing trend is expected since the oscillating mass is higher when the channel is filled up with the oil.

The settings of the above test are:

1. Driving voltage of 50mV
2. Velocity decoder set to 5mm/s/V
3. Amplification gain is 7

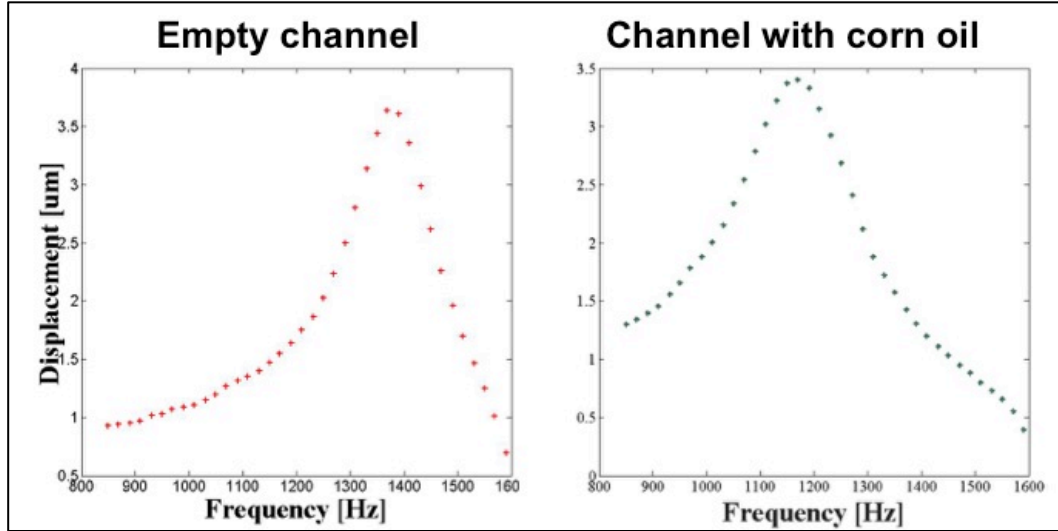


Figure 11. Resonant response of the empty (on the left, red plot) and filled channel with corn oil (on the right, green plot).

Parametric resonance response though was not achieved for devices (up to three) manufactured in this way, suggesting that the PDMS is a too dissipative material, thus not suitable for this purpose: to verify this guess a simple fixed–fixed beam geometry in PDMS was investigated in terms of resonance peak as a function of different driving voltages both in air and vacuum.

4.3.2.1 Scaling of beam

The much more simple geometry (just a beam with no channel) together with the need for vacuum measurements give the opportunity for the realization of a device having the same dimensions for the suspended element in device with a smaller footprint, since inlet/outlet ports are not necessary: the geometry is reported in fig. 12 where we can see that the suspended beam has the same dimensions of the original channel. On the other hand, the use of a vacuum chamber is required to perform vacuum testing and for this reason the shaker is replaced by a piezo–shear actuator P–141.03 in fig. 13 (PICA series from Physik Instrumente GmbH) [9].

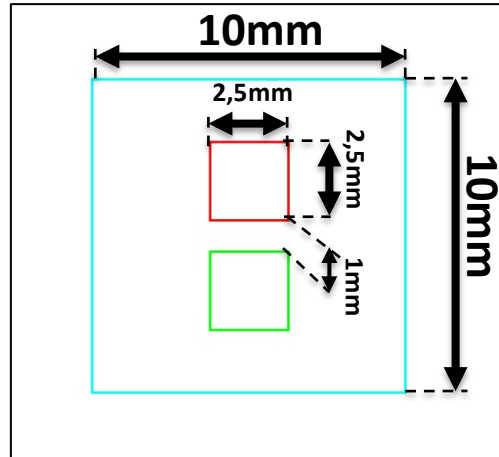


Figure 12. Layout with dimensions of the geometry used to realize simple doubly clamped beam by laser-cut.

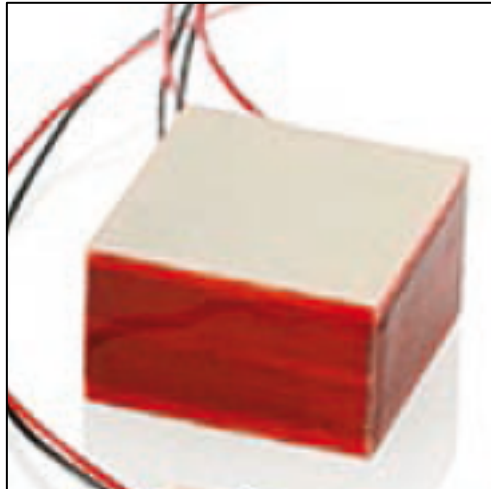
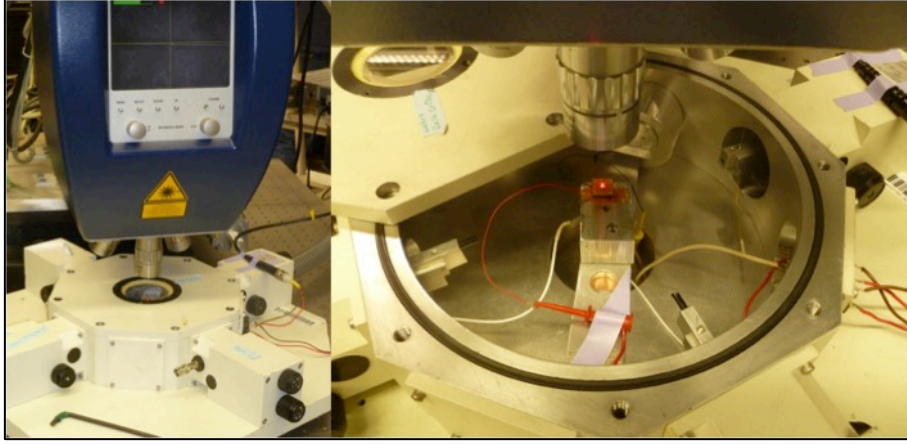
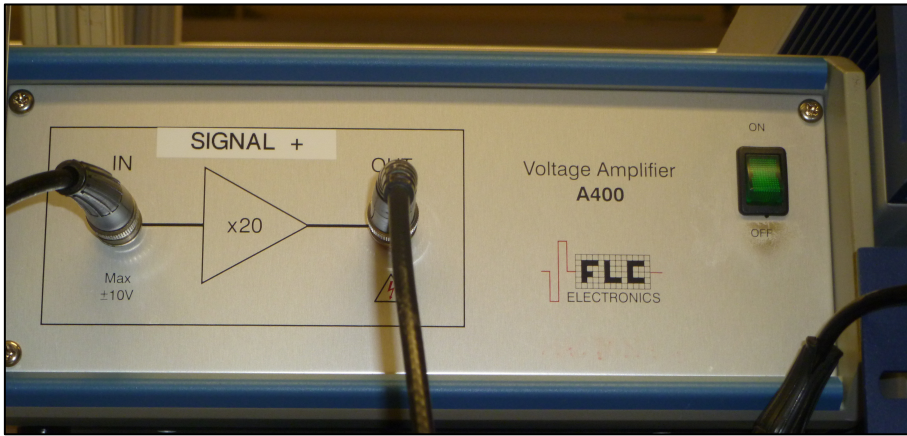


Figure 13. The shear-piezo actuator P-141.03 used to drive the device.

The measurement set-up remains the same of fig. 9(b) upon the substitution of the shaker with the shear-piezo for the actuation, the use of a vacuum chamber in fig. 14(a), and the Power Amplifier Type 2712 with the A400 voltage amplifier from FLC Electronics (fig. 14(b)).



(a)



(b)

Figure 14. Vacuum chamber (a) and voltage amplifier (b) used for the measurements of the beam.

The DUT is mounted to the piezo actuator as shown in fig. 15: the top face of the piezo is covered with a double side copper tape (Cu tape) upon of which there is a squared acrylic layer (1cm side) with a hole in the central part allowing for the beam to oscillate; a second Cu tape film is placed on top of the spacer where the DUT is attached.

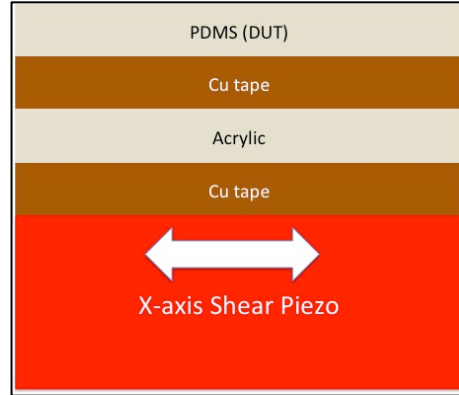


Figure 15. Schematic representation of the DUT mounted to the shear–piezo component: a first Cu tape (double side) is placed onto the surface of the actuator and an acrylic layer (with a hole in the center to allow the movement of the beam) acts as a substrate for the DUT which is in turn attached to it through a second Cu tape film.

The beams are realized by laser cut using the same process and cutting parameters explained earlier with the exception that engraving is not present: fig. 16 shows beam #3 which is the one used during the tests.

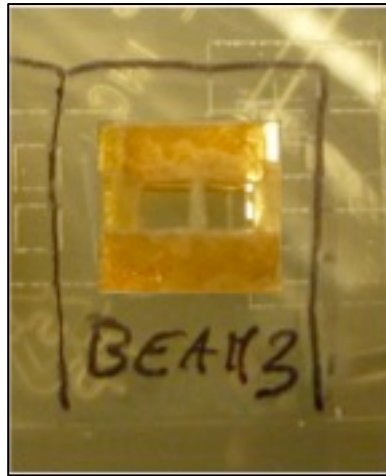


Figure 16. Picture of the used DUT removed from the actuator at the end of the measurements sessions.

The frequency response in vacuum (20mTorr) in the vicinity of the resonance peak for different driving voltages is reported in fig. 17, from where we recognize the so-called “*soft spring*” or “*softening*” behavior: the higher the driving voltages, the lower the resonant frequency, a well-known non-linear effect (conversely, when the resonant peak moves to higher frequencies with increasing voltages we have the “*hard spring*” or “*hardening*” behavior) [10,11].

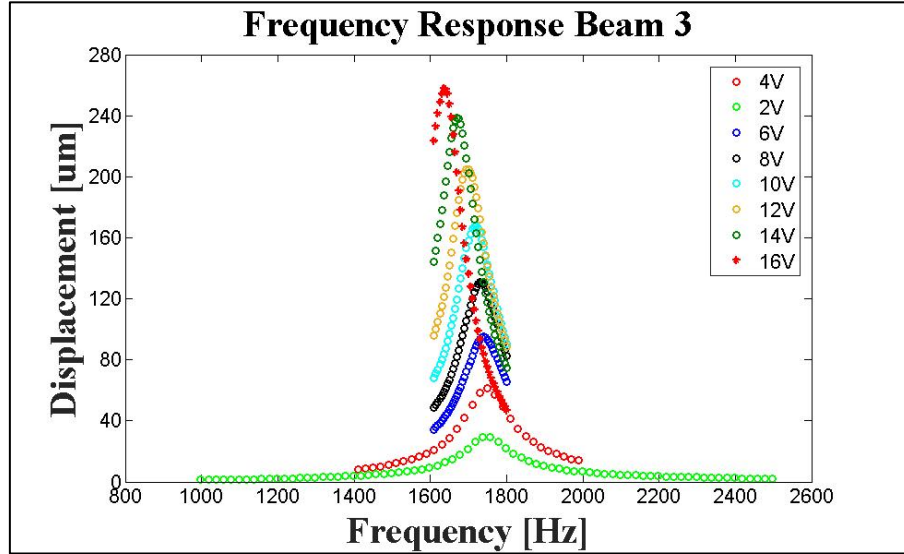


Figure 17. Frequency response in vacuum (20mTorr) in the vicinity of the resonance peak for different driving: we recognize the so-called “soft spring” or “softening” behavior: the higher the driving voltages the lower the resonant frequency. The driving voltages are those sourced by the function generator and fed into the voltage amplifier with gain of 20.

Note that the voltages reported in the picture are those sourced from the signal generator and must be multiplied by the amplifier’s gain which is 20x to have the effective voltages that are applied to the piezo.

Despite this nonlinear response featured by the beam – not present in the device with the channel – it does not show parametric resonance even in vacuum; as for the hollow beam, the dissipation is the main reason: firstly because of dissipation internal to the material, then because the coupling between the piezo–shear and the DUT is not perfect, finally for lossy paths due to the interlayers.

To complete the study, beams with different dimensions have been fabricated (in the limit of the laser cutting capabilities) and measured:

- 1) a narrow beam with higher length–to–width (L/W) aspect ratio: $L = 2,5\text{mm}$, $W = 250\text{ }\mu\text{m}$, $L/W = 10$; the thickness T is that of the original PDMS sheet, namely $250\text{ }\mu\text{m}$, thus $W/T = 1$;

From the SEM images reported in fig. 18(a) and (b), it can be seen that the beam presents not straight sidewalls (due to the laser process that produces localized micro–explosions).

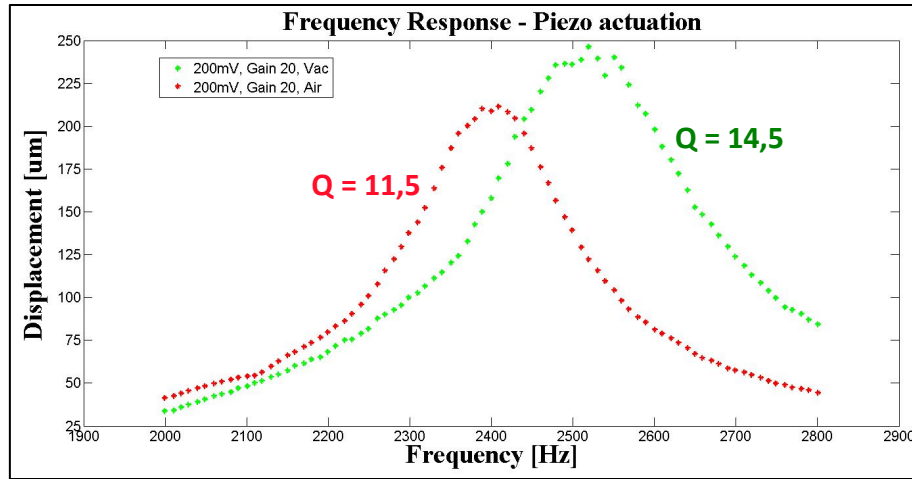
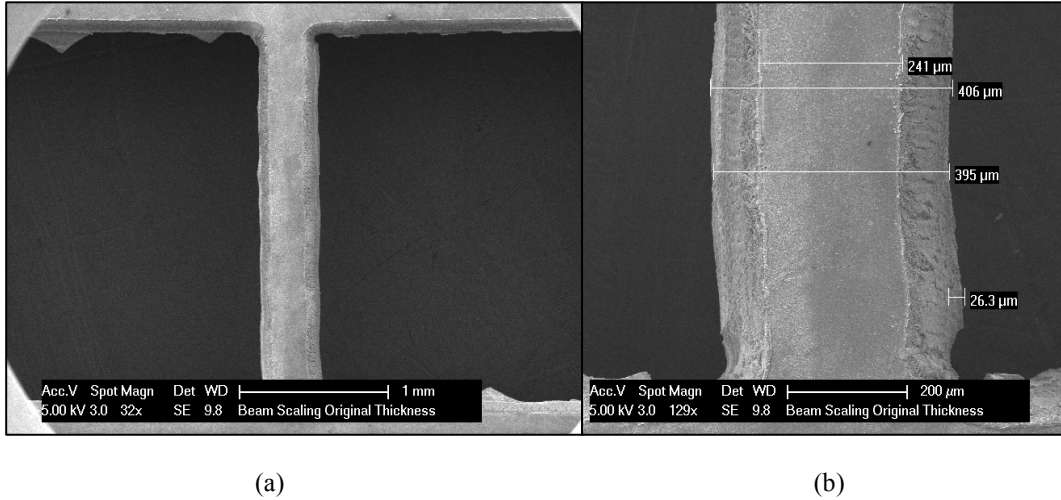


Figure 18. Beam with scaled dimensions: $L/W=10$, $W/T=1$. SEM images in (a) and (b) show that the profile is not sharp: not straight sidewalls. In (c) the measured resonant peak in air (red plot) and vacuum (green curve) are shown. The quality factor of this device remains almost the same, suggesting that the PDMS is an intrinsically dissipative material. The driving voltage in both cases is 200mV sourced by the function generator and fed into the voltage amplifier with gain of 20, for a final peak to peak voltage of 4V.

In fig. 18(c), the resonant peak is reported for air and vacuum environment, with the the quality factor changing from 11,5 to 14,5 respectively: such a small value of Q even in vacuum – where values around the hundreds were expected – remarks the dissipative nature of the polymer.

- 2) a slender beam with L/W from 1) and a thickness of less than 100 μm in order to obtain $W/T \approx 3$;

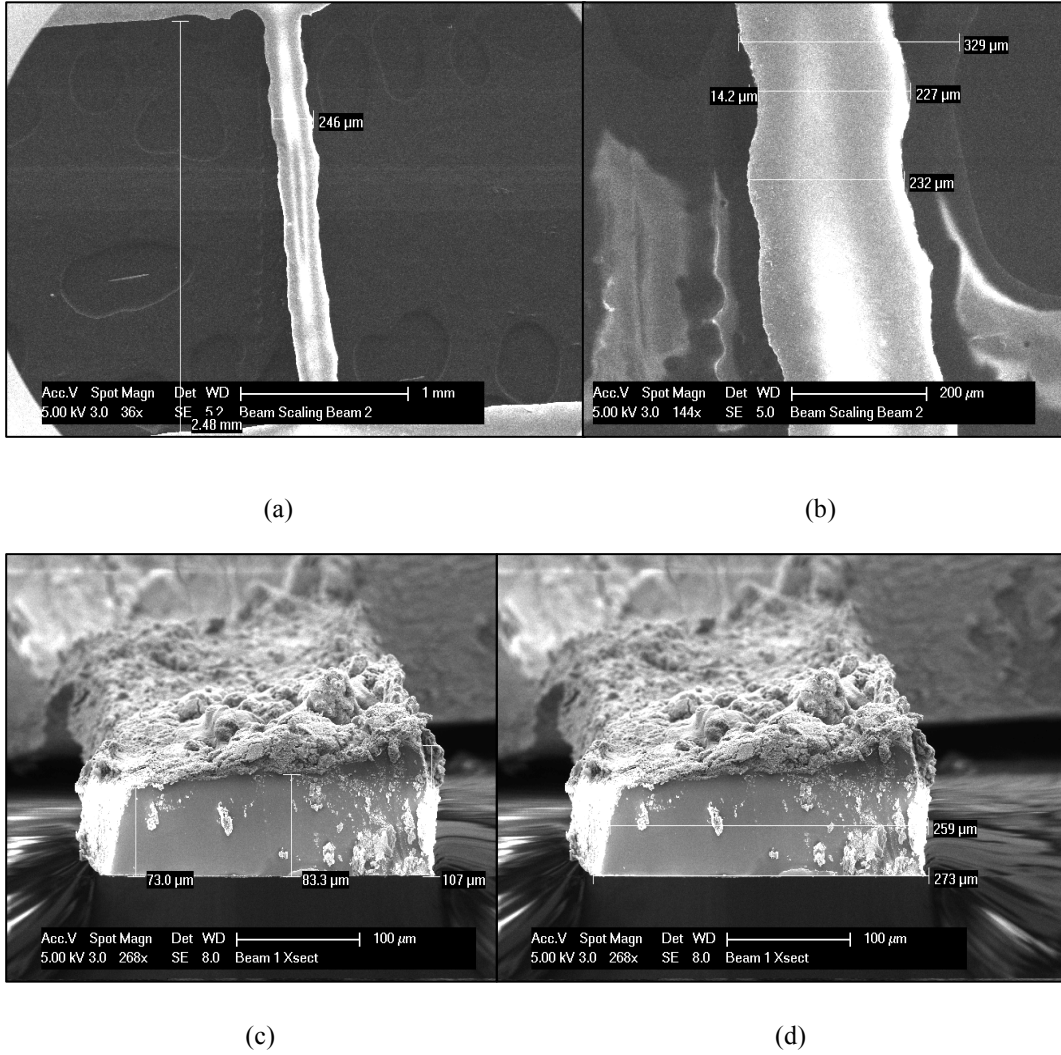


Figure 19. Beam with scaled dimensions: $L/W=10$, $W/T=3$. SEM images in (a) and (b) show that the profile is worse than the previous beam. In (c) and (d) the beam was cut to investigate the cross-section, that also has irregular dimensions. Furthermore the pretty rough surface of the etched face is clearly visible: the roughness influences the quality factor of a vibrating structure.

For the slender beam the situation – in terms of the geometry – is much worse with respect to the previous case: as shown in fig. 19(a) and (b), the profile is quite irregular and the cross-section is not uniform ((c)–(d)). Furthermore the engraved face to make a thinner beam shows a high roughness: all these aspects are linked to the use of a laser-based process technology on a thinner PDMS layer with a consequent negative impact to the dynamic behaviour of the beam (fig. 20) against a parametric resonance response.

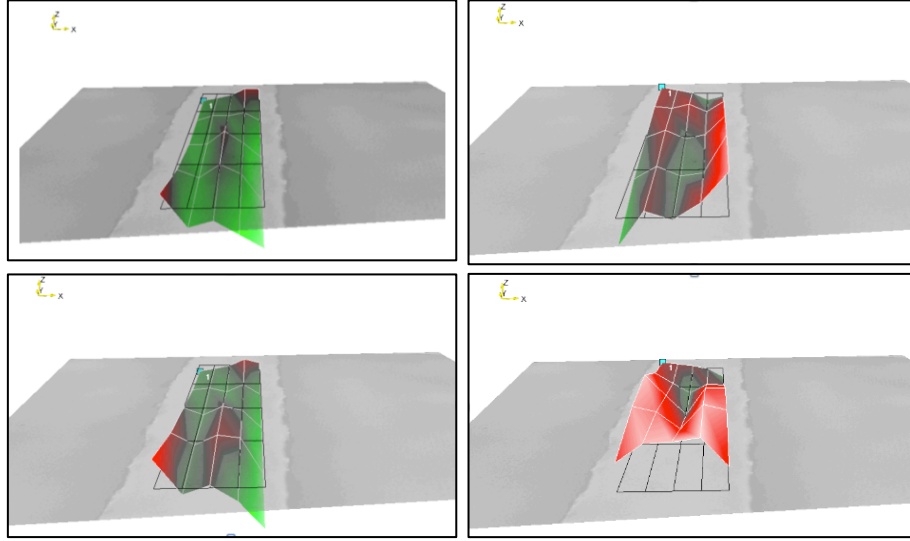


Figure 20. Software reconstruction (from the MSA 400 measurements) of the beam moving. Clockwise orientation: the beam is oscillating upwards and we can see that the movement is not planar, negatively affecting the dynamic behavior, mainly characterized by poor Q -values.

4.4 Second design

After the exploration of PDMS as structural material for the parametric resonator device, a second different prototype has been investigated. A possibly more appropriate – in terms of mechanical characteristics of the material – proposed resonator employs a “Flexible Fused Silica Capillary Tubing” as a suspended channel, and has been investigated hereafter.

The structure of the device is shown in fig. 21 and is very similar to the previous device: a capillary tube (supplied by Molex) [12] with circular cross-section is glued to a glass die serving as substrate through an epoxy glue (2 Ton[®] Epoxy) by Devcon (see fig. 24), which is widely used because of a strong, rigid bonding force on glass and other different materials [13].

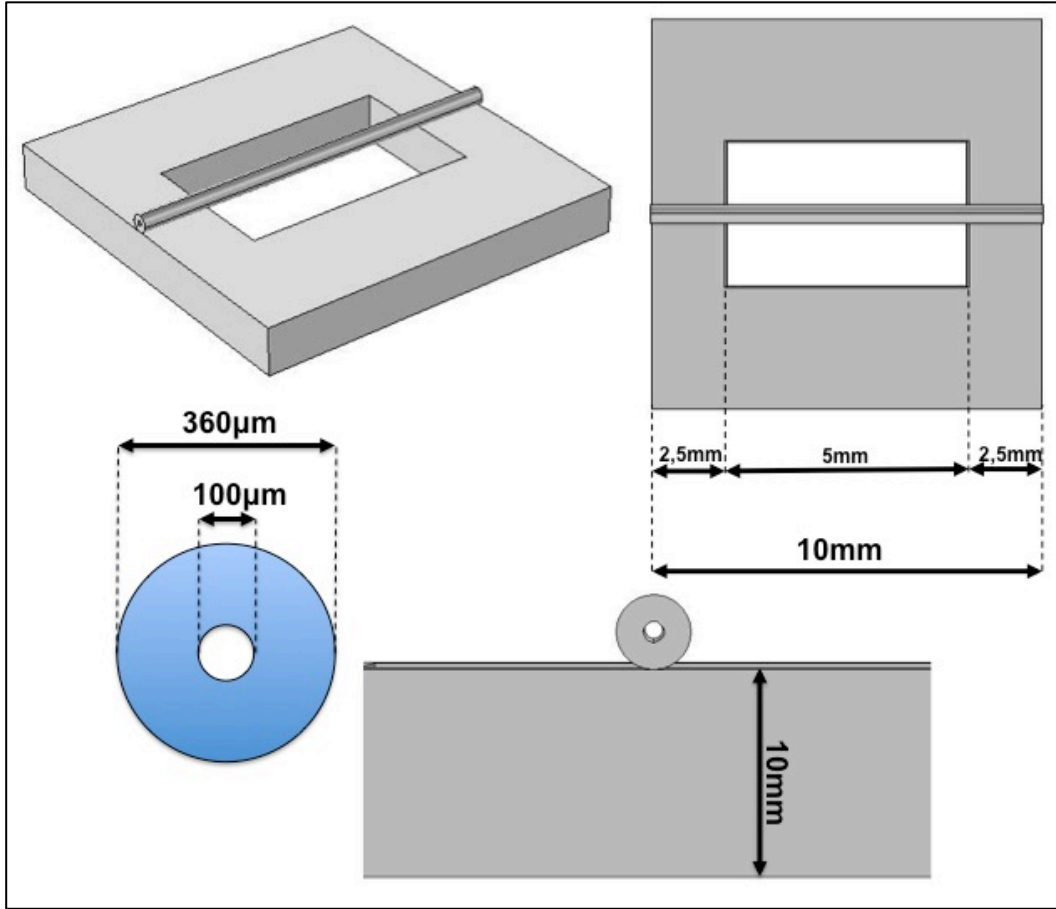


Figure 21. Schematic representation of the capillary tube as microfluidic channel: 3D representation on the upper left corner; top-view on the upper right corner. A cross-section view with a detail of the channel cross-section is represented in the bottom.

The capillary tube measures 100 μm and 360 μm for the inner and outer diameter respectively and the suspended part is chosen to be 5mm in length (note that the choice of this parameter is constrained by the shear-piezo dimensions).

4.4.1 Modelling of the suspended microchannel resonator

The discretization of the structure, in this case, was created through a composed mesh: "*free tetrahedral*" for the fused silica sub-domain, and a "*swept*" mesh for the glass substrate sub-domain: meshing in different ways different sub-domains allows to have a poor discretization (coarse) on those domains that do not play an active role in the

simulation, and a finer mesh can be applied to those parts that are important for the analysis. In doing this, the overall computing efforts are less demanding (with respect to a single mesh for each domain), and the results can be more accurate since more elements are present in the critical domains. In this case the glass substrate is a big domain with no role to the definition of the resonant frequency of the suspended channel, reason thereby it has a coarse mesh and the capillary tubing has a finer one, as shown in figure 22.

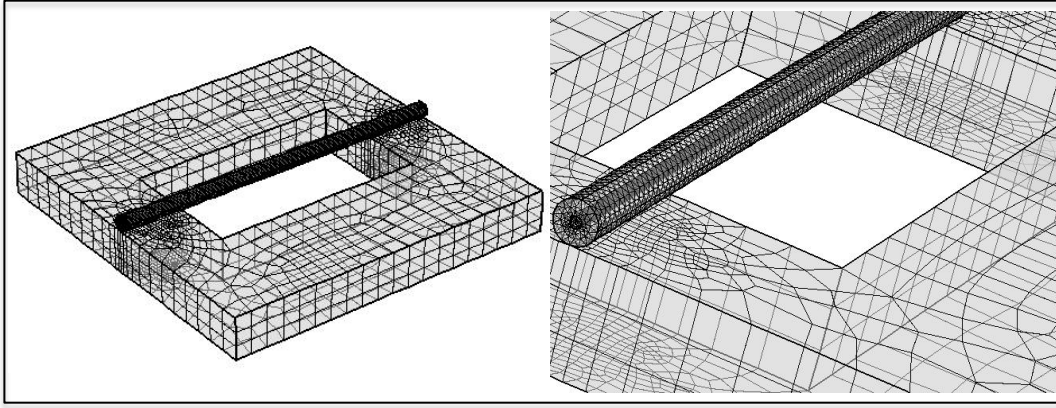


Figure 22. Mesh of the geometry in fig. 21: the channel has a finer discretization as shown in the zoomed image, thanks to the different mesh applied to the two sub-domains. In this configuration the complete mesh consists of 40455 domain elements, 11906 boundary elements, and 1821 edge elements.

The mesh parameters are: maximum element size is 80 μm , minimum element size is 10 μm , maximum element growth rate of 2 a curvature factor of 0,6 and 0,5 for the resolution of narrow regions for the fused silica capillary tube and 440 μm , 32 μm , 1,4, 0,4 and 0,7 respectively for the glass substrate.

Fig. 23 shows the FEM pictures of the first out-of-plane mode for such a structure, simulated in COMSOL Multiphysics where the default values of 73GPa for the Young's modulus and of 0.17 for the Poisson's ratio were used as input mechanical parameters. FEM calculations output returned $f_{0,vacuum} = 63,860$ kHz and $f_{0,air} = 63,827$ kHz, for vacuum air background respectively.

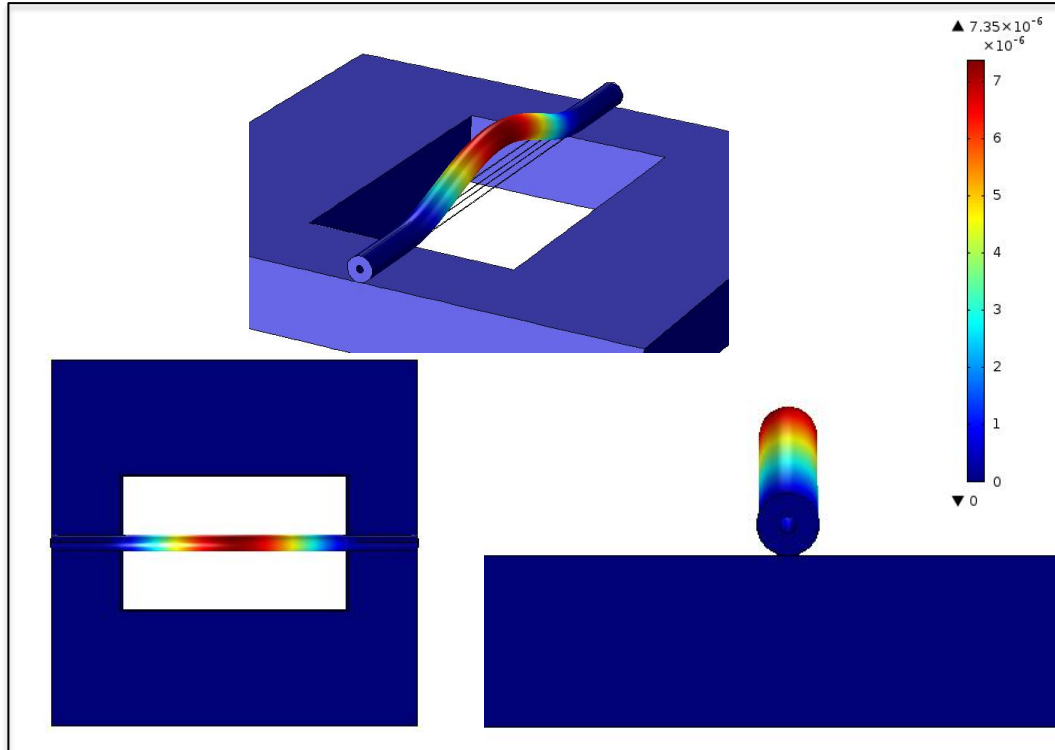


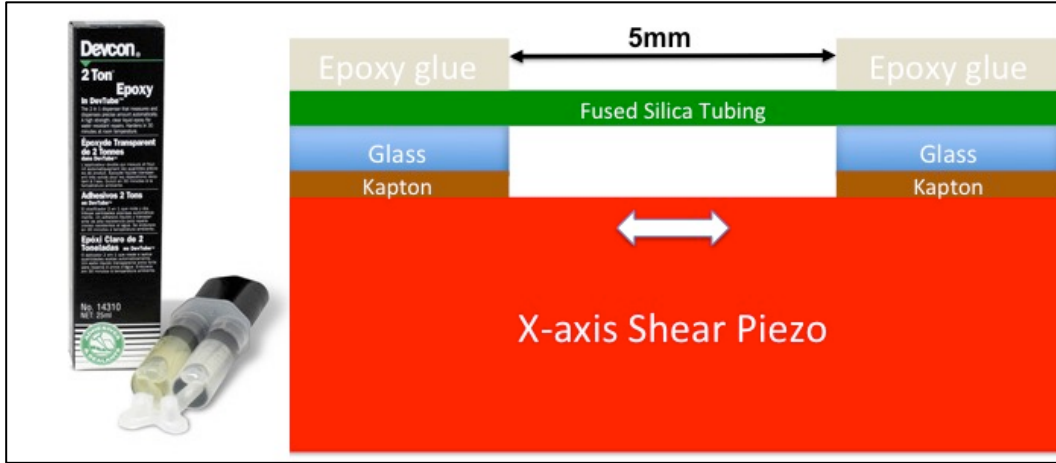
Figure 23. The designed device is represented in a FEM simulation showing the first resonant mode in air environment. The top and side views are in (b).

4.4.2 Fabrication and Characterization

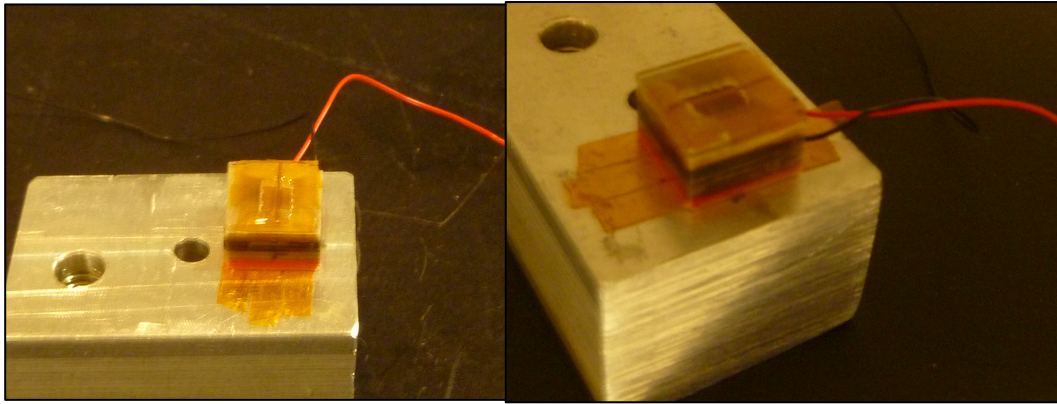
The fabrication of such a prototype is quick and simple: starting with the cut and drilling of the glass that will serve as substrate for the capillary tube, the next step is the preparation of the epoxy glue by following the instructions in the technical sheet.

Of course the glass substrate was previously cleaned by solvent-wiping any deposits of glass debris from the cut and drill operations, dust or other contaminants: full bond strength is reached in 16 hours.

The final device – already mounted on the shear-piezo actuator is illustrated in fig. 24.



(a)



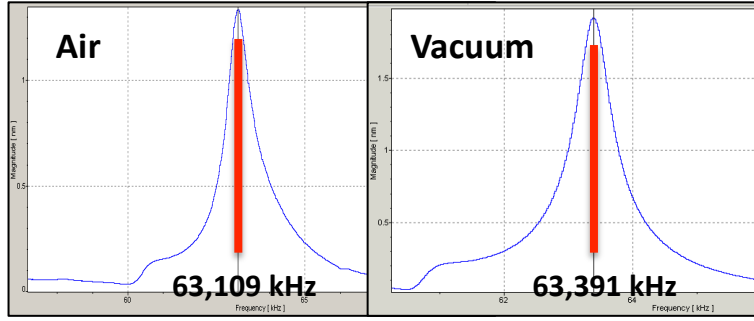
(b)

Figure 24. Mounting: (a) schematic representation of the DUT mounted to the shear–piezo component: a film of Kapton tape (double side) is placed onto the surface of the actuator and a glass die (with a hole in the center to allow the movement of the beam) acts as a substrate for the capillary tube which is attached to it through the epoxy glue. The real device attached to the piezo actuator is shown in (b).

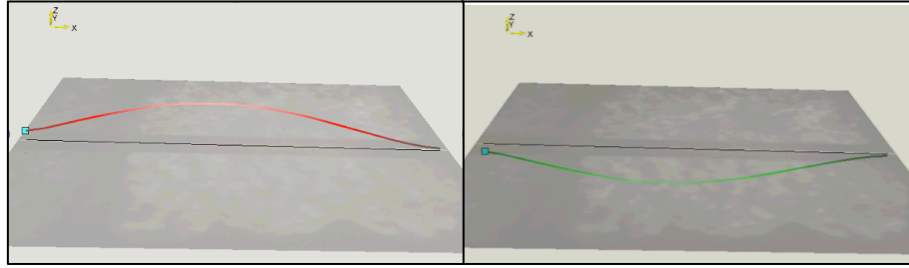
The characterization results are obtained through the use of the MSA 400 also for this device and are reported in fig. 25 where the frequency response for both air and vacuum (20mTorr) measurements are shown along with some frames showing the beam moving.

The measured values of the resonance frequency are 63,391 kHz and 63,109 kHz in vacuum and air respectively: note that the former is pretty close to the simulated value.

The driving voltage for these measurements is $4V_{pp}$ (200mV from the internal generator that are multiplied by the gain of the amplifier, which is 20x).



(a)

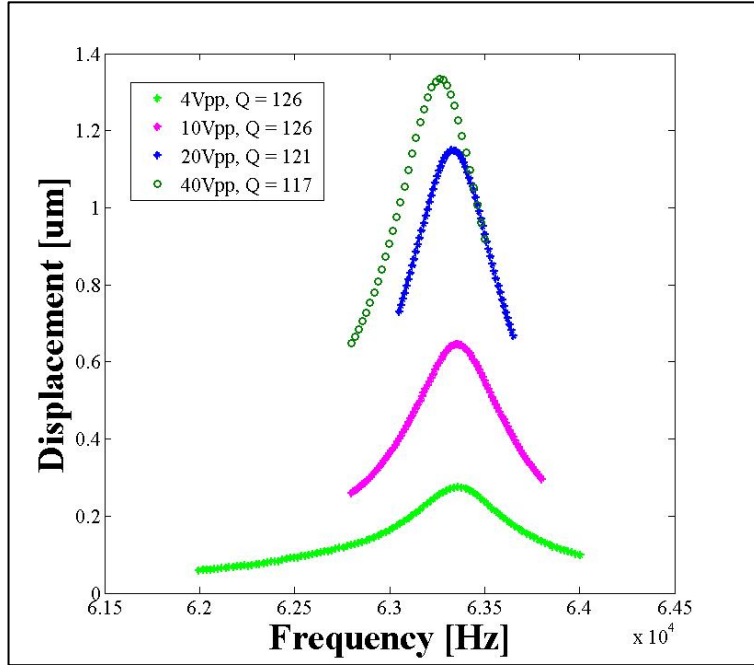


(b)

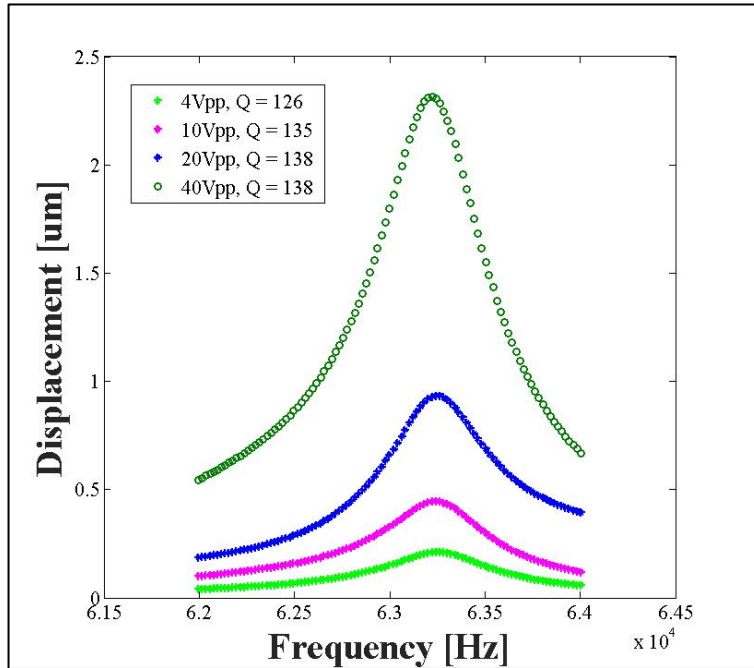
Figure 25. The measured (from the MSA 400) resonant peak in air (left) and vacuum (right) are shown in (a) for the device with fused silica capillary tube. Software reconstruction of the beam moving at its resonance frequency in (b).

Using the same set-up as for the beams in PDMS for the non-linear behaviour (namely hardening or softening response), we have measured the spectrum of the device near the resonance for different driving voltages: the results are shown in fig. 26(a) and (b) for air and vacuum environment respectively. The plots show a softening response.

The values for the quality factor are an order of magnitude higher if compared to those achieved with the PDMS, thanks to the higher Young's modulus (vs the PDMS Young's modulus) and the more rigid bond of the anchoring points (due to the epoxy glue), obtaining a better yield on the dynamic response.



(a)



(b)

Figure 26. Frequency response in air (a) and vacuum (20mTorr) (b) in the vicinity of the resonance peak for different driving voltages, showing a “softening” behavior. The Q -values for this device are above 100, an order of magnitude higher if compared to the PDMS devices. The driving voltages in both cases are the final from the output of the amplifier.

With such promising values for the Q we started to seek for parametric resonance in both air first and in vacuum then: in the former case no parametric resonance response was obtained, while it was successfully measured in vacuum, as reported in fig. 27.

The strategy carried out to measure a parametric resonance event is to drive the device in a frequency range centered at twice the natural harmonic resonance (previously measured) and wide enough to contain the zero amplitude response: a frequency scan then takes place starting from the lower value to the higher (with a predefined step) and back. The recorded vibration amplitudes, instead, are those measured at half the driving frequency, namely in a range centered at the natural harmonic resonance of the system (recalling Eq. (9) in chapter 1, with $n = 1$ we have the first parametric resonance). The measurements are run automatically using the same set-up in fig. 9(b), where the shaker is replaced by the shear-piezo in the vacuum chamber (fig. 14(a)) and the appropriate Matlab code is used.

The plot in fig. 27 shows the jump on the right-hand side: the oscillation amplitude increases up to a maximum and then collapses to zero. This is clearly the signature of a parametric resonance event, and the jump on the right is typical of a fixed-fixed beam structure.

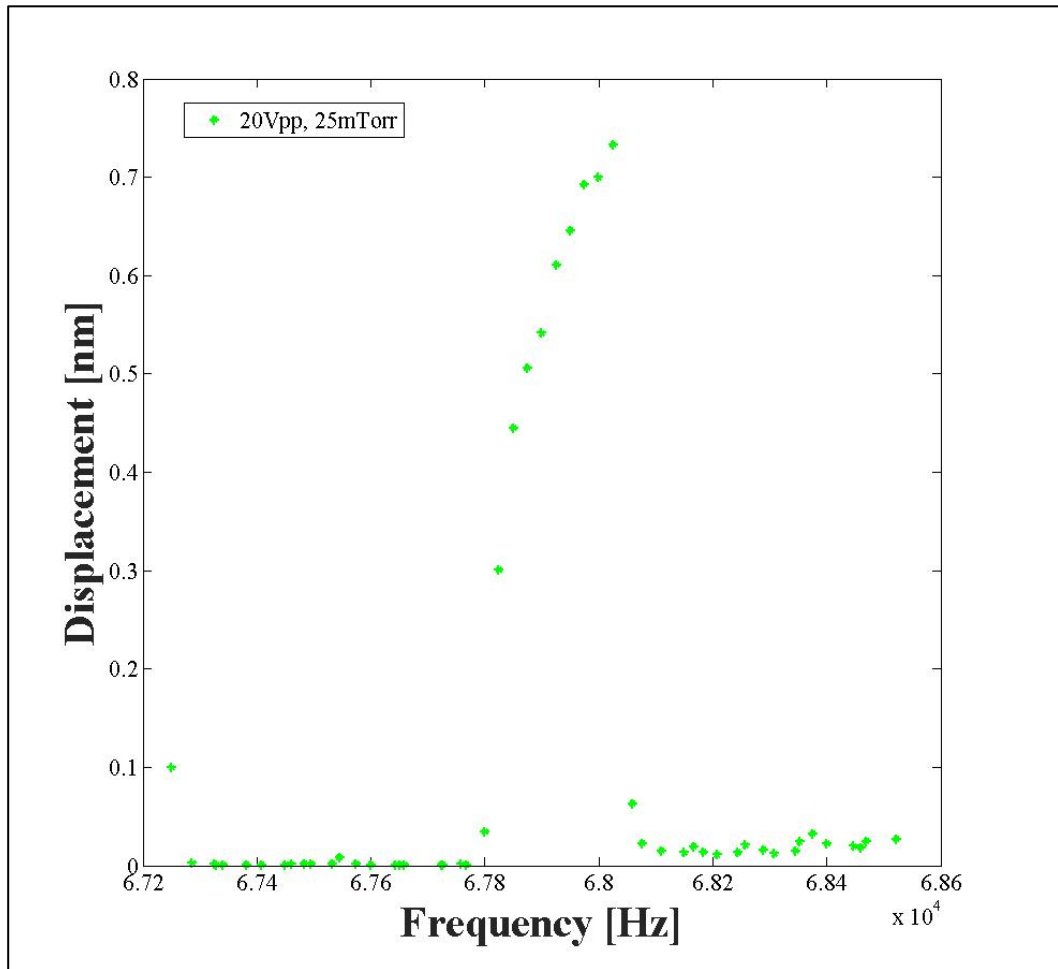


Figure 27. Parametric resonance response: from a zero-amplitude response the amplitude increases until collapses to the zero-amplitude again (“jump”).

References

- [1] Material Property Database, Massachussets Institute of Technology.
- [2] Folch A 2012 Introduction to BioMEMS (Bosa Roca: Taylor and Francis) pp 22–24.
- [3] Mark J E 1999 Polymer Data Handbook (New York: Oxford University Press).
- [4] Inglis D W 2010 A method for reducing pressure-induced deformation in silicone microfluidics Biomicrofluidics.
- [5] Mechanical characterization of bulk Sylgard 184 for microfluidics and microengineering, D Johnston, D K McCluskey, C K L Tan and M C Tracey, J. Micromech. Microeng. 24 (2014) 035017 (7pp).
- [6] “Templateless prototyping of polydimethylsiloxane microfluidic structures using a pulsed CO₂ laser” Hao-Bing Liu and Hai-Qing Gong, J. Micromech. Microeng. 19 (2009) 037002 (8pp).
- [7] Snakenborg D, Klank H, Kutter JP (2004) Microstructure fabrication with a CO₂ laser system. J Micromech Microeng 14: 182-189.
- [8] PM Vibration Exciter Type 4808 User Manual, Bruel & Kiaer
- [9] Piezoelectric Actuators Products Catalog, PI
- [10] Stephen Beeby, Graham Ensell, Michael Kraft, Neil White, “Mems Mechanical Sensors”, 2004 ARTECH HOUSE, INC.
- [11] Ki Bang Lee, Albert P. Pisano and Liwei Lin, “Nonlinear behaviors of a comb drive actuator under electrically induced tensile and compressive stresses”, J. Micromech. Microeng. 17 (2007) 557–566.

[12] Molex Technical Datasheet

[13] 2 Ton® Epoxy Technical Datasheet, Devcon

Chapter 5

Conclusions and Outlook

This PhD thesis deals with experimental studies concerning new technologies and methodologies for the development of a novel class of mechanical resonators for applications to the sensing and detection of chemical substances present in liquids environment.

The microfluidic devices realized using novel microfabrication techniques like the Two-Photon Lithography, and rapid prototyping processes like the laser machining of polymers, presented in this thesis are of particular interest for Lab-On-Chip (LOC) applications.

In the thesis, all single aspects of the proposed approaches are developed. An overview of the design and the fabrication of suspended resonators in LOC devices has been given. The detail of the experimental optimization of the fabrication procedures and the experimental set-up used for the characterization (measuring the resonance frequency) of the devices, by means of the Laser-Doppler Vibrometry (LDV) technique, have been described.

In the first part the realization of a Suspended Microchannel Resonator (SMR) via Two-Photon Lithography, demonstrating the effectiveness of such a technique to realize a SMR made of commercial SU-8 photoresist, has been introduced. Although the here-reported structures are based on vertical I/O sections, the versatility of TPL allows writing also inlet/outlet port with other orientations, allowing another degree of freedom in interfacing with microfluidic devices. To reduce the fabrication time due to the large dimensions, a shell-writing technique based on the polymerization of a 3 μm -thick contour of the structure has been described. The mechanical characterization was carried

out with subnanometer resolution, showing good agreement with FEM simulations. The obtained results in terms of first flexural mode dynamics lets suggest that TPL-written SMR – after a proper functionalization step – can be embedded in a more complex microfluidic device for the realization of a lab-on-chip systems.

In the second part of the thesis it has been explored the use of the parametric resonance for a label-free sensing of biomolecular species, as an alternative to most of the mechanical resonating devices – where the variation of frequency by the mass adsorption is given simply by monitoring the natural resonance frequency. The parametric resonance is a mechanism of mechanical amplification displayed by systems whose dynamic behavior is governed by a Mathieu equation. For these systems, large responses may be generated when the frequency of excitation is a multiple of the natural resonance frequency: the main characteristic of this mode of operation is the sharp transition between oscillatory and non-oscillatory behavior, always occurring for the same frequency value (double the natural resonance frequency, for the first parametric resonance condition). Perturbations that decrease the frequency (of excitation or resonance as in our case) lead to a collapse of the oscillation back to the zero amplitude: driving the detector with a sinusoidal signal of frequency equal to its parametric resonant frequency, keeps the system at the boundary of the parametric region; adding mass to the resonator induces a decrease in its natural resonance frequency, thus causing the parametric resonance condition not to be satisfied, and forcing the system output to be zero.

By monitoring the transition (“jump”), very small frequency shifts can be accurately detected and a high sensitivity is expected.

Firstly, the realization of a low-cost PDMS microfluidic channel via rapid prototyping approach has been showed. The microfluidic structure is composed of two PDMS foils that are machined by laser-cutting technology for the channel definition and bonded together using a protocol well described in the thesis.

This category of device has proven to be suitable to be employed as standard microfluidic channel resonators but are not indicated for parametric resonance approaches, since the PDMS is intrinsically a dissipative material, strongly limiting the Q of the system, which

is of paramount importance for the onset of parametric resonance response.

Next and finally, a simple assembled device, composed of a microfluidic channel made out of commercial fused silica capillary tubing was proposed and investigated. The microchannel is simply cut from a commercial part and is bonded to a glass substrate using an epoxy resin.

Conversely to the previous device, this solution shows Q -values above 100 and are one order of magnitude higher with respect to the PDMS devices, mainly due to the large Young's modulus of the fused silica and the strong and rigid bond ensured by the epoxy resin. This device shows a parametric resonance response and is promising for the application.

No fluidics experiments have been carried out on the devices devoted to test their behaviour in the application: the next steps are thus the implementation of an experimental set-up that allows to connect the devices to a fluidic system to evaluate and verify the true performances of the solutions.

On a long term the integration of the sensing elements in a microfluidic system can be envisioned as the final step for the design and realization of complex lab-on-chip platforms applying analyses in chemistry, medicine or biology.

Acknowledgements

This PhD program was financed by the Ministry of Education and Research for the project "PONa3_00077, Infrastructure Project for bio-MEMS Technologies for Advanced Sensing of Environmental and Food Monitoring and Diagnostics", and has involved academic and research centers such as Politecnico di Torino, the Center for Biomolecular Nanotechnologies (CBN) of the Istituto Italiano di Tecnologia (IIT) in Lecce and the Prof. Kimberly Turner's Mechanics of Microscale Systems Lab at University of California Santa Barbara.

With this work, I have now the chance to express the gratitude and esteem I feel for those persons who have directly or indirectly helped or sustained me all over these intense years.

First of all I want to thank Prof. Massimo De Vittorio (IIT-CBN) who gave me the great opportunity to be part of his group, and for his guidance throughout the project and Prof. Candido F. Pirri (Polytechnic of Turin), for promoting and setting up this special PhD program between IIT and the Interpolytechnic Graduate School (Scuola Interpolitecnica di Dottorato).

Deep gratitude to Dr. Francesco Rizzi, Researcher at IIT-CBN, together with Dr. Antonio Qualtieri and Dr. Ferruccio Pisanello (IIT-CBN) and Prof. Carlo Ricciardi (Polytechnic of Turin), for all the experience, efforts, suggestions and support put into this research: thanks to them I have gained a lot of experience.

I am very very grateful to both Prof. Kimberly Turner and Dr. Maria Teresa Napoli for giving me the opportunity to join them at the University of California Santa Barbara (UCSB), discovering the world of the parametric resonance. With their enthusiasm they have always positively influenced and motivated me.

A special thanks goes to Dr. David Bothman (UCSB) for the support in the lab environment, and for his enormous patience in teaching me how to use the tools.

Thanks to the colleagues but also friends: Jamie, for being the perfect person to make fun of during a SEM session; Brian for his music sessions while in the lab; Lily for the funny time during the day and for being easy in lending me her measurements instruments, especially the shear piezo; many thanks to Kamala for the help with the Comsol simulations and Luke for motivating me.

Also many thanks to all the personnel I have met in the cleanroom for being always available to help and dispense suggestions.

Thanks to all the people I have met during my staying in California, it has been a great time, very intense and full of emotions and I know that whenever in the future I will think about these days, I will say: “I wish go back to that time”!

A three-years PhD program is a long way, sometimes hard moments have to be faced: you can go beyond such moments thanks to the people who surround you day-by-day: in addition to the people above, thanks to Davide, Vincenzo, Francesco, Tommaso, Sara, Paola, Andrea and Tiziana.

Special thanks to Ludovico, Mirko, Mattia, Nino, Alessandro, Emma, Julia, Bhaswar, Paolo and the others living in California.

Thanks to all my friends, always supporting and trusting in me.

I want to thank my family of course: my parents and my sister are something extraordinary and I am very proud to be part of them.

